Dynamics of complex systems studied by terahertz radiation

Dissertation
zur Erlangung des Doktorgrades
an der Fakultät für Mathematik, Informatik und Naturwissenschaften
Fachbereich Physik
der Universität Hamburg

vorgelegt von
Christoph Matthias Testud
geboren am 5.November 1987
in Freiburg im Breisgau

Hamburg
2018

Gutachter/in der Dissertation:	Prof. Dr. Nils Huse
	Prof. Dr. Arwen Pearson
Zusammensetzung der Prüfungskommission:	Prof. Dr. Nils Huse
	Prof. Dr. Arwen Pearson
	Prof. Dr. Michael A. Rübhausen
	Prof. Dr. Dorota Koziej
	Prof. Dr. Gabriel Bester
Vorsitzender der Prüfungskommission:	Prof. Dr. Michael A. Rübhausen
Datum der Disputation:	20.06.2018
Vorsitzender Fach-Promotionsausschusses PHYSIK:	Prof. Dr. Wolfgang Hansen
Leiter des Fachbereichs PHYSIK:	Prof. Dr. Michael Potthoff
Dekan der Fakultät MIN:	Prof. Dr. Heinrich Graener

Eidesstattliche Versicherung

Hiermit versichere ich an Eides statt, die vorliegende Dissertationsschrift selbst verfasst und keine anderen als die angegebenen Hilfsmittel und Quellen benutzt zu haben.

Die eingereichte schriftliche Fassung entspricht der auf dem elektronischen Speichermedium.

Die Dissertation wurde in der vorgelegten oder einer ähnlichen Form nicht schon einmal in einem früheren Promotionsverfahren angenommen oder als ungenügend beurteilt.

Hamburg, den

_____

Abstract

In the last decades different principles to generate terahertz (THz) fields were developed, providing many different ways to generate THz radiation nowadays. These use for instance antenna structures in conjunction with a semiconductor [1], organic semiconductors [2] or air plasma [3]. If the goal is to generate high electric fields strengths, one possibility is to use the tilted-pulse-front excitation method in nonlinear crystals as introduced by Hebling et al. [4] and used in this thesis.
With only a single pulse, only linear spectroscopy is possible and time dependent processes cannot be resolved. In order to overcome this limitation, the approach of nonlinear pump-probe spectroscopy can be used in which the pump-pulse is driving the system to be analyzed out of equilibrium and the probe pulse is recording the response of the system. Thus, it becomes possible to analyze time dependent processes.

In the course of this thesis an apparatus was designed and built with THz pulses as one radiation source that can be combined with sources ranging from the visible to the mid infrared (MIR)[5]. The THz radiation is generated in a lithium niobate (LN) crystal, while the infrared (IR) light stems from an optical parametric amplifier (OPA) and wavelengths in the visible (vis) range can be generated by harmonics of the fundamental wavelength at 800 nm, of an amplified laser system. The setup is a versatile tool for studying time dependencies, for instance for the observation of low frequency modes (e.g. rotations) or carrier dynamics in solids. First measurements were performed on graphite oxide (GO). The setup can also be used to study molecules for instance lactose in a ploycrystaline solid or magnetic materials using the magnetic optical Kerr effect (MOKE).

As for GO the results are scientifically relevant for investigating the mobility behaviour of the carrier recombination processes by pumping such a system in the IR for the first time. The same membrane was studied in an IR pump-probe setup by Amul Shinde for gaining the relevant time constants that are used for the analysis of the THz data. These results are currently under discussion with regard to previously published literature. The decay model was motivated by the two temperature model, describing the energy transition from carriers to phonons. In conclusion, the recombination is measured and one important decay path is found to be arising via defects originating from the oxygen groups.
The results for the experiments of lactose and MOKE are also discussed and possible routes for further successful measurements are presented.

One major improvement, which will be implemented in the near future, is the use of a balanced detector system that will considerably improve the signal to noise ratio. Also, by cooling the LN crystal, stronger THz fields can be generated. One

promising application for this setup is to use strong THz pulses as a pump source to drive processes that are connected to low frequency modes, for instance in complex structures such as the deoxyribonucleic acid (DNA) double helix or complex proteins. This has barely been explored so far and should give access to information as to how delocalized THz modes (involving correlated motion of many atoms) couple to local modes, thereby providing unique new insights into the afore mentioned systems.

Zusammenfassung

In den letzten beiden Jahrzehnten sind die Möglichkeiten zur Erzeugung von THz-Strahlung stark angestiegen. Dazu gehören unter anderem Methoden mit Antennenstrukturen, organische Halbleiter oder Plasmen. Um hohe elektrische Feldstärken zu erzeugen, kann eine Methode verwendet werden, bei der die Laser-Pulsfront verkippt ist: In einem nichtlinearen Kristall wird durch nichtlineare Prozesse die THz-Strahlung dann erzeugt. Dieses Verfahren wurde von Hebling et al. eingeführt.

Lineare Spektroskopie, bei der nur ein Puls zum Einsatz kommt, kann keine zeitabhängigen Prozesse beobachtbar machen. Eine Möglichkeit, solche dynamischen Prozesse aufzuzeichnen, ist die Durchführung von nichtlineraren Anregungs-Abfrage-Experimenten. Dabei bringt der Anregungs-Puls das System aus dem Gleichgewicht und eine eventuelle Änderung kann durch einen Abfrage-Puls erfasst werden. Mit dieser Methode sind zeitabhängige Prozesse erfassbar.

Im Laufe der Arbeit wurde ein experimenteller Aufbau entworfen, der es ermöglicht, THz-Pulse mit anderen Lichtpulsen vom infraroten (IR) bis zum sichtbaren Bereich zu kombinieren, um Anregungs-Abfrage-Experimente durchzuführen. Die THz-Strahlung wird in einem Lithiumniobat (LN) Kristall erzeugt, wobei die Pulse aus dem IR-Bereich in einem optisch parametrischen Verstärker (OPA) erzeugt werden und die sichtbaren Pulse durch höhere harmonische der elementaren Strahlung des verstärkten Lasersystems. Dadurch ist ein vielseitiger Aufbau entstanden. Dieser kann beispielsweise niederfrequente Moden (z.B. Rotationsmoden) oder auch Ladungsträgerdynamiken messen. Erste Experimente in diesem Bereich wurden an Graphitoxid (GO) durchgeführt. Weiterhin können Moleküle wie Laktose oder magnetische Materialien mit dem Magnetooptische Kerr-Effekt (MOKE) untersucht werden.

Die Ergebnisse, welche durch die Untersuchung von GO gewonnen wurden, geben Aufschluss über die Ladungsträgerdynamiken und Rekombinationsmechanismen im System. Dabei wurde das System mit IR-Strahlung angeregt. Amul Shinde hat mit einem IR Anregungs-Abfrage-Experiment die gleiche Membran untersucht und die Zeitkonstanten ermittelt, die zur Analyse der THz-Daten benutzt wurden. Das Modell, welches den Mechanismus beschreibt, ist angelehnt an das Zwei-Temperatur-Modell. Dieses beschreibt unter anderem, wie Ladungsträger ihre Energie an Phononen abgeben. Die Interpretation der Zeitkonstanten wie auch ihr Wert werden zur Zeit in der Literatur debattiert. Abschließend ist aber festzuhalten, dass die Dynamik und Rekombination der Ladungsträger untersucht worden sind, bei denen unserer Meinung nach ein wichtiger Mechanismus über die Fehlstellen von Sauerstoffgruppen abläuft.

Die Untersuchungen von Laktose und magnetischer Materialien werden ebenfalls besprochen. Dabei wird auch diskutiert, welche Veränderungen am Aufbau vorgenommen werden müssen, um publizierbare Ergebnisse beziehungsweise ein Signal zu erhalten.

Die nächsten wichtigen Verbesserungen am Aufbau sind die Verwendung eines ausbalanciertem Detektors und die Kühlung des LN-Kristalls. Erstere sollte zu einem besseren Signal-zu-Rausch-Verhältnis führen und die zweite zu einem stärkerem THz-Puls mit größerer Bandbreite. Wenn die THz-Pulsstärke stark genug ist, sollte es möglich sein, niederfrequente Moden anzuregen, die zum Beispiel in der Doppelhelix der Desoxyribonukleinsäure (DNS) oder in Proteinen vorkommen. Auf diese Weise würden neue Erkenntnisse darüber gewonnen werden können, wie sich delokalisierte THz-Moden auf lokale Moden auswirken, deren Zusammenspiel bis jetzt noch kaum untersucht wurden.

Acknowledgements

In the next few lines, I want to acknowledge a couple of people, who were involved in some way in my PhD:

Nils Huse for giving me the possibility to experience a PhD project.

Katrin Adamczyk, die mich bei meinem Projekt angeleitet hat und einfach echt Ahnung hat. Am besten nach dem ersten Kaffee anzutreffen.

Amul Shinde for showing me the way of a warrior - fighting the PhD. I think I will go to India at some point.

Miguel Ochmann, fast immer strahlend.

Matthias Ruppert für unsere Fehde im Labor, damit wir was zum Quatschen, Lachen und Streiten hatten.

Stephan Niebling, der einfach recht damit hat, einen Hüpfball im Büro zu haben. Und jetzt haben alle beim MPI auch einen bekommen.

All other members of the Huse group for a lively working atmosphere.

Arwen Pearson, who was there for giving me advices and pointing out the project's direction.

Toru Matsuyama, dem ich all meine Elektronik-Fragen stellen konnte.

Meinen Eltern, die immer gesagt haben, dass ich das schon schaffe.

Ma grand-mère Lea, qui m'a montré qu'on n'a pas besoin de beaucoup pour être heureux.

Meiner Großmutter Erna, die leider im Dezember 2016 verstorben ist und meine Abgabe nicht mehr miterleben kann. Ich werde versuchen, mir einen grünen Daumen wie ihren anzueignen.

Meiner Freundin Rebecca, die die richtige Einstellung zu Arbeit und Arbeitszeiten hat.

Contents

List of Abbreviations

AgGaS$_2$	Silver Thiogallate
BBO	Beta-Barium Borate (β-BaB$_2$O$_4$)
cw	continuous wave
DFT	Density functional theory
EM	Electromagnetic
EOS	Electro-optic sampling
FEL	Free-electron laser
GaAs	Galliumarsenid
GaP	Galiumphosphite
GO	Graphite oxide
IR	Infrared
LiNbO$_3$	Lithium niobate
LN	Lithium niobate
MgO	Magnesium oxide
MIR	Midinfrared
MOKE	Magneto optic kerr effect
Nd:YVO$_4$	Neodymium-doped yttrium orthovanadate
OPA	Optical parametric amplifier
SHG	Second harmonic generation
THG	Third harmonic generation
THz	Terahertz
THz-TDS	Terahertz time domain spectrometer
Ti:Sa	Ti:sapphire
TTM	Two temperature model
ZnTe	Zinc telluride

Chapter 1

Introduction

1.1 Terahertz electromagnetic radiation

In the electromagnetic spectrum the THz frequency region lies between the infrared and radio frequencies as shown in figure 1.1. In the literature it is sometimes referred to as far-infrared (FIR). Since in photonics different units are used to describe light, the following describes 1 THz in terms of frequency, wavelength, wavenumber, energy and temperature:

$$1THz \leftrightarrow 10^{12}Hz \leftrightarrow 300\mu m \leftrightarrow 33.3cm^{-1} \leftrightarrow 4.13meV \leftrightarrow 48K. \qquad (1.1)$$

A term which was used in the past for that frequency region was "terahertz gap" since it lies between the fields of electronics and optics. Only in the 90s (of the last century) that gap was bridged [6, 7] and this new part of the EM-spectrum was available, thanks to ultrafast laser pulses [8]. Ever since the field expanded quite strongly and nowadays different sources like crystals (organic and inorganic), antenna structures [9, 10] or FELs [11, 12] can be used to create EM waves of that frequency range. The detection of the THz radiation can be done in the same way using crystals or antennas. These methods have the advantage that not only intensities but electric fields are measured, and so the amplitude as well as the phase can be extracted. It
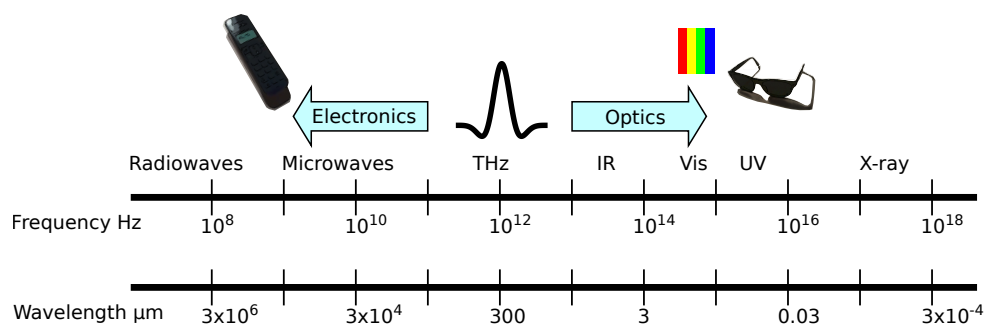

FIGURE 1.1: Electromagnetic spectrum

gives the possibility to calculate various optical characteristics [10].

In terms of usage, the THz scientific field is still expanding. Some examples of applications where that radiation already has been used are security systems, material science [13], medicine, biology and communication:

In the research field of security systems, THz radiation is used by body scanners at airports. Another example is the investigation of drugs and explosives in letters for instance [14]. Also the field of metamaterials (materials which properties are not found in nature) was widely studied [15, 16, 17, 18]. Spectra from different molecules were recorded, showing the low frequency absorptions [19, 20] and further extend the knowledge of the characteristics. Since THz radiation is sensitive to water, one idea is to use it to detect skin cancer [21]. In that way also the localisation and concentration of water in a leaf can be studied [22, 23]. Nowadays WLAN (Wireless Local Area Network) systems operate in the GHz region but for higher transmission rates the next step is to go towards THz or IR regimes which could accelerate the transfer of data. However this is still far in the future [24].

With the THz frequency available new pump-probe experiments (explained in 1.2) could be done within this supplementary range in which the dynamics of lower frequency modes or free carriers play a role [25, 26].

The aim of this work was to develop a versatile system in which the THz spectrometer could be connected to an OPA, a higher harmonics generating tripler or another light source. Additionally, THz should be used as a pump or probe but in this work the focus was to use it as a probe beam. The combination with an OPA was already mentioned in the literature by Backus et al. [5]. In fact, experiments using the pump-probe methods were performed shortly after THz radiation became available [27, 25, 28].

Certainly the combination of different light sources for time dependent measurements will increasingly be used and new insights for all kinds of materials will be gained this way.

1.2   Pump-probe spectroscopy

One way to study time dependent phenomena of various types is to do pump-probe spectroscopy with lasers. It gives the possibility to look at ultrafast events (femtosecond regime). In the case of samples described later, two laser pulses are used. The pump pulse excites the sample and the probe pulse is sampling the behaviour induced by the pump pulse, see figure 1.2. By varying the time delay between both pulses a time dependency can be recorded.
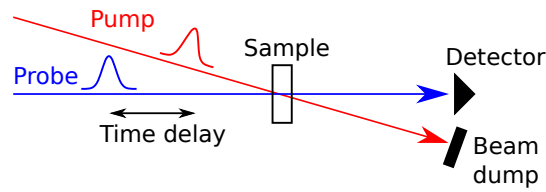
FIGURE 1.2: Pump-probe scheme: the pump beam (red) excites the sample and the probe beam (blue) is sampling the induced change. If a time dependence exists, it can be resolved by a delay between both pulses.

1.3 Laser system

The source for the THz setup (and all other setups like the OPA in the lab) is an amplified pulsed femtosecond laser system (as shown in figure 1.3, Spitfire Ace, Spectra-Physics). It consists of a mode locked Ti:Sa oscillator (Mai Tai SP-Series, Spectra-Physics) system (see 1.3.1) running at $\sim$84 MHz, with $<$ 50 fs pulse width, a peak power of $>$ 95 kW and TEM$_{00}$ outgoing mode (transverse electromagnetic mode). This high repetition laser light is guided into the amplifier system. There, oscillator pulses are picked out by Pockels cells to be amplified. The physical process of enhancement used is called chirped pulse amplification (see 1.3.2). It results in an outgoing laser pulse having a center wavelength of 800 nm, 3 kHz repetition rate (can be modified by dividing through integer numbers), a maximum pulse energy of 1.6 mJ and a minimum pulse width of 95 fs. In appendix A, the measured beam profile is represented.
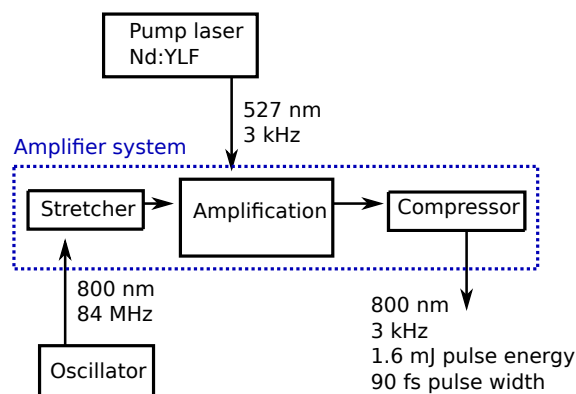

FIGURE 1.3: Sketch of the amplified laser system. The oscillator delivers pulses into the amplifier system that consists of a stretcher, an amplification oscillator and a compressor. They are amplified by a pump laser and kicked out for use in experimental setups.

1.3.1   Mode locking

The mode locking process is used in the oscillator system. Here a Nd:YVO$_4$ is the continuous wave pump laser (532 nm by frequency doubling SHG with LBO) for the Ti:Sa crystal (absorbs between 400 and 600 nm, emits between 670 and 1000 nm). The excited states of the crystal are spontaneously emitting light after being pumped in a resonant cavity. These photons are able to induce stimulated emission which starts the lasing process. By choosing special boundary conditions, e.g. the cavity length L, the eigenfrequencies of the resonator are fixed as are the longitudinal modes in the system. Mode locking is caused by all the modes being synchronized and having a fixed phase relative to each other. This gives rise to constructive interference that creates short pulses (in the fs regime) of high power. A single soliton wave packet is created this way which circulates the resonator. The leakage through one end mirror, the so-called output coupler, is used for experiments or is transmitted to the amplifier system with a time period ($\sim$12 ns) of one round trip in the cavity [29, 30, 31].

1.3.2   Amplification process

A short explanation of the amplification process is that the seed laser from the oscillator system is amplified by the energy of a pump laser.

To be more precise, the amplification system using the chirped pulse amplification process is divided into stretcher, amplifier and compresser (see blue dotted box of figure 1.3). First the width (in the frequency domain) of the seed pulse coming from the oscillator is stretched (by a factor of 10^4) by a grating. This broadened pulse is then sent into the amplification area via a Pockels cell which opens only every $0,\overline{3}$ ms. Consequently, the repetition rate is reduced this way from 84 MHz to 3 kHz. In the amplification district a Ti:Sa crystal is positioned in a cavity in which the seed pulse makes round trips (here around 12 times, depending on the saturation in the process). This crystal is pumped with a Nd:YLF laser (527 nm, after SHG) and by every pass of the seed pulse, it is picking up energy (increase of a factor of three or four, not linear). After gaining the desired (maximum) energy, the pulse is kicked out of the cavity by passing a Pockels cell and sent to a compressor, which inverts the process of the stretcher. It shortens the pulse almost back to its original width. This whole process enables a pulse energy increase from nJ to mJ [30].

Chapter 2

Terahertz setup

This chapter describes the design of the THz spectrometer (see figure 2.1) that has been constructed as part of this work. It includes the setup itself with the generation and detection of the THz radiation, the related electronic parts as well as the data analysis. At the end, different combinations of the setup are introduced. Already in figure 2.1 the beam path of the IR is depicted, since it is one major asset of the setup. Overall it should be a versatile pump-probe spectrometer with a wide range of pump and probe radiations, from THz to the visible. In the following the beam path is explained:

A fraction ($\backsim$50%) of the 800 nm fundamental of the pulsed fs-laser source (see section 1.3) is sent into the setup (top left corner in figure 2.1) and split into two beams by a 10:90 (T:R) beamsplitter. One beam is guided to a mechanical delay stage, in order to control the relative time delay with respect to the second beam that is guided for instance to a tripler box, described later in section 2.11. From the beam passing over the delay stage, a leakage through a mirror is used for electro optic sampling (EOS, red dotted line) and the other for generating a THz pulse in a lithium niobate (LiNbO$_3$, LN) crystal via optical rectification (see 2.1.1). Before striking the LN crystal, the beam is conditioned with two telescopes, before and after a grating (2000 lines/mm). The first telescope with cylindrical lenses scales down the horizontal part of the beam by a factor of 2 (1 inch lenses), the second scales the whole beam down (2:1) (2 inch lenses). Off axis parabolic mirrors guide and focus the THz pulse to the sample position and afterwards onto a birefringent crystal (e.g. GaP or ZnTe) for scanning the pulse (see 2.2). If refered to the parabolic mirrors in this thesis, the counting starts with the first after the LN crystal until the fifth in front of the EOS crystal, as done in figure 2.1.

The IR beam (blue line in fig. 2.1) is generated in an OPA, not shown here (see section 2.10), and focused onto the sample, with appropriate optical components. On the long run, the idea is to guide this IR beam afterwards into an imaging spectrograph and detect it by a multichannel detector (not shown in the sketch). This
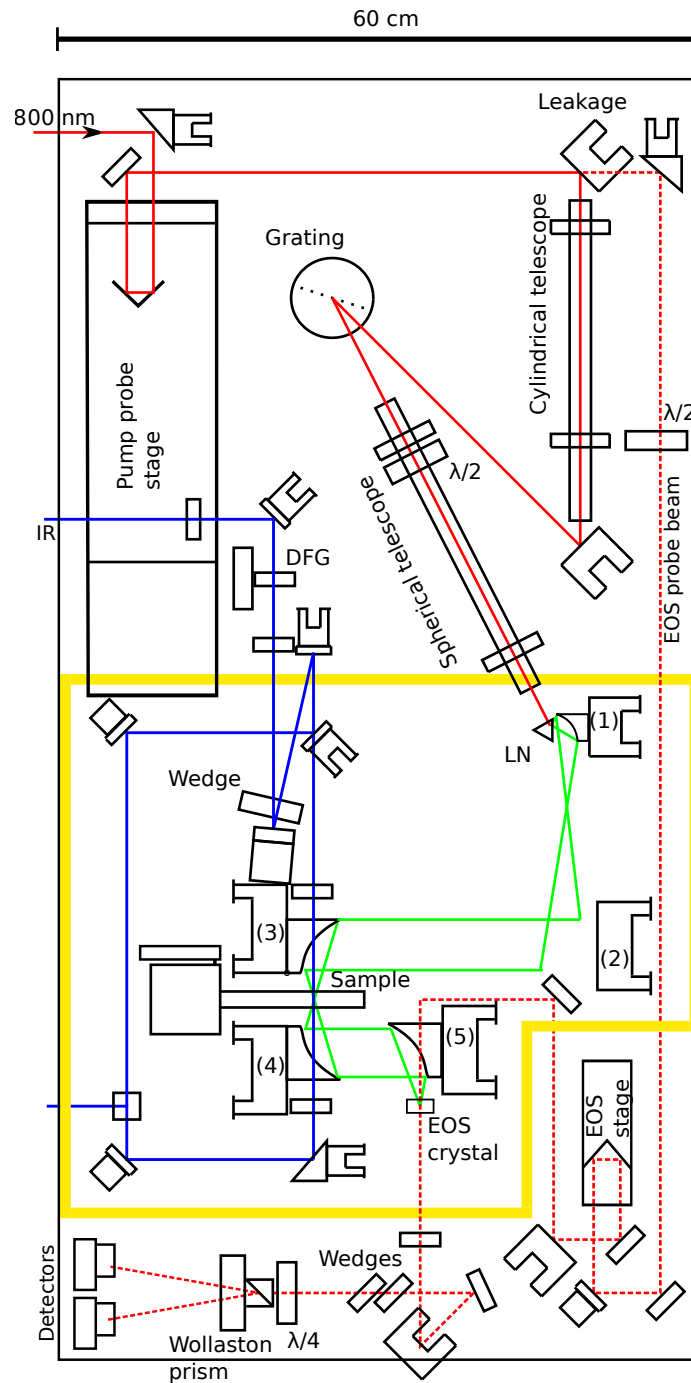
FIGURE 2.1: Two colour pump-probe setup. The incoming 800 nm beam (red line) is split in one part for generating THz radiation (green) in the LN crystal. There the pulse is guided via parabolic mirrors onto the sample position. The IR beam (blue) is coming from an OPA (not shown) and also guided to that position. Afterwards the path towards a spectrometer is also sketched. The 800 nm leakage part (dotted line) is used for the electro optical detection of the THz.

In appendix B.3 the sketch is shown on the breadboard grid.

configuration allows it to use the THz light as a pump or probe beam in combination with IR light, also usable as pump or probe.

How the THz beam can be aligned is depicted in appendix B and a list of the used non common optomechanics and optical components is given in appendix C.

2.1 THz generation

2.1.1 Optical rectification

When an external electrical field E is applied to a material, a polarization P arises and is expressed as

$$\vec{P} = \epsilon_0 \chi \vec{E} \tag{2.1}$$

where ϵ_0 denotes the vacuum permittivity and χ the electrical susceptibility.

Equation 2.1 is sufficient for weak fields and is linear. Whereas, if the electrical field originates from a pulsed laser, like the one described in section 1.3, high field strengths can be achieved. Higher order terms do arise then. Hence, the linear relation of equation 2.1 must be extended and the polarization can be described with a power series:

$$P(\omega) \propto \sum_n \chi_n E^n = \chi_1 E^1 + \chi_2 E^2 + \chi_3 E^3 + ... \tag{2.2}$$

with χ_n the electric susceptibility, E^n the electric field and n the order.

At this point the term of nonlinear (NL) optics is used. After the linear part of equation 2.2, the second order term arises. Its effects can only be seen in non-centrosymmetric crystals, as all other even numbered orders because of P(-E)=-P(E). The second order susceptibility is in the order of $\chi_2 \sim 10^{-12}$ m/V. Consequently, to create effects described by this relation, the incoming electric field should at least be in the order of 10^6 V/m. Typically, field strengths of 10^8 V/m are being used for getting a nonlinear response in a system. The third order susceptibility is already in the order of $\chi_3 \sim 10^{-24}$ m^2/V^2 and neglected here [32].

As described above, the external field induces a polarization into the system. The time evolution of that polarization can be deduced from the Maxwell equations and is expressed as

$$\frac{1}{\epsilon_0 c^2} \frac{\partial^2 P^{NL}}{\partial t^2} = \nabla^2 E_e - \frac{n^2}{c^2} \frac{\partial^2 E_e}{\partial t^2} \tag{2.3}$$

with n the refractive index of the material and c the speed of light. It results in an emitted electric field E_e, induced by the polarization.

In case that the irradiated electric field is strong enough to induce a nonlinear polarization, the second order term generates light at different frequencies. Assuming that the electric field can be expressed with two terms $E_{01} = E_1 cos(\omega_1 t)$ and

$E_{02} = E_2 cos(\omega_2 t)$ as E = $E_{01} + E_{02}$, the polarization can be calculated as follows: First rewriting the cosine function as

$$E_{01} = \frac{E_1}{2}(e^{i\omega_1 t} + e^{-i\omega_1 t}) \tag{2.4}$$

$$E_{02} = \frac{E_2}{2}(e^{i\omega_2 t} + e^{-i\omega_2 t}) \tag{2.5}$$

and taking the square of the electric field since the second order process is of interest

$$E^2 = (E_{01} + E_{02})^2. \tag{2.6}$$

Inserting the single electric fields results for the second order polarization in

$$\frac{P^2}{\chi_2} \sim \frac{E_1^2}{2}(1 + cos(2\omega_1 t)) + \frac{E_2^2}{2}(1 + cos(2\omega_2 t)) + \tag{2.7}$$

$$E_1 E_2 cos((\omega_1 + \omega_2)t) + \tag{2.8}$$

$$E_1 E_2 cos((\omega_1 - \omega_2)t). \tag{2.9}$$

Equation 2.8 represents the process of sum frequency generation (SFG) and equation 2.9 the process of difference frequency generation (DFG), depicted in figure 2.3. In addition two other processes are taking place. They are responsible for second harmonic generation (SHG) and optical rectification (OR). In the equations above a continuous wave was used for deriving the processes taking place in a non-centrosymmetric material. It can lead to the DFG process generating THz radiation. To get a strong THz wave out of the crystal all the single waves generated by the process must add up. This is accomplished by an effect called phase matching described in more detail below 2.1.2 [9]. In fact, phase matching controls which process of the four introduced above dominates. But here a laser pulse is used for generating the THz pulse. For a high photon conversion efficiency in the crystal, the OR process should be favored for generating THz radiation. Therefore, two processes are taking place in the crystal, SHG and OR. The latter one is responsible for the THz pulse [33]. In figure 2.2 the process is shown with a pulse.
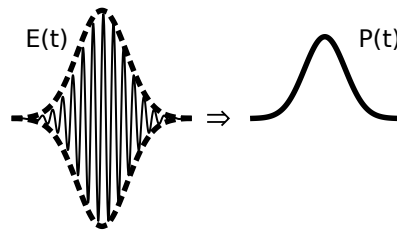

FIGURE 2.2: E(t) depicts the 800 nm pulse that generates a polarization P(t) in the non-centrosymmetric material.

The 800 nm pulse E(t) induces a polarization $P(t) \sim |E(t)|^2$ in the crystal, which is the origin of the THz field. By calculating the second time derivative of the polarization, as in the equation 2.3, the THz pulse is obtained. It is irradiated by a dipole created by the nonlinear polarization in the crystal.

Besides, one should note that the created THz wave in the crystal is a phonon polariton (see underneath), generated by the 800 nm pulse. One can imagine this mechanism in the following way: the optical pulse is like a flashlight (shining into the crystal) and the THz is a light wave created by that, which couples out at the crystal's edge and that is the THz pulse used for experimentations.
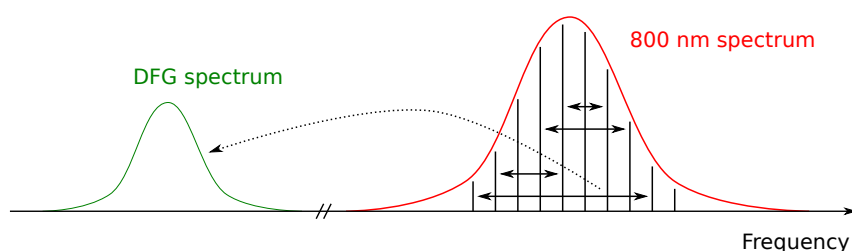
FIGURE 2.3: The green wave packet is created by DFG from the red (800 nm) wave packet by interacting with a non-linear medium.

Phonon Phonons are quantized vibrations of the grid of a periodic system as e.g. a solid state material. They can be seen as waves wandering through the material but also as a quasi particle. One can find 3N different modes in a material that has N atoms in its base. 3 of them are acoustic modes and 3N-3 optical. Acoustic modes are for instance responsible for the propagation of the spoken word in air. The neighbouring atoms are doing a movement in phase. For optical phonons it is the opposite. Therefore, the movement of neighbouring atoms is inverse and the crystal base must have at least two atoms. They are also optical active, so can be excited by a photon.

A phonon polariton is the coupling between the phonon-photon fields (only the transversal optical phonon). It occurs when strong electric fields are applied, like here with the incoming 800 nm pump beam. The generated electromagnetic THz wave is therefore escorted by a phonon wave [34].

2.1.2 Phase matching

The generated waves in a non-linear crystal must add up constructively to gain intensity, so the phase relation between them must be fixed [29]. This is realized if the following equation is fulfilled:

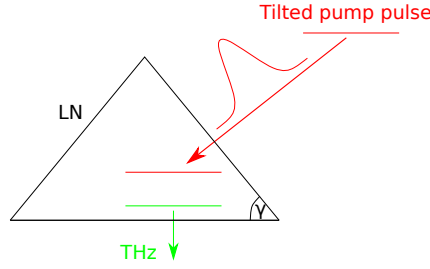$$v_{Opt}^{gr} = v_{THz}^{ph}. \tag{2.10}$$

FIGURE 2.4: Tilted pulse front for phase matching in a LN crystal.

The group velocity of the incoming optical wave packet v_{Opt}^{gr}, should be equal to the phase velocity of the THz wave packet v_{THz}^{ph}, so that it is not overrun and constructive interference occurs. Equivalent to the expression of 2.10, the refractive indexes must match: $n_{Opt}^{gr} = n_{THz}^{ph}$. In ZnTe this condition is naturally fulfilled since the refractive indexes of v_{Opt}^{gr} and v_{THz}^{ph} are nearly the same. But in LiNbO$_3$ which was used here, as the energy conversion efficiency is two times higher than for ZnTe, equation (2.10) is not satisfied due to non matching refractive indexes [4]. Therefore, a tilting must be induced in the incoming optical beam so that the phase matching condition is fulfilled

$$v_{Opt}^{gr} cos\gamma = v_{THz}^{ph} \tag{2.11}$$

where γ is the tilting angle ($\sim 63°$ for LN [35],[36]), as shown in figure 2.4. It is done with the grating placed in the THz pump beam path (see figure 2.1).

2.1.3   Lithium niobate

For generating THz radiation, a LN crystal was used. It must be doped with MgO, so that the optical damage threshold is high enough for pumping the crystal convienently. MgO serves as protection. The issue with higher doping, is that the absorption coefficient in the THz regime increases. Consequently, by doping, the refractive indexes are changed, but the one for the extraordinary part stays nearly stable, independently from the doping level, which is a benefit for processing [37]. That is also the reason why there is a halfwaveplate in front of the LN crystal which rotates the 800 nm pump beam, therefore enabling higher outcome and fine-tuning. Here a stoichiometric LN crystal with 0.6 mol% MgO was purchased [38].

By slightly changing the angle of the tilted pulse front, the emitted THz radiation maxima can be tuned, when the crystal is cooled. The chilling changes the absorption and higher frequencies can be decoupled. Since the present setup does not yet contain a cooling system, the higher frequencies (above 1.5 THz) are not reachable [39]. In figure 2.5 the grating angles are drawn, in case that it must be dismounted for cleaning.

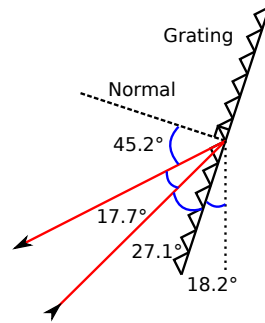FIGURE 2.5: Grating before the LN crystal for inducing a tilt to the
800 nm pulse.

The LN crystal itself is mounted on a xyz stage enabling the pump beam to hit its edge. This way the THz radiation travels the shortest path within the crystal and is minimally absorbed. If the crystal gets damaged by the 800 nm pump beam, it can be moved vertically (for some millimetres) in order to expose an undamaged position to the beam.
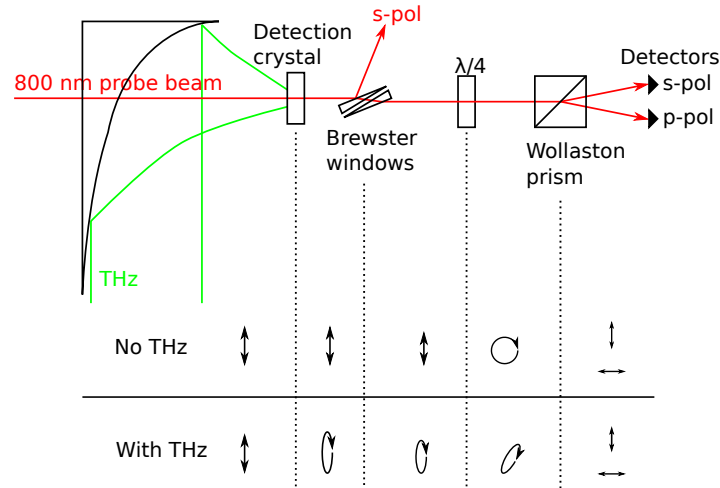
2.2   THz detection - EOS

FIGURE 2.6: Sketch of the EOS unit (in figure 2.1 the 800 nm makes a 90° deflection). The THz (green) is inducing a polarization change in the birefringent detection crystal which changes the polarization of the transmitted 800 nm probe beam (red). For better contrast it passes a pair of brewster windows and a $\lambda/4$ plate. The latter one is setting the equilibrium state for no applied THz field. The Wollaston prism is separating both s- and p-polarization parts of the beam. Each one hits one detector. Below the sketch, the polarization change of the 800 nm is shown, with and without applied THz field.

The scheme used to detect the THz transient field is electro optical sampling (EOS), shown in figure 2.1 and in more detail in figure 2.6. The THz pulse is focused onto an electro-optical material, which changes its refractive index when an external electric field is applied (Pockels effect). These non-centrosymmetrical objects (mostly crystals) are for example GaAs, ZnTe or GaP. The two latter ones are used here [40]. Because of the electric field of the incoming THz field and the birefringence of the crystal, the 800 nm sampling (probe) beam sees a different polarization depending on changes of the THz field. Furthermore, the presence of a sample induces a change in the THz field which is detected by the polarization change in the EOS crystal (or nothing changes if there is no sample).

By detecting the THz pulse this way, one can use the 800 nm probe beam (100 fs FWHM) to scan the THz pulse, which has a much longer pulse length (> 1 ps), as depicted in figure 2.7. With a mechanical stage, the 800 nm are delayed and therefore can raster stepwise the THz pulse. Point by point the THz pulse is recorded. Thus, the phase and the amplitude can be extracted from the measured fields, and used to calculate all the optical coefficients such as refractive index, absorption coefficient,

permittivity and conductivity[41].

For the next explanations, see also the lower part of figure 2.6. Before irradiating the EOS crystal, the 800 nm beam is vertically polarized. Afterwards is has a slight horizontal polarization component, depending on the influence of the crystal induced by the THz. To minimize that polarization ratio, a pair of Brewster windows is inserted, which deviates a part of the s-polarized beam. This enables an enhancement of the THz-field detection [42]. The quarter wave plate is used to determine if there is a THz field applied on the detection crystal or not. It defines the equilibrium state. There is no signal, when the THz field does not reach the EOS crystal[1]. In that case, the 800 nm would get circularly polarized. Thereafter the 800 nm beam is split in its s- and p-polarization parts by a Wollaston prism and detected by a detector system, which measures the difference between both polarizations. If a THz field irradiated the EOS crystal, the 800 nm probe beam is elliptically polarized after passing the quarter wave plate and the s- and p-polarization parts are not equal. The recorded difference is the THz pulse.
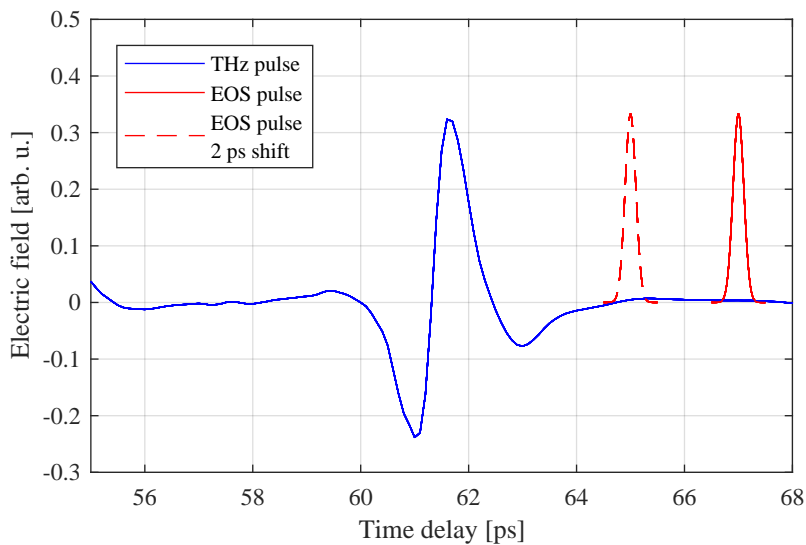

FIGURE 2.7: The THz pulse (blue) is being rastered by the 800 nm EOS pulse (red). Via a delay stage it can be delayed and sample the THz field, e.g. 2 ps later (red dashed). The time delay is kept, like it is displayed by the delay stage.

---

[1]It is set by letting pass the 800 nm probe beam and equalize the signals on both detectors, so that they give zero if subtracted from each other.

2.3   THz measurement

Figure 2.8(A) shows the THz time trace of the pulse, while figure 2.8(B) shows the amplitude spectra calculated via fourier transformation. The detailed data analysis can be read in 2.4. Both measurements have been taken with a 1 mm thick ZnTe (110) EOS-crystal. By comparing the purged and not purged lines, water vapour absorption lines can be seen at around 0.5, 0.7 and between 1 and 1.2 THz [43]. As comparison, the THz pulse measured with a 300 μm thick GaP (110) EOS-crystal is shown in figure 2.9(A), alongside with a calculated THz-spectrum in figure 2.9(B). By comparing both spectra measuerd with the two different EOS crystals, GaP is showing the absorption lines less distinctively. This is as expected according to [44]. The sensitivity of the GaP crystal is lower, which leads to the conclusion that a ZnTe crystal is better suited in this frequency range for the EOS (thicker crystals lead to higher sensitivity). Furthermore, a phonon absorption line from ZnTe arises only at 5 THz. It does not interfere with the emitted band width which goes up to 1.5 THz here. If detecting higher frequencies becomes necessary, GaP can be used up to ~10 THz, since no phonon absorption line lies in the range from 0.2 to 10 THz for that crystal.

Since the EOS crystals are not of equal thickness, the time delay of the measurement can not be the same because otherwise the reflected pulse in the crystal of the THz would superimpose on the data. It leads to a better resolution for the thicker ZnTe crystal and the back pulses can be seen (reflected pulse within the crystal) in figure 2.9(A) at a time delay of 14 ps.

(A) THz pulse
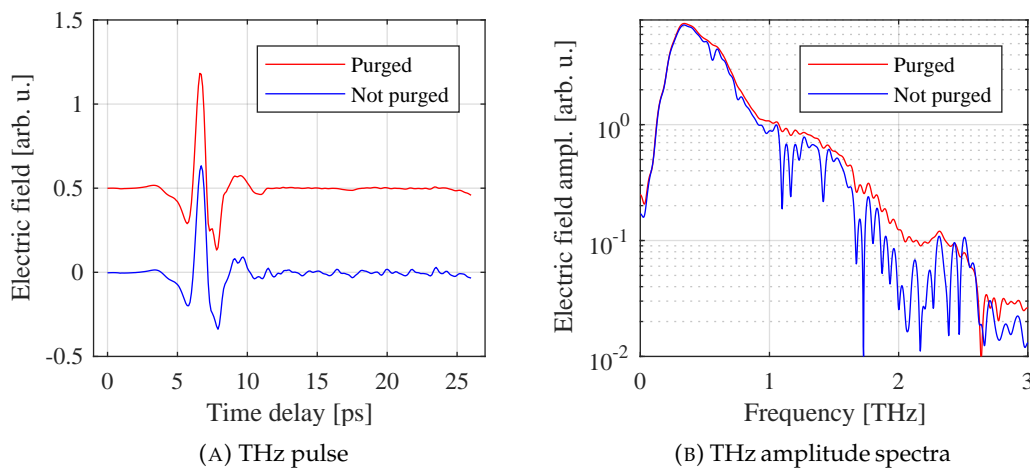

(B) THz amplitude spectra

FIGURE 2.8: The red and blue curves show the recorded THz pulses (A) with and without purging the spectrometer respectively, measured with a 1 mm thick ZnTe crystal for EOS. In (B) the amplitude spectra is shown.
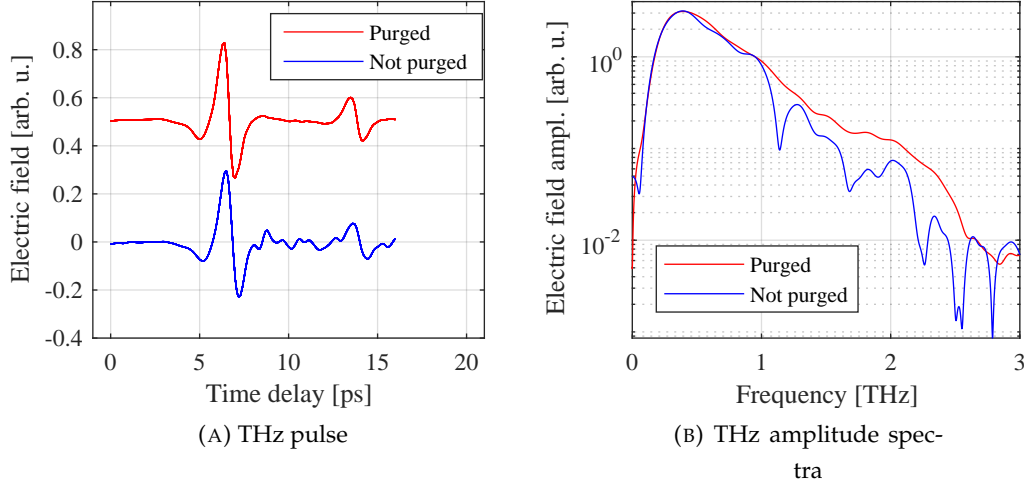
(A) THz pulse

(B) THz amplitude spectra

FIGURE 2.9: The red and blue curves show in (A) the THz transient field with and without purging the spectrometer. A 300 μm thick GaP crystal was used. 7 ps after the main pulse the back pulse can be seen. In (B) the spectra are shown.

2.4 Data analysis of a THz pulse

The recorded data is the electric field E(t) of the THz pulse over the time delay. This pulse is set to zero baseline so that a possible offset is rectified by subtracting the mean of the first data points before the pulse arrives. Additionally, one can also integrate the upper and lower part of the pulse curve (around the horizontal axis) which must, after subtracting one part from the other make zero. An overlaid supergaussian[2] is afterwards multiplied with the pulse, so that the starting and ending values of the pulse are smoothly converging to zero, as seen in figure 2.10 for a pulse recorded with GaP (pulse from figure 2.9). At the end of the pulse, zeros (zero padding) are added which artificially gives a higher resolution to the spectra. By doing this, it is assumed that all the radiating processes in direction of beam propagation have decayed. $\frac{1}{T}$, with T the length of the time trace gives the frequency step in the spectrum f_{step}. This adding of zeros makes only sense until f_{step} is small enough to resolve the natural linewidth of the processes in that frequency region. It could also be said that this zero padding is doing an interpolation of the data (with the sine and cosine functions).

The THz pulse is recorded by rasterizing the pulse, in discrete time steps t_{step} (see figure 2.7) which gives the maximum frequency value $f_{max} = \dfrac{1}{2t_{step}}$ that can be

---

[2]A supergaussian is a gaussian function with its exponent being of power n. With higher n the curve edge becomes steeper.

measured after the Nyquist–Shannon sampling theorem [45]. Here, the pulses were recorded in 100 fs time steps equalling an upper frequency limit of 5 THz. That is sufficient since the bandwidth of the THz pulse does not exceed 1.5 THz.

Finally the time trace of the pulse (cyan curve in figure 2.10(A) plus the zero padding not shown here) without the back pulse (which would result in a ringing or oscillation on top of the data) is fourier transformed (fast fourier transformation for numerical data) to the frequency domain via

$$E(t) \Rightarrow E(\omega) \tag{2.12}$$

yielding E(ω). Afterwards the absolute value of E(ω) is taken.
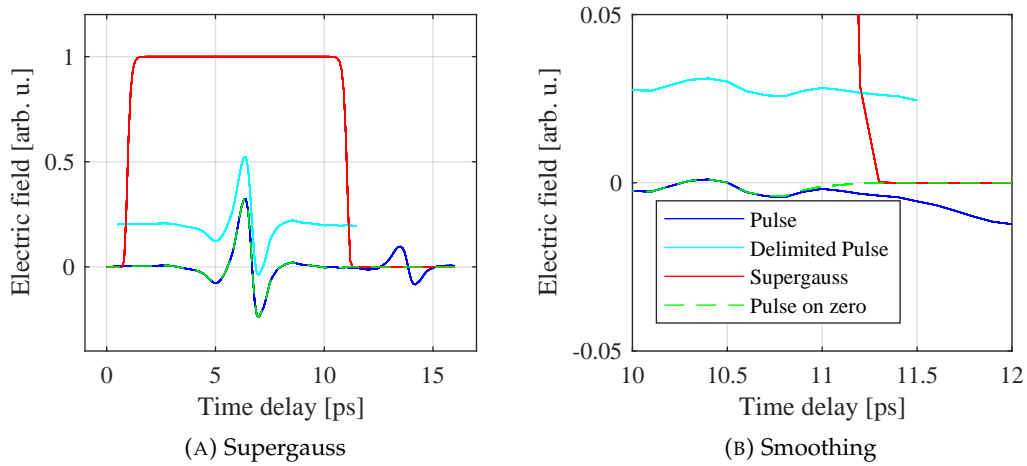

(A) Supergauss

(B) Smoothing

FIGURE 2.10: In blue the whole time trace is depicted (A) and in cyan the delimited part for processing. Red shows the supergaussian, that is multiplied with the pulse. Dashed green is the smoothed pulsed, zoomed in (B).

Fourier transformation The fourier transformation (FT) is widely used in many fields as for instance signal processing, acoustics and others. In the following equation the general fourier transformation is written

$$Ff(y) = \frac{1}{2\pi} \int_{-\infty}^{\infty} f(x)e^{-iyx}dx \tag{2.13}$$

with a normalisation factor of $1/(2\pi)$ that differs depending on literature reference or scientific field (the importance is to stick to one formalism). f(x) is the function of x that is transformed to Ff(y) with the variable y.

Here, x is the time and y the frequency, or the transformation of the THz pulse to its spectrum. The THz pulse is transformed from the time domain to the

frequency domain. The new function is complex valued. For gaining the transmission t through an object the following relation can be used

$$t = \frac{E_{sam}(\omega)}{E_{ref}(\omega)} = A e^{i\Delta\phi} \tag{2.14}$$

with E_{sam} being the electric field passing through the sample, E_{ref} the electric field of the reference beam, A the amplitude and $\Delta\phi$ the phase retardation between the two pulses. As an example, one wave is travelling through air (reference) and the other through a sample, the phase retardation of the second pulse can be calculated via a fourier transformation. The occurance of a phase shift can already be seen by the delayed pulse going through the object arriving at a later time at the detector.

2.5   Water absorption lines

THz radiation is absorbed by water vapor in the ambient air, which makes purging the setup with dry air or nitrogen necessary for certain measurements. If the absorption frequency of the sample coincided for example with water absorption lines it would be problematic if it was to be analysed. For instance, the lactose absorption line at around 0.53 THz overlaps with the water line at around 0.56 THz and superimpose (see chapter 4 or figure 2.11).

In figure 2.12 the spectra of a purged and non-purged setup are shown. Clear absorption lines can be seen and can be associated with the ones reported by van Exter et al. [46] who measured them in a TDS system. The ringing arises from the FT of a measurement, for which the purge system did not sufficiently dry the air. An assignment of absorption lines to transitions can be done according to the work of Hall et al. [47, 48]. They also measured the aborption of water vapor and e.g. for the line at $\sim$0.56 THz a transition from $1_{01} \rightarrow 1_{10}$ was calculated. This transition is read as J_{cd}, with J denoting the asymmetric rotor energy level (the water molecule is a asymmetric rotor), c the prolate symmetric rotor quantum number and d the oblate symmetric rotor quantum number. Furthermore absorption lines are listed in Table II of the publication [47].

From the measured absorption lines and because THz is strongly absorbed by LN at frequencies above 1 THz, the bandwidth of the spectrometer is identified from 0.2 to $\sim$1.5 THz.
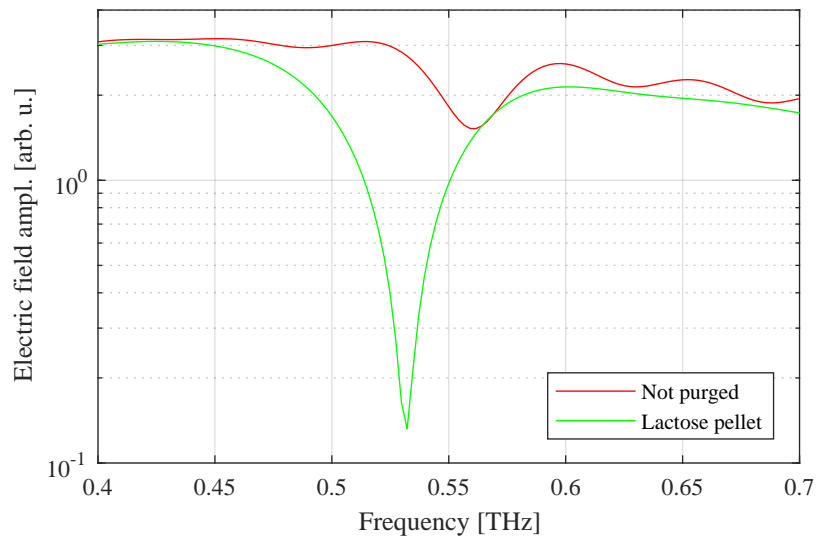
FIGURE 2.11: The red line shows the water absorption line at 0.57 THz and the lactose absorption at 0.53 THz is in green. The lactose sample was in a pellet form with a mixture of 230 mg lactose and 220 mg of PTFE.
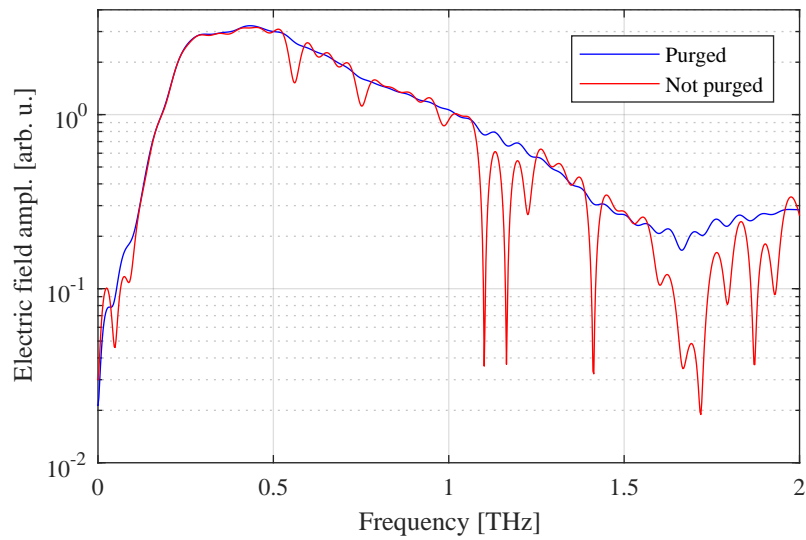

FIGURE 2.12: THz spectra with a purged setup (blue) and without purging (red) it.

2.6 Electronics

The signal detection is done by measuring the change in polarization of the 800 nm probe beam, induced by the THz field in the detection crystal (birefringent) as described in 2.2, in which the EOS system is described. Several possibilities can be used for measuring and two are briefly discussed in the following.

In the THz community, a lock-in amplifier is mostly used. The detection signal could come from a balanced detector. In order to obtain a reference signal, a chopper is positioned in one of the beams that either generates THz or is used for detection. But with the laser-system's low repetition rate of 3 kHz, one could conclude that the signal to noise ratio would be better if single pulse detection was used. (Also a lock-in amplifier plus GPIB card are quite expensive.)

The detection system used here is realized by two separate photodiodes, which emit a current that is sent into an integrating amplifier like the IVC102[3] (which can read out positive and negative currents). One of the diodes is hit by the s-polarized light beam and the other is hit by the p-polarized part of the EOS beam that is separated by the Wollaston prism. The integrator[4] is triggered by two logic inputs to gate the integration for recording the signal and for resetting the capacitors (which are physically the integrators). The latter ones are set to zero this way. In figure 2.13 a sketch of the detection unit is shown. The integrated signal is readout by an analogue digital (a/d) converter (which transcribes the information into a digital signal so that a computer can grab the data). All logical signals must be sent at specific times to avoid an overlap which would result in faulty data. Therefore the 3 kHz signal sent out by the laser system is used as master internal clock. It is delayed by a delay generator but that could also be done with the IC 74HCT123. The disadvantage of that configuration is that the subtraction of both s- and p-polarization signals only happens at the end, i.e. in the software of the computer. This gives rise to an inferior signal to noise ratio compared to the alternative described in the following.

The method described next, is what will be implemented as future improvement of the detection part of the setup. A balanced detector designed by the Electronic Service Unit of the Max Planck Institute (MPSD) will be used. The system uses two photodiodes encased in a single box. Their outgoing current is directly subtracted before going into the integrator. This should strongly decrease the signal to noise ratio.

(In any case, if the photodiodes are operated with batteries, one should regularly check their single response. When the end of the lifetime of the batteries is close, it is better to replace them in advance.)

---

[3]Burr-Brown Corporation
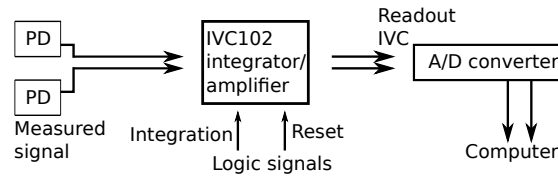[4]Build by the Electronic Service Unit of Max Planck (MPSD)

FIGURE 2.13: Sketch of the electronic detection unit.

2.7 Pump-probe with THz

The introduced THz setup allows the use of a THz pulse as either pump or probe pulse, while the second beam e.g. in the IR is the probe or pump. A possible geometry to achieve that which was used in the described setup, is shown in figure 2.14. The collimated THz beam's diameter exceeds the one of the second beam by a factor of 10. This is why 2 inches off-axis parabolic mirrors with holes are used which let the second beam pass and which enables overlapping at the sample position. In general the pump beam should be at least $\sqrt{2}$ times bigger than the probe beam, so that the probe beam hits a homogeneously irradiated sample.
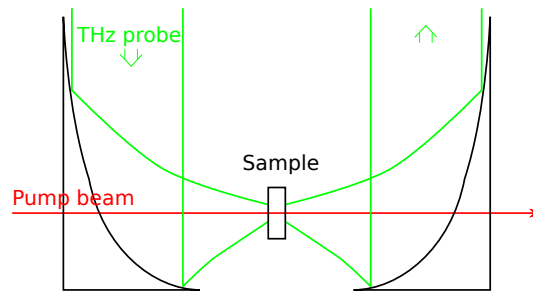
FIGURE 2.14: Off axis parabolic mirrors focus the THz beam onto the sample and holes enable a second beam overlap onto the sample.

2.8 THz beam profile

2.8.1 Divergence of LN crystal

To correctly position the first off-axis parabolic mirror, the divergence of the THz radiation emitted from the LN crystal was measured by cutting the THz beam in front of a pyrodetector. As seen in figure 2.15, after approximately 14 mm from the LN outcoupling surface, the vertical and horizontal divergence are equal and the first off axis parabolic mirror was positioned there. The full opening angle in horizontal direction is 5.5° and 3.7° in vertical direction. For comparison see reference [49, 50].
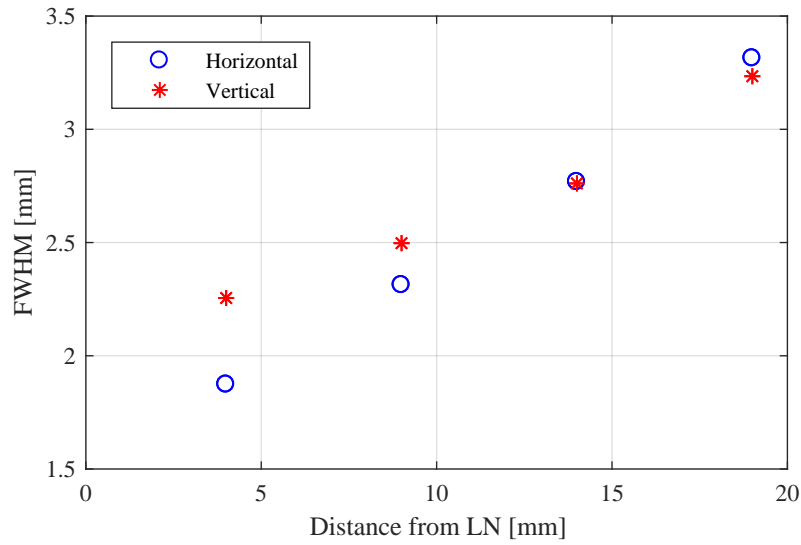
FIGURE 2.15: Divergence of THz radiation after LN crystal.

2.8.2 Sample position

In the two diagrams of figure 2.16, 10-90 cuts of the THz beam around the sample position in horizontal and vertical direction are shown. It was measured by recording the THz peak and decreasing its value by the knife edge method. The spot size has a FWHM of around 0.6 mm in both axes. Horizontally, the beam is expanding uniformly but non-uniformly in vertical direction. This means that the beam is going diagonal through the sample position at the vertical axes.

(A) Horizontal
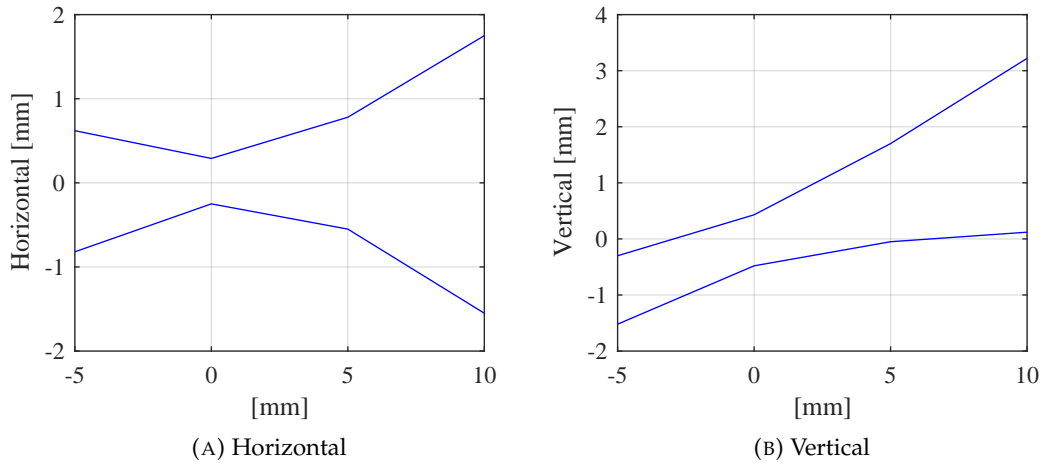
(B) Vertical

FIGURE 2.16: 10-90 cut through the THz beam at the sample position. In (A) the horizontal part is shown and in (B) the vertical part. The y axis depicts in both figures the beam propagation direction.

2.8.3 Collimated THz beam

Results of knife edge measurements shown in figures 2.17 confirm that the collimated THz beam hits the third and fifth off-axis parabolic mirrors in the center. No error function fit was necessary.

(A) Before 3rd parabolic mirror

(B) Before 5th parabolic mirror
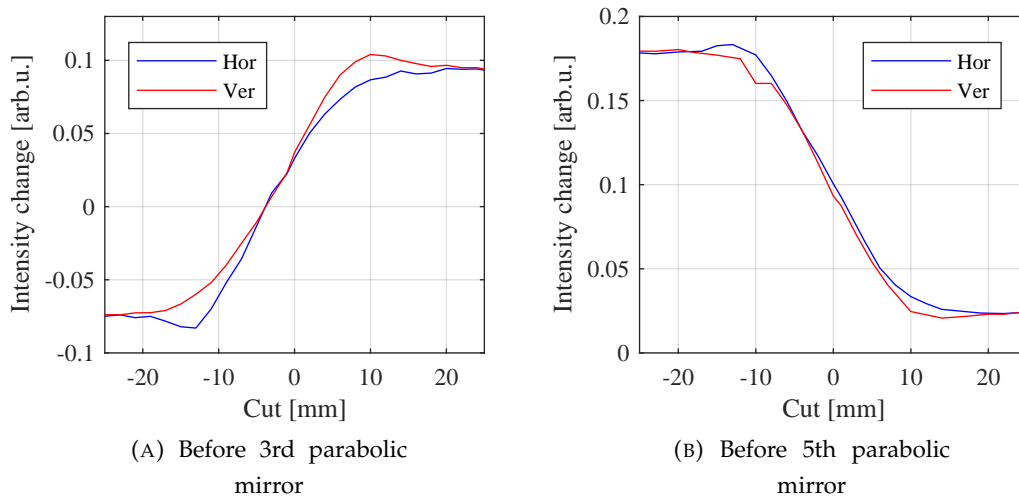
FIGURE 2.17: Profile of the collimated THz beam. Hor stands for horizontal and Ver for the vertical cut.

2.9 THz beam power

Depending on the orientation of the half waveplate in front of the LN crystal, the THz generated is more or less efficient (in vertical orientation maximal). For checking its behaviour, measurements were performed and in figure 2.18(A) the change of the THz peak with respect to the rotation angle of the $\lambda/2$ plate is shown. The blue curve shows the peak at a fixed EOS stage position and the red one tracks the maximum of the THz peak with the EOS delay stage. The difference in peak intensity arises due to an output power decrease of the laser system over time (between both measurement sets). It should be noticed that the THz field does not go down to zero and that depending of the angle, the maximum THz peak is shifted in time (not shown in the figure). This is because the $\lambda/2$ plate delays the beam depending on the angle and rotates the polarization axes[5].

In figure 2.18(B) the power measured by a digital powermeter is shown with respect to the $\lambda/2$ angles. The output power follows the one of the THz peak and has a maximum of 185 μW (62 nJ). In the LN pump beam path a power of 2.2 W (0.73 mJ) was measured, yielding a conversion efficiency of $1*10^{-4}$ on that day (20% power loss at the grating taking into account).
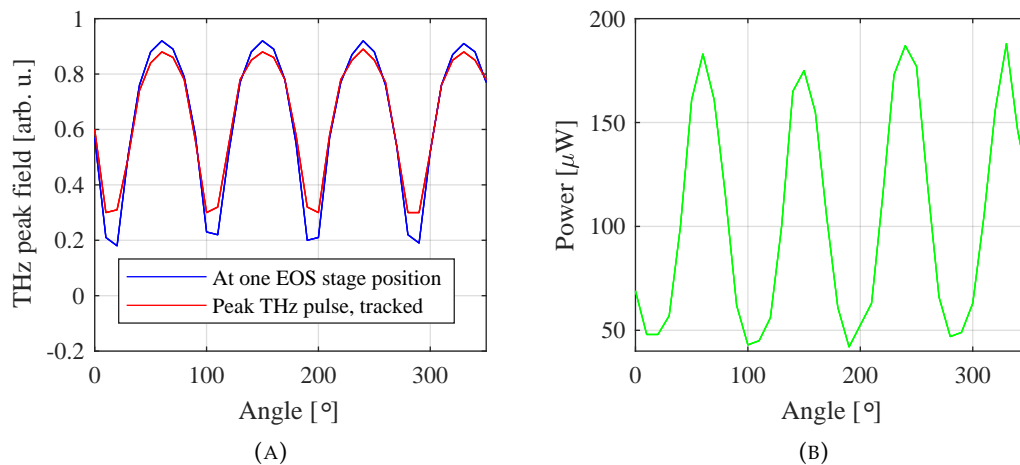
FIGURE 2.18: In (A), the change in the THz peak is plotted vs the angle of the $\lambda/2$ plate. The blue curve shows the peak when the EOS stage is at the position where one is at the THz peak. If the THz peak is tracked, the rotation of the plate results in the red curve. (B) shows the measured THz power with a powermeter at the sample position.

---

[5]The $\lambda/2$ wave plate can retard one component of the transmitted light polarization for half a wavelength. Therefore, it can rotate the polarization axes from linear polarized light. A $\lambda/4$ plate is retarding one projected polarization part of a transmitted beam for a quarter of the wavelength. This way, linear polarized light can become circular polarized and the other way round [51].

To check if the power measured by the powermeter shows reasonable values, another detector was used and the results are compared in figure 2.19 and 2.20, at the sample and the EOS crystal position, respectively.

The horizontal axis shows the orientation of the $\lambda/2$ plate, which turns the polarization of the 800 nm pump before the LN crystal. The efficiency of the THz generation decreases with increasing deviation of the polarization plane from vertical. This is indicated by the decrease of measured power (see figure 2.18). Note that figure 2.20 compares the measured pulse energy of the powermeter and the pyrodetector (Microtech Instruments Inc.). Both were positioned after the last off-axis parabolic mirror. The pyrodetector is specified for the THz frequency region emitted by the LN, but the range of the powermeter is limited up to the mid infrared region. For maximum reliability the use of a pyrodetector is recommended, but due to its size (10 cm long) it cannot be installed at the sample position. However, the powermeter detects on the same order the THz pulse energy at the EOS position and therefore the powermeter used in this work for measuring the THz power is a good compromise.

For the measurements in figure 2.19 and 2.20 the 800 nm beam had a power of 2.25 W (0.75 mJ) for THz generation in the LN crystal.
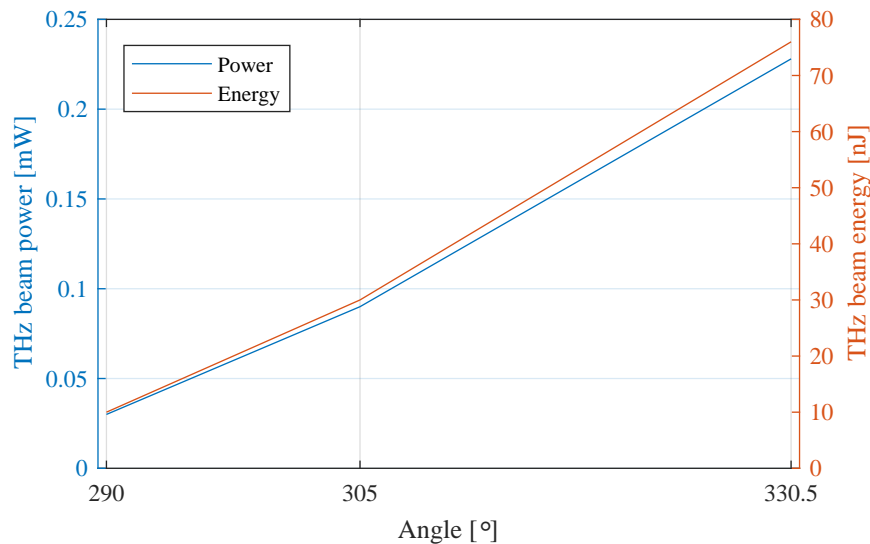

FIGURE 2.19: THz power at the sample position (after the third parabolic mirror) measured with a powermeter in respect to the $\lambda/2$ angle.
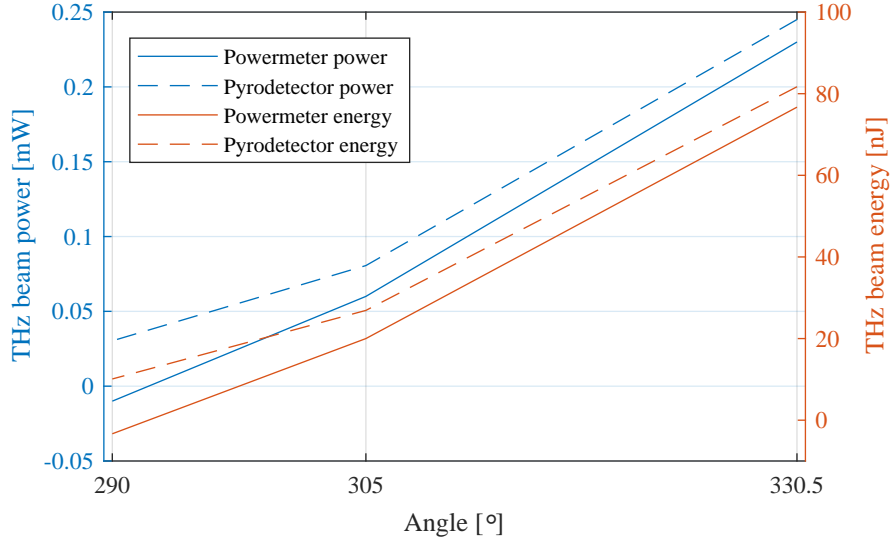
FIGURE 2.20: THz power at the EOS detection position (after the fifth parabolic mirror), measured with a powermeter and a pyrodetector from Microtech.

2.10   Pump-probe extension with an OPA

With an optical parametric amplifier (OPA) it is possible, in a first step, to generate light in the near infrared range with the 800 nm fundamental wavelength provided by the laser system. The following description is illustrated in figure 2.21. White light is generated in a sapphire plate and focused onto a nonlinear (birefringent) crystal (here BBO) and overlayed with the first 800 nm pump. A part of the white light has near infrared components that are used as seed for the signal beam. The second order DFG process in the crystal yields a weakened pump, a signal and an idler pulse ($\lambda_{signal} < \lambda_{idler}$). By changing the angle between the ingoing beam and the crystal surface, the phase matching condition can be changed, making the outgoing signal and idler wavelengths tunable.

In a second step, the gained signal beam passes the BBO crystal again, thereby being enhanced by a second 800 nm pump beam. The generated idler beam was blocked before. At the end of both steps a signal beam and idler beam are generated. If necessary, both can generate mid infrared light via DFG for example in a Ag_2GaS crystal.

For energy and momentum conservation the following equations must be fullfilled (for the DFG process):

$$\omega_{pump} = \omega_{signal} + \omega_{idler} \Leftrightarrow \frac{1}{\lambda_{pump}} = \frac{1}{\lambda_{signal}} + \frac{1}{\lambda_{idler}} \qquad (2.15)$$
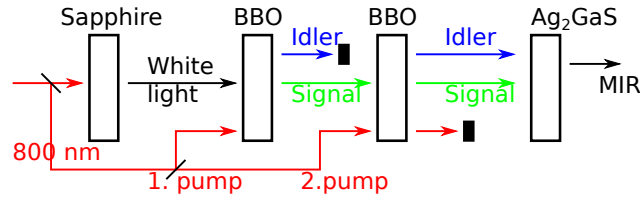
FIGURE 2.21: Sketch of the OPA. White light generated in a sapphire plate and a 800 nm pump beam are generating the signal and idler beams. The signal is passing a second time through the BBO crystal and gets boosted by a second 800 nm pump beam. Both signal and idler can generate radiation in the MIR by DFG. For a better overview the BBO is drawn two times although it is the same getting passed from reciprocal directions.

$$\vec{k}_{pump} = \vec{k}_{signal} + \vec{k}_{idler}. \tag{2.16}$$

Equation 2.16 describes the phase matching in the nonlinear crystal.

Figure 2.22 shows a sketch of the used OPA, which was built by Amul Shinde and Katrin Admczyk (for the experiments with IR light as a pump beam). It is located on the opposite side of the optical table and the outgoing radiation can be guided towards the THz setup. When the two mirrors, which are hit separately by the signal and idler are properly adjusted, they should not be touched anymore (provided the OPA is running correctly). The DFG crystal is positioned on the THz board in a telescope, so that the spot size of the signal and the idler are ideal for MIR generation. If a small spot size at the sample focus of the IR is desired or needed, a f=100 mm lens can be positioned before the third parabolic mirror (e.g. FWHM focus size of around 0.7 mm). For bigger spot sizes like 1.4 mm FWHM the last mirror before the hole of the third parabolic mirror can be exchanged to a concave gold mirror (e.g. f=500 mm).

2.11   Pump-probe extension with tripler box

In order to obtain pulses at wavelengths of 400 or 266 nm, the THz setup can be expanded by a second or third harmonic generator, which position is shown in figure 2.23. This leads to pump wavelengths of 800 nm when the box is empty, and 400 and 266 nm when a BBO or BBO plus retardation plate, half waveplate and a second BBO, respectively, are installed. Accordingly to the beams, the detection parts have to be modulated if they are used as a probe. They need to pass the hole in the fourth parabolic mirror with a detection unit afterwards.

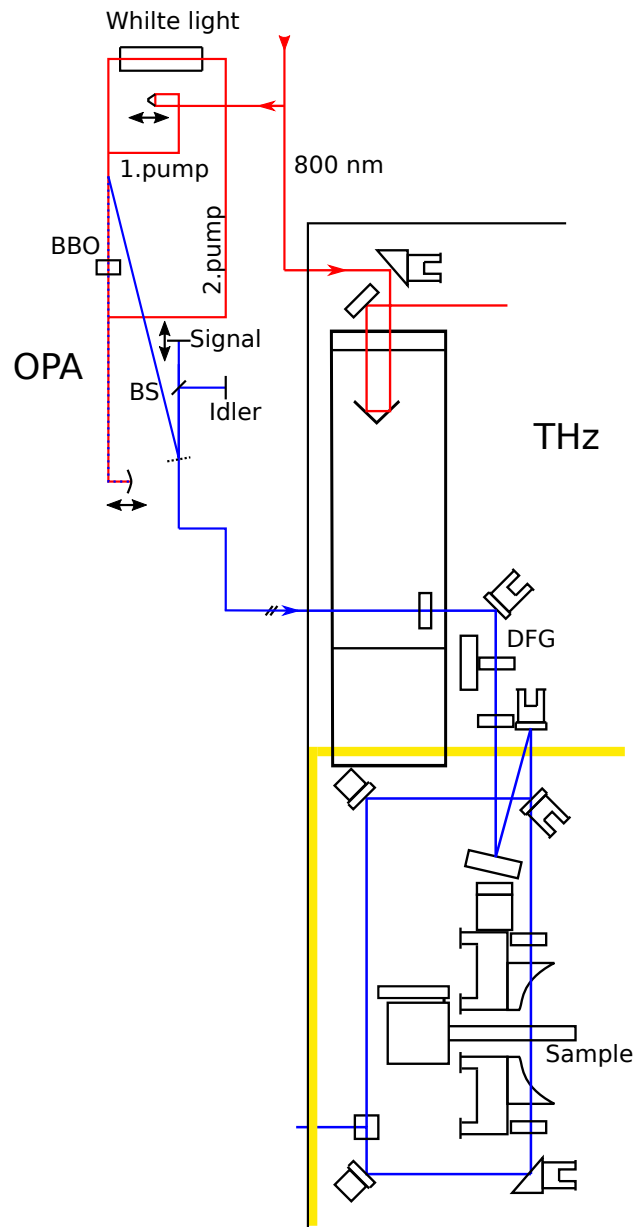FIGURE 2.22: Sketch of the OPA, which radiation is guided over to the THz Setup. Red represents the 800 nm beam and blue IR radiation (NIR+MIR). The dimension of the OPA part is not to scale.
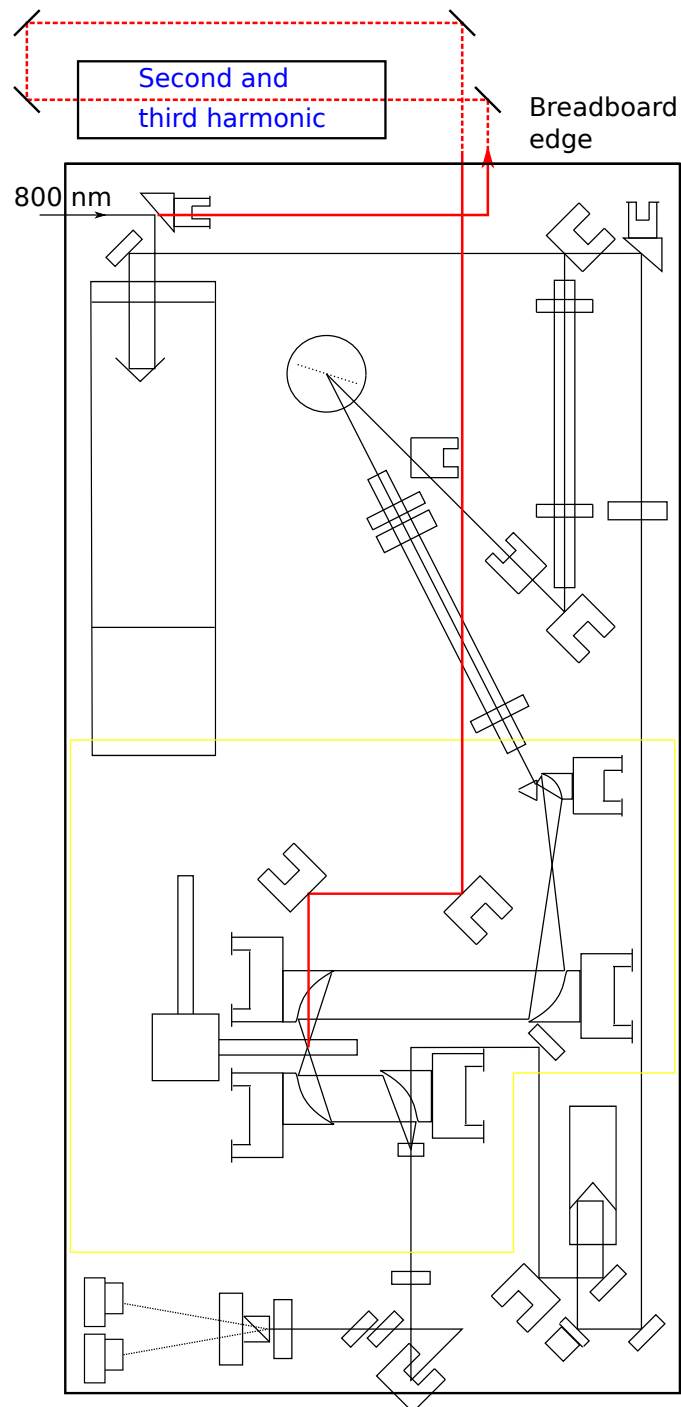
FIGURE 2.23: Sketch of the THz setup with the tripler box. In red the beam path of the possible 800 nm, 400 nm and 266 nm beam is depicted. All can be used as a pump and if changes are done in the detection part, also as probe.

2.12 Summary

A versatile pump-probe setup was built as described in the previous sections. It has a LN crystal as the THz radiation source, pumped by a 800 nm beam, with a tilted pulse front. The second pulse can be the fundamental wavelength coming from the laser system or higher harmonics from it, e.g. 400 nm or 266 nm. Additionally, IR light from an OPA can be used, which is tunable from 1.6 to 10 μm.

The generated THz has a bandwidth ranging from 0.2 to $\backsim$1.5 THz, with a central frequency of 350 GHz. Since the LN crystal is not cooled, the emission above 1 THz decreases strongly. At the sample position energies of 0.2 μJ can be obtained (fluence 10^{-5}J/cm^2). An efficiency of 3*10^{-4} can be achieved. In comparison, the conversion efficiency for THz generation is typically less then 10^{-4}. The THz beam path was checked at various positions to ensure a centric beam guidance.

At the end the THz pulse is recorded by EOS, that enables the collection of the electric field. As a result, the amplitude and phase can be gained for further analysis or calculation.

2.13 Outlook

In order to improve the THz setup, two major changes will be realized in the future. One is incorporating the LN crystal in a cryostat which should increase the THz pulse power by a factor of at least 10 and expand the bandwidth above 2 THz with a central frequency around 1 THz. The other would be to use a balanced photodetector (designed by the Ultrafast Electronics Scientific Support Unit of the MPI-MPSD) which would give a better signal to noise ratio. Another part would be the installtion of a cryostat at the sample position, for cooling samples.

Chapter 3

Carbon based materials

3.1   Motivation for studying graphite oxide (GO) films

A vast field of research today deals with carbon based materials. This leads to various new insights and products in many sectors, like electronic devices [52], filters [53] or in medical applications [54].

One open question until now is, which route is suitable for a mass production of graphene (a carbon monolayer, described in more detail in 3.2), which is a potential future key product. One of the several manufacturing options, is via chemical processes in solutions. The first step is the oxidation of graphite to graphite oxide (GO[1]). The next step is to mechanically separate the GO-creating sheets. This solution can be dried on a substrate and the oxidized graphene flakes are superposing each other, building a layered system. Graphene is formed from the solution by reduction methods. In figure 3.1 the steps are depicted, except for the reduction step.

In this work, a GO membrane system was studied. The original motivation for pump-probe experiments was to study the water content and vibrational behaviour between the sheets via IR-two-color-spectroscopy. But the overall strong electronic response superimposing with for instance the C=C vibrational mode at 1575 cm^{-1}, made it clear that an analysis of the carrier behaviour is necessary to complement those experiments.

THz radiation is sensitive to these free carriers and can complete previous investigations to better describe the membrane. Hence, experiments on the vibrational states of GO were performed by Amul Shinde, by means of IR spectroscopy and the continuative pump-THZ-probe spectroscopy which is described in this chapter. It is possible to investigate the electronic behaviour by means of the IR pump-probe setup. However, spatial inhomogeneity of the GO bandgap due to the layered character of the sample makes THz probing useful since its low energy photons. A THz photon should not be able to excite a trapped carrier again into the conduction band.

---

[1]In this work the abbreviation GO is going to be used for materials which consists of a mixture of graphene oxide and graphite oxide sheets and flakes.

After the introduction to graphene and graphite the recorded data and results are shown and discussed.

(A)
Graphite

(B)
Graphite
oxide

(C)
Graphene
oxide
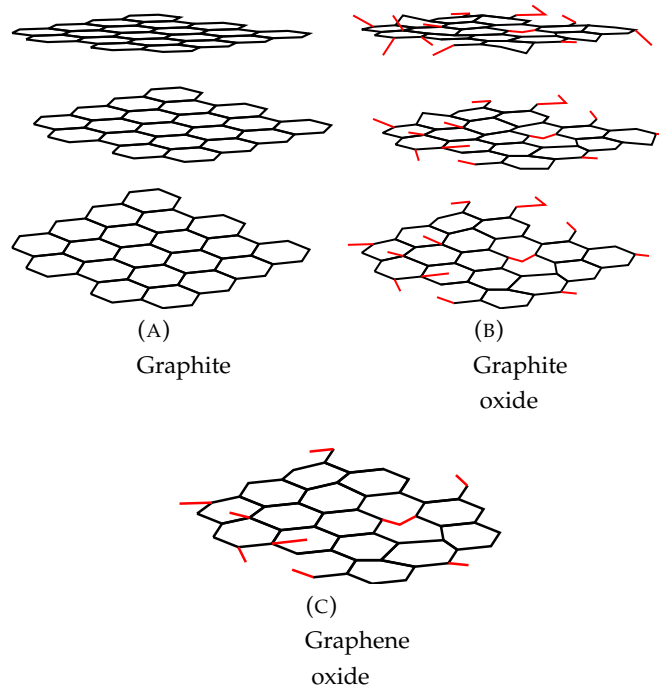
FIGURE 3.1: Graphite (A) becomes graphite oxide (B) after oxidation and exfoliation leads to graphene oxide (C). Oxygen groups like phenol or carboxyl are depicted in red. Adapted from [55].

3.2   Introduction to graphite and graphene

(A)   (B)
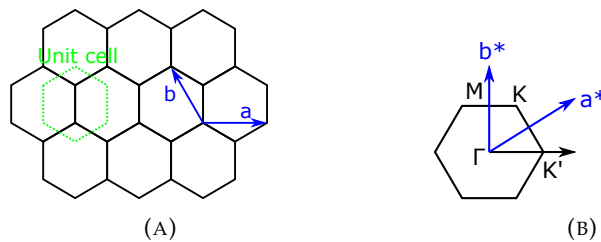
FIGURE 3.2: In (A) the honeycomb structure of graphene with the respective unit cell is shown. a and b are the basis vectors and the nearest neighbours have a distance of 0.14 nm. The first Brillouin-zone is shown in (B) with the Dirac points K and K′ and the reciprocal basis vectors a* and b*.

Graphene consists of carbon atoms which are arranged in a planar honeycomb pattern (see figure 3.2). It was first isolated in 2004 [56]. Between the next neighbour

atoms σ bonds are holding the structure together and the electron in the p_z orbital is building π bands with its neighbours. This creates an electron gas delocalized over the planar surface. For displaying the band structure, a transition to the reciprocal structure needs to be made. In this case, it is also a honeycomb structure, as can be seen for the first Brillouin-Zone (BZ), shown in figure 3.2(B). Only two corners are named because there are only two sub-lattices. The edges are typically named K and K'. At these special points the valence band (VB) and the conduction band (CB) are overlapping. The peculiar thing is, that the band structure is straight around these points (see figure 3.3(A)), which allows descritption of charge carriers with the Dirac equations. They have a vanishing effective mass and spin 1/2. That is why the points K and K' are sometimes called Dirac points [57].

In the case that there are one or two carbon layers, the structure can be described as having no bandgap between the VB and CB. By piling up more layers the band structure is changed. For 10 or more layers the object behaves like thin graphite films [58]. The band structure of graphite is shown in figure 3.4 [59]. In contrast to graphene the band structure of the π bands are quadratic around the K point. Independent of the number of layers, defects lead to a band gap and so one has a semiconductor or semimetal like behaviour.

Several methods can be used for producing graphene, like chemical vapour deposition (CVD) [60] or exfoliation techniques. A pre-stage on the way to graphene was studied here, described as the "filtration of a monolayer graphene oxide dispersion"[2] (and purchased from GRAPHENEA S.A., with the following characteristics: oxygen level: 41-50%, thickness: 12-15 μm and non-conductive).

---

[2]https://www.graphenea.com/collections/graphene-oxide/products/graphene-oxide-filter
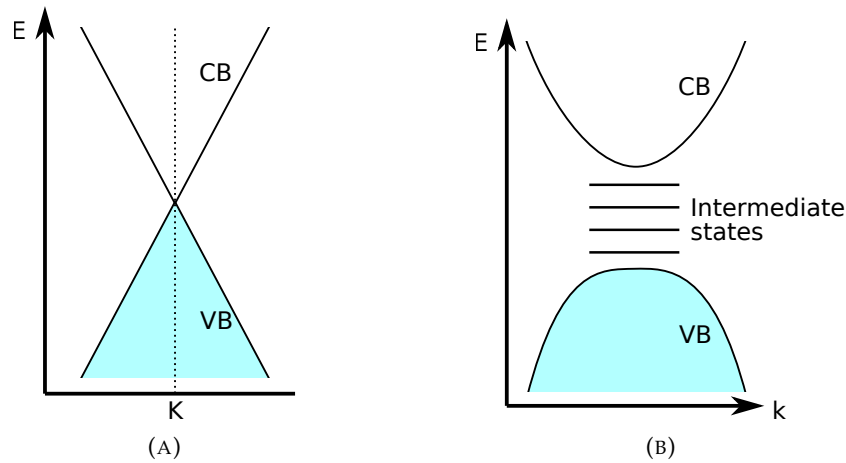
FIGURE 3.3: The band structure with no band gap of perfect graphene around the K (Dirac) point is shown in (A). The energy band structure of a semiconductor with many defects is illustrated in (B). The light blue colour marks the filled valence band before any interaction.
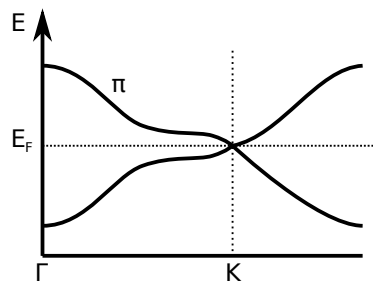
FIGURE 3.4: The band structure of graphite around the K point is not linear like in graphene but quadratic.

3.2.1 GO - Graphene/Graphite oxide

Befor being able to use graphene in a wide variety of fields with its desired properties, it must first be produced on a large scale. The Scotch tape method or CVD [61] is presently not the method of choice. There is a more promising approach via GO solution, since it can be produced in big quantities at once. It should be noticed that e.g. the CVD method gives much better results in terms of structure homogeneity and therefore, conductance (if that is the desired characteristic).

The basic steps of GO production are described in the following: it starts with the oxidation of graphite. Between the sheets, for instance oxygen (epoxide), hydroxyl and carboxyl groups are formed [62, 63, 64]. This is due to the usage of e.g the oxidant $KMnO_4$ (potassium permanganate) [65] during the process. The oxidation process leads to wider spacing of the layers, with respect to graphite (the spacing

changes from 3-4 Å[66] to 7-14 Å[67, 68]). This condensed matter is hydrophilic and water from the solvent or air humidity can intercalate. By a fast increase of temperature, the layers can be separated and single or multilayer flakes of GO are obtained. Another splitting method is to press the oxidized solution through a nozzle, which separates layers through shear forces [69] or to use a sonicator. This material can now be dried on e.g. a filter, like the samples that are studied here. Such a layered material is very heterogeneous and each slide should have a different band structure. It would range from graphene to a semiconductor with many defects, having intermediate states in the band gap, as depicted in 3.3(B).

For the conversion to pure graphene, an additional step is necessary, for reduction of the sheets (for example alanine, a reducing agent [70]). At the end of the process reduced graphene oxide (rGO) is obtained but has by far not the quality of graphene produced with the CVD method mentioned above. Increasing the temperature to seperate sheets can also lead to rGO (or rather thermally reduced graphene oxide [69]). One of the most used methods at the moment for gaining GO is the so-called Hummers method [71].

3.3 Recapitulation of selected publications

Before showing the GO measurements in the next sections, a short selection of publications should be listed, that studied carbon materials.

One reason why there is such an interest in graphene at this moment in time is its high conductivity value. To measure this, one possibility is to use the four-point probe method [72]. In the work of Tölle et al. [69], that technique was used to measure thermally reduced graphite oxide (TRGO) on plastic substrates. The conductivity for their samples ranged from 0.5 to 16 S/cm. Unfortunately, the probe tips of the four-point probe device have to be in contact with the conductive layer. It can lead to fractures in the film, especially when it is very thin or got a special surface which should not be touched. One method to overcome this is to use THz-TDS (time domain spectroscopy). The THz radiation can non-invasively probe the conductivity. Two geometry possibilities can be used for that. Either the measurements are done in transmission or in reflection mode [73]. If the experiment is performed in reflection mode, all kinds of substrates can be used for graphene. However, it is more challenging to use that geometry. Investigating these THz-TDS methods are of great importance, since it is desired to produce graphene on a large scale and to continuously check its characteristics, like the conductivity. This was studied by Mackenzie et al. [74] (March 2018). As mentioned above, both transmission and reflection methods can be used and result in the same values for the conductivity of graphene. For single-layer graphene the conductivity was measured to be around

1.7 mS in transmission mode and 2 mS in the reflection geometry. The difference arises from measurement uncertainties. What should be noted, is that the conductivity changes up to 20% when the relative humidity is changed from 0% up to 60%. Therefore the humidity should be kept stable during all the measurements, which was done also here by purging the setup with dry air.

Below, pump-probe experiments of some publications should be shortly discussed. The interpretation of the data will not be disputed, since there is an ongoing debate in the literature and is discussed in section 3.11.

In 2008, one of the earliest publication studying epitaxial grown graphene via pump-THz-probe spectroscopy was published. George et al. [75] did study 12 to 20 layer thick graphene samples (one should rather talk about thin graphite). They recorded that the decay after optical excitation is a three step process. The model to explain the data is deviated from the formulation describing transmission through a conductive material as introduced by Tinkham [76]. Additionally, the intraband conductivity was derived. The pump pulse energy was varied between 1-15 nJ (pump spot size of 350 μm) and it shows a dependency of the recombination process with the carrier density. The process for the recombination could be via plasmon emission, phonon emission and Auger scattering. Besides, the 20 layer sample has a recombination rate that is two times faster than the thinner sample with 12 layers of graphene.

One year earlier, in the same group, optical pump-probe spectroscopy was also done on epitaxial grown graphene by Dawlaty et al. [77]. The data recorded there can be described by two time scales. For the first time constant, carrier-phonon scattering could be one interpretation of the process. That supports the interpretation of the data shown in sections below. The second time constant depends on the disorder of the sample, which was checked by Raman scattering measurements. Modelling of the data was also done via the formulation introduced by Tinkham [76].

One publication in 2011 from Kaniyankandy et al. [78] reported optical pump-probe spectroscopy experiments on graphene oxide (pump wavelength 400 nm). They studied graphene oxide in solution (water) since substrates like SiC can alter the bandgap of the carbon layers on top of it. The decay curves can be described by a multiexponential model with three time constants. In the case of reduced graphene oxide a fourth constant is introduced. The longest time scale is on the order of >400 ps (as in the measurements shown in the sections below) and is attributed to deep trap states (the trapped carriers need a lot of time to recombine). By comparison of the decays of graphene oxide and reduced graphene oxide, the time constant do strongly change. It leads to the conclusion that the oxygen groups are playing a major role for the carrier-phonon scattering and recombination process. Therefore, the reduction process changes the trap states number. In addition, the absorption increases in the blue frequency region. Moreover, different pump intensities were used

and showed that in graphene oxide, the carrier dynamics are independent from the carrier density.

The publication of Kar et al. [79] (2014) shows measurements on multilayer reduced graphene oxide. They first show the conductivity of their samples measured in a THz-TDS. The values they got ranges from 500 to 600 S/m, depending on the sample. For the modelling they used the Drude-Smith model, since the Drude model did not work for the data. Also, optical-pump-THz-probe spectroscopy was performed by Kar et al. and the decay curve was analysed with a model incorporating three time constants. Again the relaxation is mediated by carrier-phonon scattering. In addition, at different delay times after excitation the THz time trace was recorded to gain the change in conductivity due to excitation. Unfortunately the Drude-Smith model does not reflect the data before 3 ps, maybe due to the fast rate of relaxation processes happening after excitation.

The work of Mihnev et al. [80] (2016) reports 800 nm pump-THz-probe spectroscopy on different samples, as multilayer epitaxial graphene and CVD graphene. If the samples are highly doped, the recorded decay trace can be described by a mono-exponential model. For theses samples there is no time dependence on the substrate temperature and a weak one on the pump fluence. In contrast, a multilayer layer (63 layers) sample with low doping and at cryogenic temperatures has a bi-exponential behaviour. The approach to explain the data is microscopic and not originating from e.g. the Drude model. Moreover, they state that carrier-acoustic-phonon scattering does not play a role on time scales of tens of ps. Also, disorder does not need to be taken account, which indicates that they have very homogeneous samples.

The different pump-probe experiments show that even if the publications are studying graphene or graphene oxide, the results and used models can strongly differ. Another point is the usage of a model to describe the processes. In that direction, Ishida et al. [81] (2011) did perform time resolved photoemission spectroscopy on graphite. One purpose was to check the usability of the two temperature model (TTM). Right after the excitation from a pump, coupled-optical-phonons can be tracked. The dissipation of the energy is likely to happen through electron-coupled-optical phonon scattering in the first hundreds of fs. Also, the electron-electron scattering cannot be held responsible for the energy loss of the excited electrons. However, it cannot be ruled out, that during the excitation process, both, excited electrons and coupled-optical-phonons are generated. Therefore, for short times (under 200 fs) the TTM might break down. But in this range lies the time resolution of the experiments performed in this thesis. Consequently, no statement can be made about its correctness or not. To already mention some results from our group, the scheme that optical phonons are being generated at early times (around 150 fs) is in agreement with the experiments done by Amul Shinde (see below) and verified here.

3.4   Checking the feasibility to measure GO

The method that is used for studying carrier dynamics, is to constantly probe with the EOS 800 nm beam the maximum of the THz field. It records how it changes over time, in respect to the delay between the pump and probe beam [82].

Before applying this technique, it must be checked if there is a phase shift between the THz pulses passing the pumped and unpumped sample. In the figures 3.5 and 3.6 the THz traces of the chopped and unchopped signals are shown. These are going through the GO sample when it was excited at different fixed delays in relation to the maximum of the overlap. No phase shift at the different times can be seen which means that the effect to be investigated is frequency independent. This allows the measuring of the decay of the THz maximum in relation to the delay between pump and probe pulse.
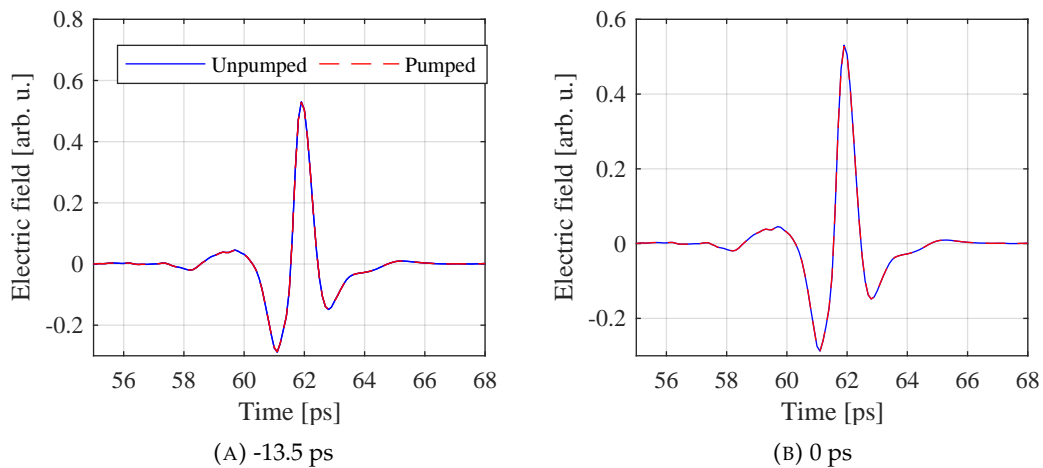
FIGURE 3.5: In the figures (A) and (B), the THz pulses from the unpumped and pumped signals are shown at times -13.5 ps and 0 ps, in relation to the overlap maximum.

(A) +0.2 ps

(B) +4.5 ps
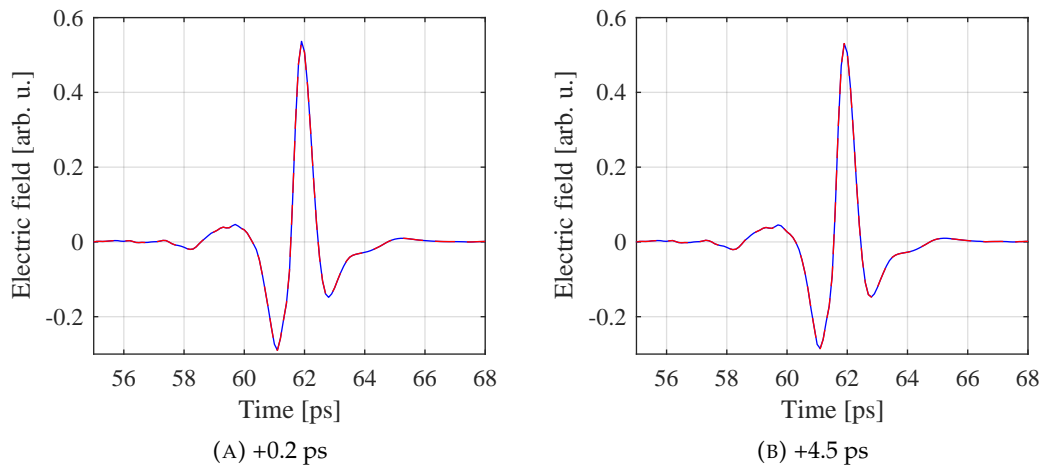
FIGURE 3.6: In the diagrams (A) and (B), the THz pulses from the unpumped and pumped signals are shown at times +0.2 ps and +4.5 ps, in relation to the overlap maximum. Legend as in 3.5(A).

By subtracting the pumped and unpumped THz pulses, a statement about the noise level can be made. The differences can be seen in the figures 3.7 and 3.8. The noise level is on the order of $3*10^{-3}$. Around the peak fields, the differences of the pumped and unpumped THz pulses are at their maximum. To be more precise, that extremum for the difference curve is arising around the inflexion points of the THz pulses. It should be noted, that one main noise contribution comes from the THz pulse itself. This is why, the improvements on the used electronic devices might be at some point unnecessary, if the THz pulse noise is too high.

(A) -13.5 ps

(B) 0 ps

FIGURE 3.7: In the figures (A) and (B), the differences (blue) of the unpumped and pumped THz pulses are shown at times -13.5 ps and 0 ps. Scaled by a factor of $10^{-2.5}$, the unpumped THz pulse is shown in red.
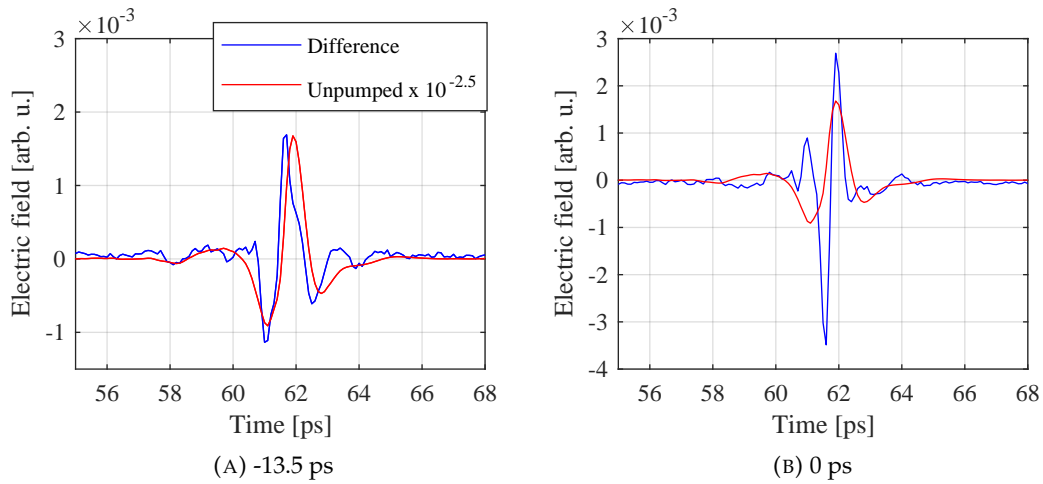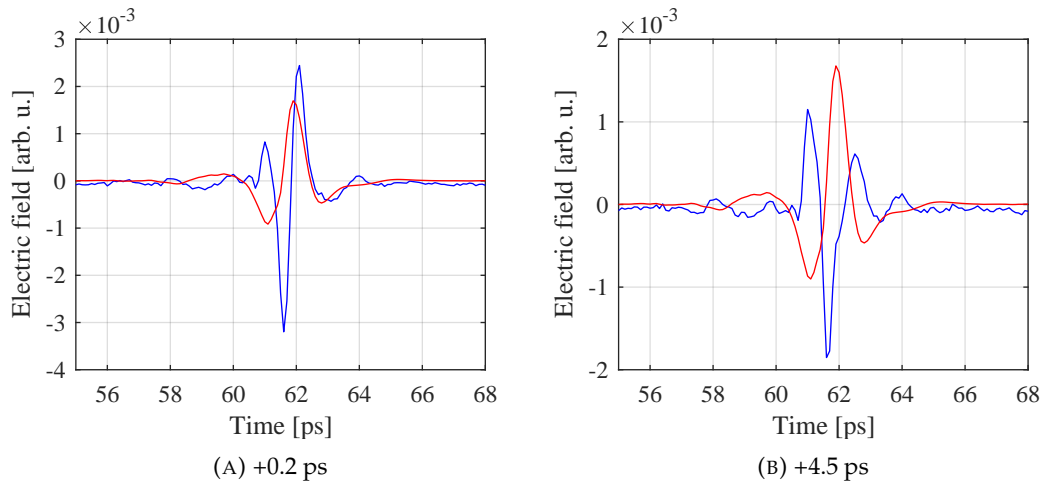

(A) +0.2 ps

(B) +4.5 ps

FIGURE 3.8: In the figures (A) and (B), the differences (blue) of the unpumped and pumped THz pulses are shown at times +0.2 ps and +4.5 ps. Scaled by a factor of $10^{-2.5}$, the unpumped THz pulse is shown in red. Legend as in 3.7(A).

3.5 Absorption of GO in the NIR and IR region

The GO membrane was measured with an UV-Vis[3] and an FTIR[4] spectrometer to record the absorbance and the absorption length, shown in figure 3.9(A) and (B) respectively (partially measured by and with Amul Shinde). Both data sets acquired from the two different commercial setups, did not have the same baseline. Therefore, there was an offset between both data points sets. To align both curves, a constant value was added to the data of the UV-Vis part, since the Bruker device is more reliable in the IR frequency range.

For the pump-probe measurements, three pump wavelengths were used (0.8, 2 and 3 μm). As seen in figure 3.9(A), at 800 nm the absorbance makes a kink, before increasing drastically for smaller wavelengths. At 2 μm the absorbance is at 0.9 OD and it is the lowest value of the three pump wavelengths. A peak of the absorbance is at 3 μm, which arises from the absorption of the water and oxygen groups in the GO membrane.

The absorption length of the $\sim$13 μm thick membrane at 0.8 and 3 μm are quite similar, with a value of around 3.8 and 3.2 μm respectively. For 2 μm the absorption length is at 6.2 μm. Therefore, the pump beam can penetrate deeper at a wavelength of 2 μm and excite more carbon layers out of equilibrium.

To foreclose already some adjustments, the idea was to adjust the pump fluences so that it matches the different penetration possibilities. For 800 nm pump wavelength it was set to 12 μJ/cm^2, for 2 μm to 40 μJ/cm^2 and for 3 μm to 45 μJ/cm^2. The fluence of the 800 nm pump wavelength could have been easily increased, but at higher pump fluences thin GO membranes did get black marks, so were destroyed by that. This limited the pump fluence for 800 nm. Less fluence did result in very noisy data. At 2 μm the idler beam of the OPA was used. By decreasing the power of that pump radiation with IR absorptive filters to 1/4 of the initial power, no signal was detected anymore. At 3 μm pump wavelength the pump spot size was strongly reduced in comparison to the two other pump spots (from 1.4 mm to 0.7 mm), to be able to record a signal, because the output by the DFG process was very low.

This is why the different pump fluences were not tuned and there was no recording of a measurement set with different pump fluences at one wavelength, to check if there is a dependency between the decay process and the carrier density. At least from the publication of Kaniyankandy et al. [78], no dependence of pump fluence and carrier density for graphene oxide was observed. It indicates that it might not happen for the samples used in this work, but needs to be checked in a future experiment.

---

[3]Ultraviolet and visual spectrometer, Shimadzu 3600
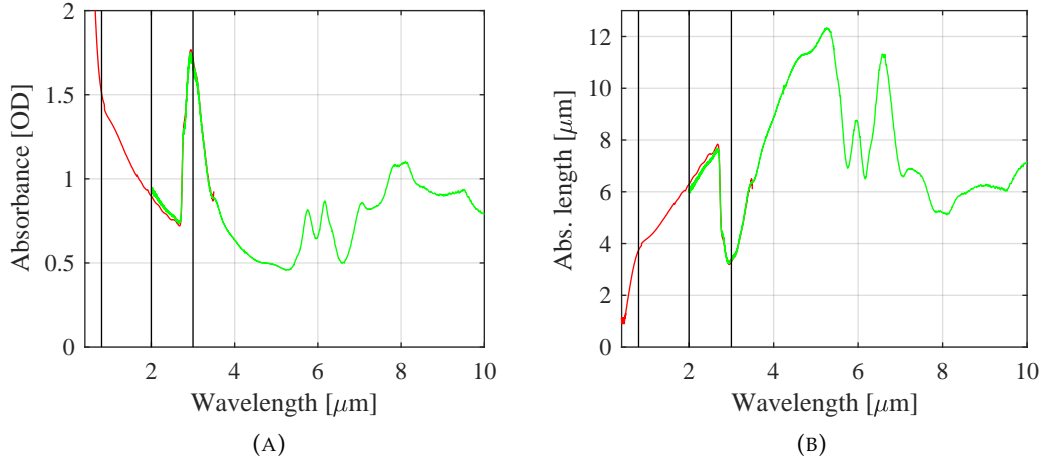[4]Fourier transform infrared spectrometer from Bruker, Vertex 70

FIGURE 3.9: The absorbance of the GO membrane is shown in (A) and the absorption length in (B). Red depicts the measurement done in the UV-Vis spectrometer and green the measurement in the IR spectrometer. The black lines depict the wavelength of 0.8, 2 and 3 μm, which were used as pump wavelengths in the pump-probe experiments.

3.6 Recorded data

The software of the data aquisition unit from the THz setup is recording different values. These are the vertical and horizontal polarisation of the electric field in the unpumped $E_{unpumped}$ and pumped E_{pumped} mode and the difference between them.

In the literature two ways are used for presenting pump-probe data. One is by plotting the change of the electric field $\Delta E = E_{pumped} - E_{unpumped}$ used here (THz peak amplitude [83]), the other by showing the change in transmission [77]. The following equation 3.1 shows how to calculate the transmission change $\Delta T/T$ from the recorded electric fields:

$$\frac{\Delta T}{T} = \frac{I_{pumped}}{I_{unpumped}} - 1 = \frac{|E_{pumped}|^2}{|E_{unpumped}|^2} - 1 \tag{3.1}$$

3.7 Pump-probe spectroscopy of GO

In the following literature references [77, 75, 79, 84, 80], similar experiments on graphene or GO were performed, but not further discussed since the interpretation is under current debate as mentioned in section 3.11. In our case, different pump wavelengths are used to study the electronic dynamics of GO. The first is 800 nm, that could be considered a reference measurement, since a lot of laser system are emitting at that wavelength, so that it can be easily used as a pump. The second is 2

μm which is generated in an OPA as is the third pump beam with a wavelength of 3 μm.

Different possibilities exist to analyse the recorded data. One way is to evaluate the EOS scans at different delay times after the overlap of the two pulses and look at their spectra or the calculated conductivity (or the refractive index). With the Drude model or variations of it, it could be possible to obtain information about its change over time. But as stated in chapter 2 the bandwidth of the THz pulse goes only up to 1.5 THz. Hence, no features could be seen or reasonable fits made. More importantly, the Drude model would only be a classical approach to describe a heterogeneous system that is excited out of equilibrium by the pump pulse. So in the following section first the raw data will be discussed. Later on it is shown how the data can be analyzed.

3.8 Raw data

The raw data plots show ΔE over the time delay between the pump and probe pulse. The fact that ΔE is negative, means that the sample is absorbing the THz radiation after excitation of the pump. In appendix D.1 the normalized curves can be seen, as a reference for later measurements.
At the pump wavelength of 400 nm, the GO sample was also pumped but no signal was seen. Since with a ZnSe waver a signal (step function like) could be recorded, a delay stage position error can be excluded. Also, a thin sample turned dark after exposition to the pump beam, which means that the pump energy was high enough to induce a change (at least electronically) to a GO membrane. It is possible that the beam did not enter the sample deep enough (see figure 3.9(B)) to enable the THz to detect a change.

- In the figures 3.10 the GO sample was pumped at 800 nm and probed by THz radiation. Since this wavelength is widely used in laser systems, it can also be seen as the reference measurement. As it is the fundamental wavelength, it would be possible to pump the film quite strongly, but at around 28 μJ/cm^2, a thin slightly transparent sample turned dark. So a change in the structure is induced. Here, 12 μJ/cm^2 (1 μJ pulse energy) was applied to exclude any damage on the sample. Besides, no damage on thin samples could be seen after exposure. By inspecting the decay curve, it monotonically decreases on several time scales.

(A)

(B)

FIGURE 3.10: Figure (A) shows the decay curve for GO pumped at 800 nm and probed with THz. In (B) a zoom around the maximum is done.

- The smooth curve at 2 μm pump wavelength can be seen in figure 3.11. At time delays of -700 fs and +700 fs bumps on top of the curve can be clearly seen. The pump pulse fluence was 40 $\mu J/cm^2$ (its energy 4 μJ). The smooth decay curve can be explained by the absorption length (see figure 3.9(B)), which is more than half of the sample's thickness. Therefore, most of the layers of the GO membrane are excited and consequently can be probed by the THz radiation.

(A)

(B)

FIGURE 3.11: (A) shows the decay curve for GO pumped at 2 μm and probed with THz. In (B) a zoom around the maximum is done and at -700 fs and +700 fs, embossments can be seen.

- The curve for the overlap, at 3 μm pump wavelength is shown in figures 3.12.

It is the mean of 3 measurement days since the data is noisy. Also the beam spot size was reduced from 1.4 mm (for the other measurements) to ~0.72 mm, for getting a higher fluence that was around 45 $\mu J/cm^2$ on average. In appendix D.2, each curve can be seen. It is suspected that the strong noise arises from the pump spot size being approximately the same size as the probe spot size. Similar to the previous 2 μm pump data, at a negative delay of -900 fs a bump can be discerned. In comparison to the two other pump wavelengths (see figure 3.13), it decays faster. Since the pump wavelength is 3 μm, one difference to the other pump wavelengths is the possible excitation of the OH-stretching vibration mode. This could alter the decay mechanism.
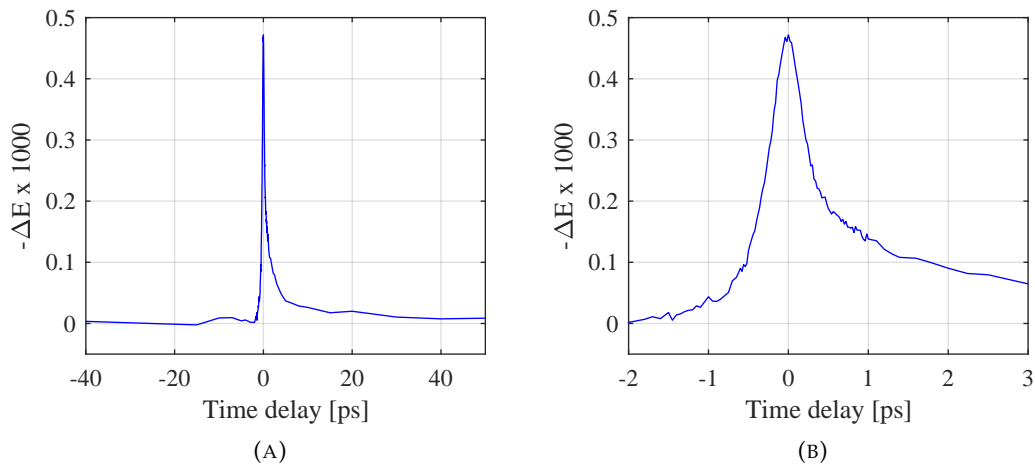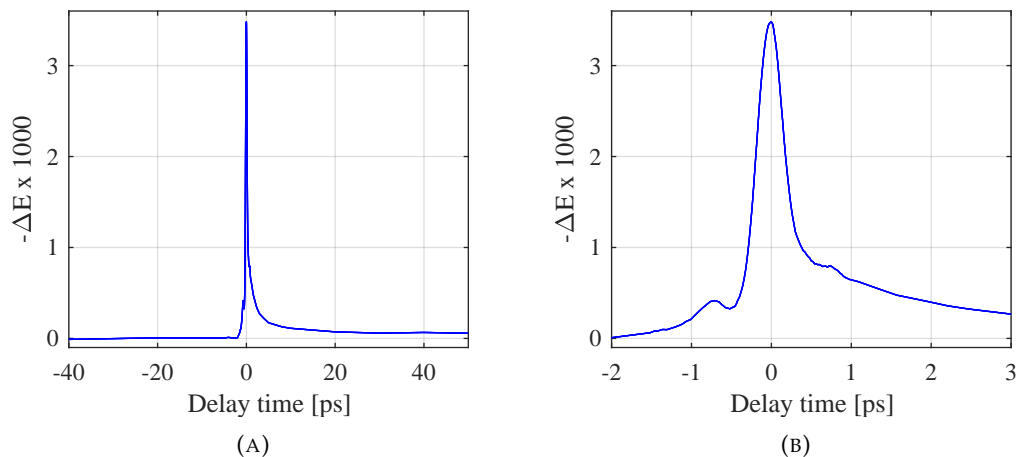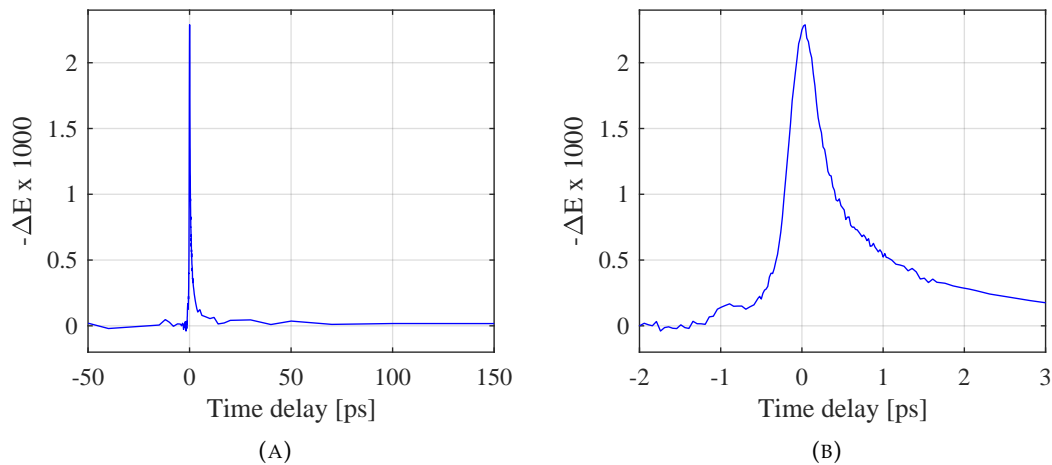

FIGURE 3.12: (A) shows the decay curve for GO pumped at 3 μm and probed with THz. In (B) a zoom around the maximum is done and at -900 fs a bump can be seen.

By comparing the three data sets above, minor peaks before and after the main maximum seem more pronounced if pumped in the IR.
In figure 3.13 a semilog plot of all decay curves is shown. There the data is normed on its maximum value and it could be assumed, that the decaying data, after 1.5 ps, can be described by two exponential functions, which will be done exemplary in the next section.
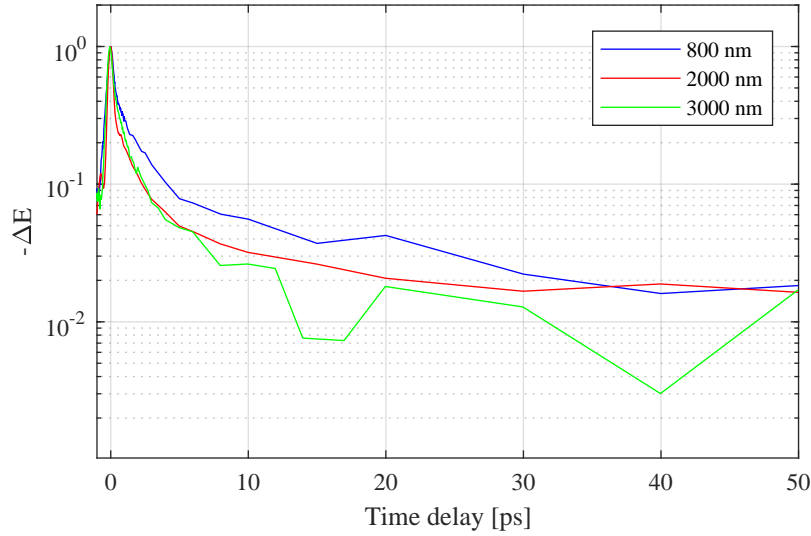
FIGURE 3.13: Overlayed data of the peak electric field change for the three pump wavelengths.

3.9   Stretched exponentials

In this section a simple way to analyse the data with a stretched exponential is introduced. In the literature it was first used to describe the relaxation of carriers in glassy systems [85, 86]. Its general form is the following

$$f(t) = a \cdot \exp(-(\frac{t}{\tau})^\beta) \tag{3.2}$$

with *a* being the amplitude, t the variable, τ a lifetime and β the stretching value.

This way, it can be taken into account, that there is not one single fixed lifetime as for an excited state in an atom but there is a distribution of lifetimes (or decay rates) [87].

In the last decades, that approach was used in different scientific fields, but here it should be looked at how it can be used for heterogeneous systems [88] like GO. A mathematical description of the stretching distribution and its moments can be found in the work of Johnston [89] or [90].

As an example, the fitted data with a pump wavelength of 800 nm are shown in figures 3.14. The blue dots depict the data which are used for the fit, starting 1.5 ps after the maximum of the decay curve, which is set as time zero. In green, the excluded data points are shown. The red fit curve is also drawn at times before 1.5

ps. For both plots the following equation was used:

$$f(t) = a1 \cdot \exp(-(\frac{t}{\tau 1})) + a2 \cdot \exp(-(\frac{t}{\tau 2})^\beta) + c \qquad (3.3)$$

with a different β.

The trapping can be associated to the material's dimension d with the following equation

$$\beta = \frac{d}{d+2} \qquad (3.4)$$

that was introduced by Philips [88]. Here β was set to 0.5, displayed in the fit of figure 3.14(A). This corresponds to a decay on a surface in which the carriers can move. These are the single GO sheets, so a 2 dimensional material.
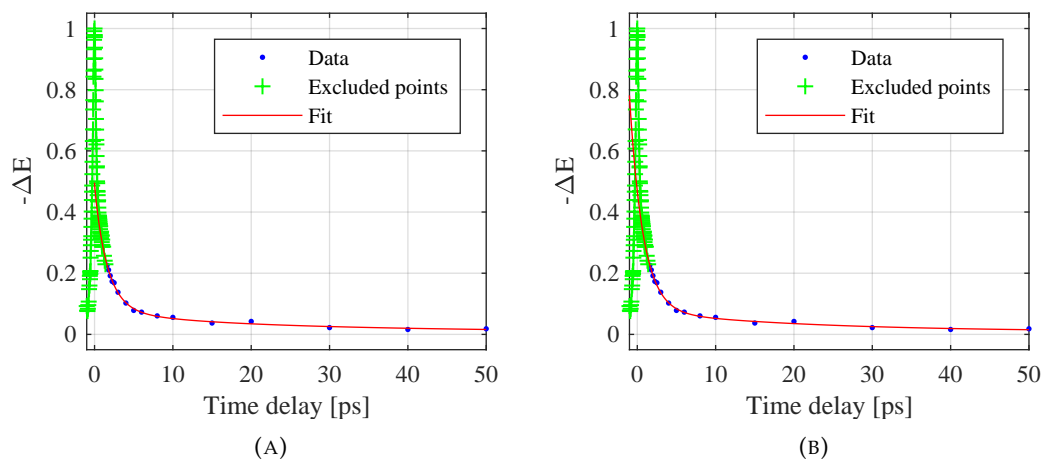
FIGURE 3.14: Both plots show the decay curve when the sample is pumped at 800 nm. In (A) the data is fitted with β=0.5 and in (B) with β=1.

In (B), β is set to 1, expressing a biexponential decay. The values of the fit variables can be seen in table 3.1. $\tau 1$ is clearly between 1 and 2 ps for both fits and $\tau 2$ higher than 10 ps. The error in $\tau 2$ is also quite big, higher than the value itself, arising from the long decay tail. The first decay time could be associated with electron-phonon scattering and is in the range of the one of metallic systems (discussion with Michael Sentef, MPI-MPSD). Slow trapping process is shown by the second time constant. This process takes tens or hundreds of ps. One could understand the results as having a noncoductive material which by pumping is transferred to a metal and after some ps is going back to its original characteristics.

Both R-square values of the fits are very good (almost 1) which means that the fit is

Func	$a1$	$a2$	c	
Stretched	0.37±0.08	0.13±0.09	$0.4*10^{-3} \pm 55*10^{-3}$	
Bi-Exp	0.39±0.06	0.07±0.02	$8.8*10^{-3} \pm 25*10^{-3}$	
	β(fixed)	$\tau1$ [ps]	$\tau2$ [ps]	R-square
Stretched	0.5	1.64±0.63	11.16±39.10	0.9969
Bi-Exp	1	1.73±0.43	21.5±26.4	0.9971

TABLE 3.1: Values of the fitvariables from the fits in figure 3.14.

good. At least from this point of view. The data points, on which the fits were performed are from a time delay after 1.5 ps. Before that, the pump and probe pulses are interacting and a deconvolution of the data should be performed. This is not done, since for the inverse convolution the noise of the measurement must be known for instance, which is not the case here [91].

But if one remembers the decay curves shown in section 3.8, when the sample is pumped in the IR, there are smaller peaks before and after the main maximum. These can not be modelled with exponentials only. So the model is missing terms or should be expressed otherwise. In the next section 3.10, a new model will be introduced, which is suited for the measurements.

3.10 Nonlinear optics using the density matrix

To interpret pump-probe data, as simply as the absorption spectra of an excited system, is only valid when the pulses are short compared to the dynamics of interest. Since the THz pulses generated by optical rectification have a FWHM of roughly 1.4 ps (see figures 3.5), which is already on the same order of magnitude as the decay dynamics studied here, a more sophisticated model should be used for proper interpretation of the pump-probe traces. In the following a model is described, which is more appropriate to interpret the experimental observations.

Calculations, based on third order time-dependent perturbation theory, as described in [92] were performed by Matthias Ruppert. The system can be well described as a statistical ensemble, which can be expressed using the density matrix ρ. Via the trace of the dipole operator V and ρ, the polarisation P can be calculated which is the relevant observable for the system

$$P^{(n)}(t) = < V\rho^{(n)}(t) >, \tag{3.5}$$

where power of n denotes the n-th perturbed order.

First the Liouville formalism is introduced, which is more convenient for handling

the temporal evolution of the density matrix ρ. It is also referred to as the Liouville equation:

$$\frac{d}{dt}\rho = -\frac{i}{\hbar}[H,\rho] \tag{3.6}$$

For convenience the Liouville (super-) operator is introduced as follows:

$$-\frac{i}{\hbar}[H,\rho] \equiv -\frac{i}{\hbar}\mathcal{L}\rho \tag{3.7}$$

$$\mathcal{L}O := [H,O] \tag{3.8}$$

with the Liouville operator $\mathcal{L}$, H the Hamiltonian of the whole system and O an arbitrary operator from the Hilbert space. In equation 3.6 the temporal evolution of the density matrix is stated. The Hamiltonian can be expressed as H(t)=H$_0$+H'(t), with H$_0$ as the unperturbed part and H'(t) when a time dependent perturbation occurs. Latter one is expressed as $-E(t) * V$, with the electric field E and the dipole operator V (from the Hilbert space). By making use of the interaction picture, the evolution of the density matrix becomes

$$\frac{d}{dt}\rho_I(t) = -\frac{i}{\hbar}[H'_I(t),\rho_I(t)]. \tag{3.9}$$

With relation 3.7 and integration, the density matrix can be expressed as

$$\rho_I(t) = \rho_I(t_0) - \frac{i}{\hbar}\int_{t_0}^{t} d\tau_1 \mathcal{L}_I(\tau_1)\rho_I(\tau_1). \tag{3.10}$$

From there the iteration process is used by using the expression above to plug it into itself resulting in

$$\rho_I(t) = \rho_I(t_0) + \sum_{n=1}^{N} \rho_I^{(n)}(t) \tag{3.11}$$

$$with \quad \rho_I^{(n)}(t) = (-\frac{i}{\hbar})^n \int_{t_0}^{t} d\tau_1 ... \int_{t_0}^{\tau_{n-1}} d\tau_n \mathcal{L}_I(\tau_1)...\mathcal{L}_I(\tau_n)\rho_I(t_0). \tag{3.12}$$

Afterwards the substitution of the single interaction times τ to the time intervals t_i (see figure 3.15) between the field-interactions is made. From equation 3.5 the general expression for the polarization is obtained by calculating the trace with the density matrix, which leads to:

$$\vec{P}(\vec{r_0},t) = <V\rho(t_0)> + \sum_{n=1}^{\infty} \vec{P}^{(n)}(\vec{r_0},t) \tag{3.13}$$

$$with \quad \vec{P}^{(n)}(\vec{r_0}, t) = (\frac{-i}{\hbar})^n \int_0^\infty dt_n ... \int_0^\infty dt_1 E(t - t_n)...E(t - t_n - ... - t_1) \cdot$$

$$\cdot \theta(t_1)\theta(t_2)...\theta(t_n) < VG(t_n)\vartheta G(t_{n-1})\vartheta...G(t_1)\vartheta\rho(-\infty) > \quad (3.14)$$

with ϑ the dipole operator from the Liouville space ($\vartheta := [H, V]$) and $G(t) = e^{\frac{-i\mathcal{L}}{\hbar}t - \Gamma(t)}$. $\Gamma(t)$ is an artificially introduced decay term, that accounts for the decay of populated states over time. However, it does not conserve population.
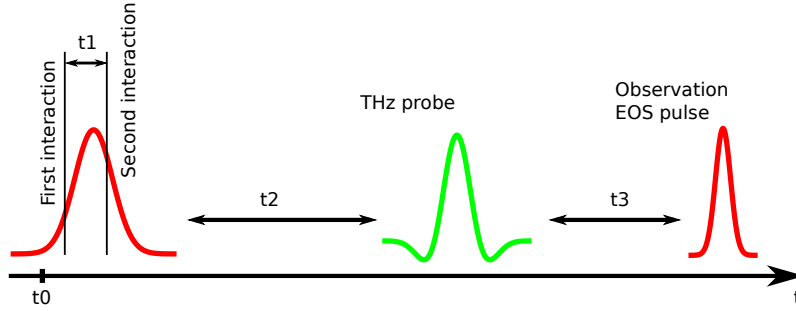

FIGURE 3.15: Interaction of the pulses (not to scale) with the sample. The first red pulse is depicting the pump pulse with its two interactions. After the time t2 the THz pulse is probing the sample. At the end the EOS pulse is probing the maximum of the THz field.

Herein discussed experiments have the main contribution coming from the third order $P^{(3)}$. The interaction pulse scheme can be seen in figure 3.15. Also the rotating wave approximation (RWA)[5] will not be assumed, since the THz pulse is a few cycle pulse (around 1.5 field cycles) and the integral over it cannot be assumed to yield to zero. It is presumed, that the 800 nm pulses are δ-like

$$E_{pump}(t) = \delta(t + \tau)e^{-i\omega_{pu}t} \quad (3.15)$$

where τ denotes the pump-probe delay. The pump pulses precede the probe pulse. Also, it is assumed that the system is in a population state after the interactions with the pump pulse. Given these assumption, the following expression for the third order polarization is derived:

---

[5]RWA: The RWA is an approximation made to a Hamiltonian operator H. This operator can be separated into two terms when a disturbance is occuring: one part for the unperturbed system H_0 and the other H_{Int} for a weak interaction by e.g. an external electric field. The frequency ω_e of that field should be close to a transition frequency ω_t of the system H_0. By expressing the Hamiltonian $H=H_0+H_{Int}$ with the introduced frequencies and in the interaction picture, exponentials with $\omega_t+\omega_s$ and $\omega_t-\omega_s$ are arising. At that point the approximation is made by neglecting the fast oscillating parts $\omega_t+\omega_s$, which tend to zero. It is valid on time scales that are shorter than the lifetime of the excited state [93].

$$P^{(3)}(t) = \frac{-i}{\hbar^3} \int_{-\infty}^{\infty} dt_3 \int_{-\infty}^{\infty} dt_2 \int_{-\infty}^{\infty} dt_1 \theta(t_1)\theta(t_2)\theta(t_3) \cdot$$
$$\cdot E(t - t_3)E(t - t_3{-_2})E(t - t_3 - t_2 - t_1) \cdot R(t_1, t_2, t_3) \qquad (3.16)$$

In figure 3.16(A) a very simplified energy level scheme for a semiconductor is shown. Employing this level scheme, only the Feynman diagrams shown in 3.16(B) and their hermitian conjugate have to be considered for the 3rd order polarisation, once pump and probe don't overlap anymore. The expectation value part of 3.16 can then be calculated as

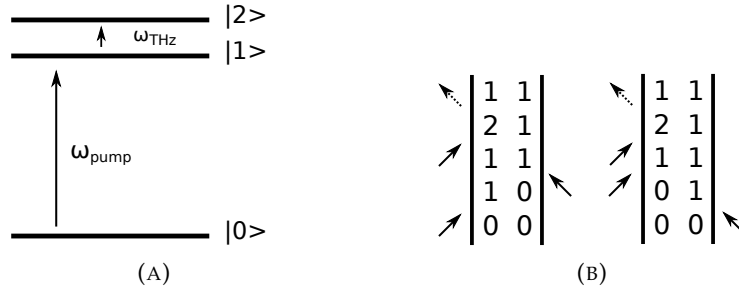(A)   (B)

FIGURE 3.16: In (A), a 3 level system is presented as a starting point for the first primitive description of the system. (B) shows possible Feynman diagrams for that system.

$$R(t_1, t_2, t_3) = |\mu_{10}|^2 |\mu_{21}|^2 \cdot e^{-i\omega_{10}t_1 - \Gamma_{10}t_1} \cdot e^{-\Gamma_{11}t_2} \cdot e^{-i\omega_{21}t_3 - \Gamma_{21}t_3} - h.c. \qquad (3.17)$$

Also assuming being on resonance: $\omega_{10} = \omega_{pu}$ and $\omega_{21} = \omega_{THz} = \omega_{pr}$. Γ_{11}, Γ_{21} and Γ_{10} are the decay rates of the corresponding states. Additionally, the excitation pulses are assumed δ-like.
Evaluating the integrals along t_1 and t_2 leads to

$$P^{(3)}(t) = \frac{-i}{\hbar^3} \int dt_3 \theta(t_3)\theta(t + \tau - t_3) E_{THz}(t - t_3) \cdot$$
$$\cdot |\mu_{10}|^2 |\mu_{21}|^2 (e^{-\Gamma_{22}(t+\tau-t_3)} e^{-i\omega_{21}t_3 - \Gamma_{21}t_3} - h.c.) \qquad (3.18)$$

Each part of the THz pulse is inducing a polarization in the sample, which decays. It can lead to an influence of the THz transient peak which is probed by the EOS beam. In the EOS detection scheme a temporally short 800 nm pulse is used to directly measure the THz field transient. For the data presented here, only the maximum of the THz transient was recorded for the time trace. In this model, it is treated as a δ-like gating pulse at t=0.

Due to the proportionality of the electric field with the polarization $E^{(3)}(t) \sim iP^{(3)}(t)$ and that the detection is done on the THz pulse maximum, equation 3.18 leads to

$$Signal \quad S_{max} \sim \int_{-\infty}^{\infty} dt \delta(t) E^3(t) \tag{3.19}$$

$$\sim \int_{-\infty}^{\infty} dt \delta(t) \frac{1}{\hbar^3} \int_{-\infty}^{\infty} dt_3 \theta(t_3) \theta(t + \tau - t_3) E_{THz}(t - t_3) \cdot$$

$$\cdot e^{-\Gamma_{22}(t+\tau-t_3)} \cos(\omega_{21} t_3) e^{-\Gamma_{21} t_3}$$

$$\sim \int_{-\infty}^{\infty} dt_3 \theta_3 \theta(\tau - t_3) E_{THz}(-t_3) e^{-\Gamma_{22}(\tau-t_3)} \cos(\omega_{21} t_3) e^{-\Gamma_{21} t_3} \tag{3.20}$$

With the last equation 3.20 an expression is found that can describe the recorded data for positive time delays. It consists of the probing frequency $\omega_{pr} = \omega_{21}$, Γ_{22} the dephasing term of the excited population state and the Heaviside θ-functions. The integral can be seen as a convolution of the THz pulse and the response function. By $e^{-\Gamma_{21} t_3}$, the dephasing of the system is accounted for. The model for the carrier decay process is described above in 3.20 by $e^{-\Gamma_{22}(\tau-t_3-t_0)}$.

For the system here, it results to:

$$\Delta E \sim \int_{-\infty}^{\infty} dt_3 E(-t_3) \cos(\omega_{pr} t_3) e^{-\Gamma_{21} t_3} \theta(t_3) \theta(\tau - t_3 - t_0) \left(\sum_{n=1}^{4} A_n e^{-\frac{\tau-t_3-t_0}{\tau_n}} + A_5 \right)$$

$$\tag{3.21}$$

An adapted model, partially motivated from the two temperature model [81] with a sum of exponentials was put into the integration above. The single exponentials have an amplitude A_n and a time constant τ_n, describing the lifetime of a single decay process. A_5 reflects very long time constants, resulting in an offset for the recorded data for long delay times.

The model was minimized to fit the measured data. In the figures 3.17 to 3.22 the decay curves and optimal minimized model curves are shown. Not all the variables could be minimized since the calculation time went quickly over 10 hours. A compromise needed to be made. The time constants gained from the IR pump-probe experiments (conducted by Amul Shinde) are taken as fixed values and the amplitudes, the dephasing rate and time zero t_0 are varied. In table 3.2 the gained values for the parameters are listed. As a first description of the data, the model involves only the most probable interactions in the system. It describes well the shape of the curve. The missing part are the small peaks, recorded at pump wavelengths in the IR. For these peaks, additional mechanism needs to be taken into account and will be calculated as a next step in the future.
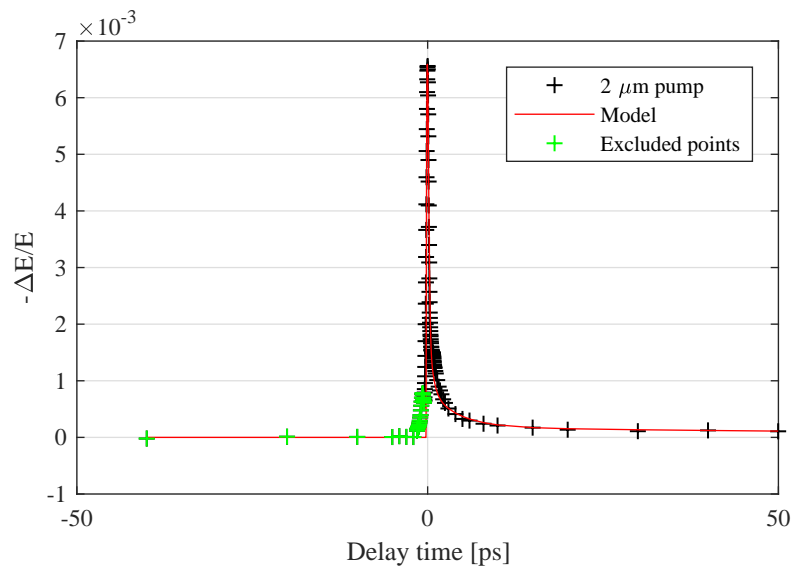
FIGURE 3.17: Decay curve when pumped at 2 μm.
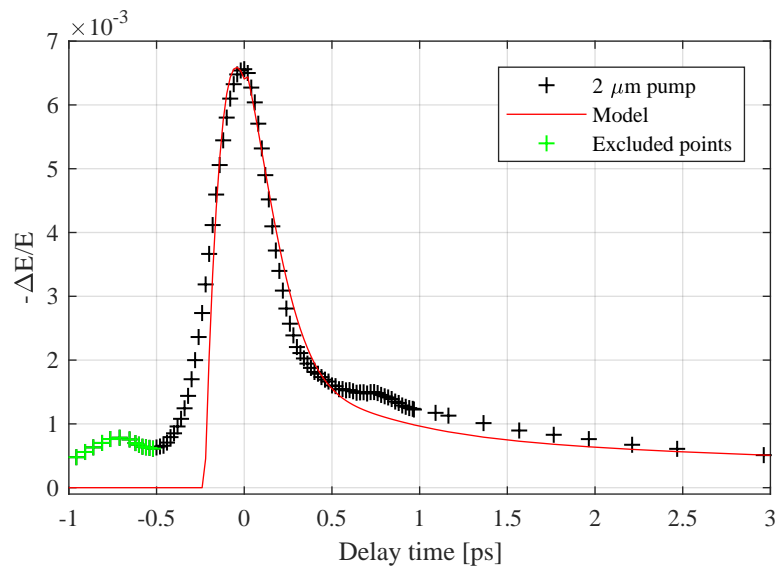
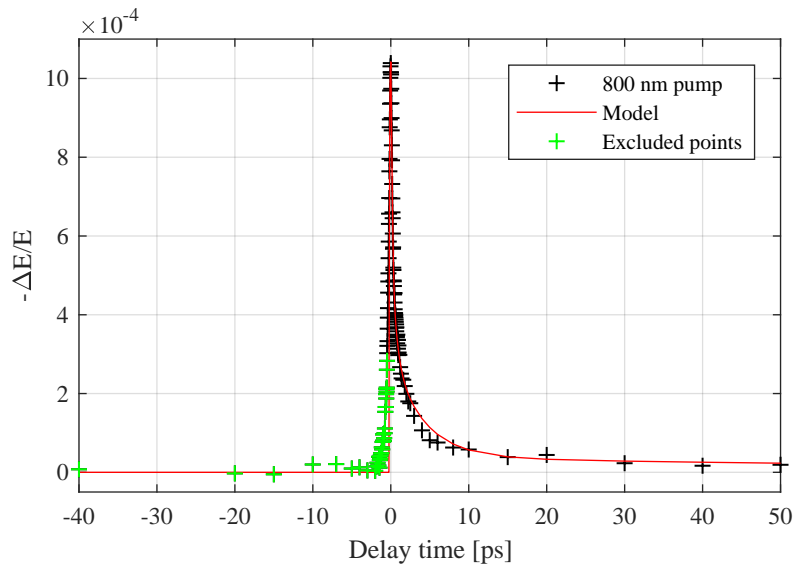FIGURE 3.18: Decay curve when pumped at 2 μm, zoom around the maximum.
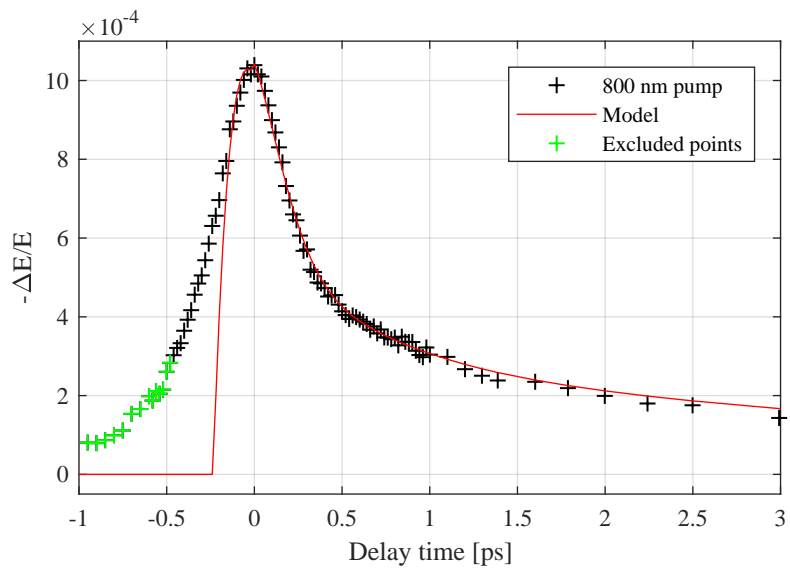
FIGURE 3.19: Decay curve when pumped at 800 nm.

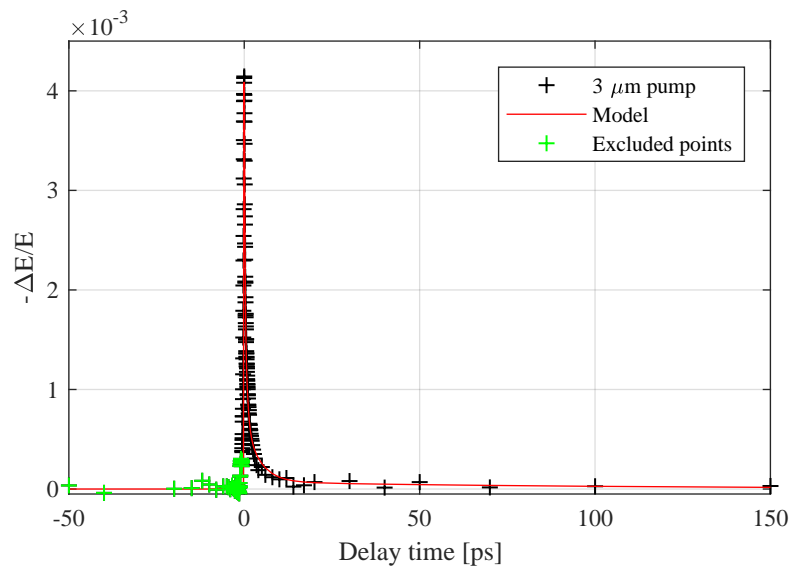FIGURE 3.20: Decay curve when pumped at 800 nm, zoom around
the maximum.

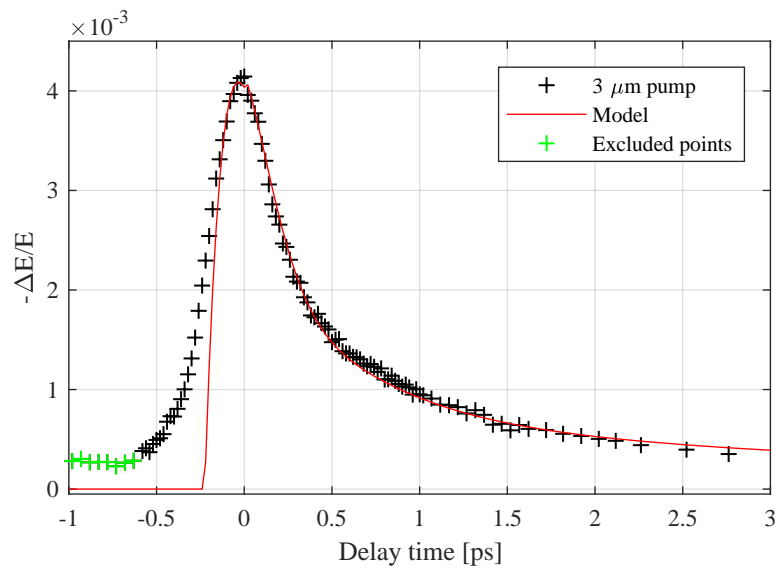FIGURE 3.21: Decay curve when pumped at 3 μm.

FIGURE 3.22: Decay curve when pumped at 3 μm, zoom around the maximum.

TABLE 3.2: Minimazation values for the three different pump wavelengths.

Pump/μm	$A_1 * 10^{-3}$	$A_2 * 10^{-3}$	$A_3 * 10^{-3}$	$A_4 * 10^{-3}$	$A_5 * 10^{-3}$
0.8	21.0	5.0	4.0	0.6	0
2	150.0	14.5	8.0	2.0	0.1
3	63.5	22.5	7.5	0.8	0
Pump/μm	Dephasing Γ_{21} /ps	t_0/ps	R-square	Fluence/μJ/cm^2	
0.8	0.25	-0.24	0.70	12	
2	0.27	-0.23	0.88	40	
3	0.25	-0.23	0.88	~50	

3.11   Discussion

As can be seen in the plots 3.17 to 3.22 above, the model does follow the measured curves. Dephasing of the THz induced polarization happens on the order of 0.25 to 0.27 ps. The model is only valid for positive times. Therefore, only points after the pump induced population should be taken into account. Unfortunately, time zero is not known, and the choice was made to use the data after the first arising small peak, when pumped at one of the pump wavelengths. For the data with a pump wavelength of 800 nm, the data cut was made 0.5 ps before the main peak. As for the 2 and 3 μm data, the cut was made after the first small peak. The rising edge was taken into account this way.

Underneath an interpretation of the carrier decay process in the GO membrane is given:
During the fitting process, the 4 time constants for the population decay were held fixed. The values were taken from the experiments conducted by Amul Shinde with the IR pump-probe setup [94]. The IR radiation is, as the THz radiation, sensitive to carriers but can also probe vibrational modes (e.g. optical phonons). As a result from the evaluation of the data, the time constants were obtained. Since with these the minimization is working well, it is safe to say that the processes are happening on these time scales and are double checked this way. Additionally, the amplitude ratio for the 2 μm data are on the same order. For the other pump wavelengths a comparison of the amplitude ratios could not be done.

The first time constant τ_1 was measured and resulted in 150 fs. It represents the process of carrier-phonon scattering, more precisely carrier-SCOP scattering (strongly coupled optical phonon). The GO system here can be related to the layered composition of graphite. There, the excited carriers are transfering their energy whithin a

couple of hundreds of fs to optical phonons [95]. The energy of the initially excited carriers is transferred amongst others, to the C=C ring stretching vibration (G-mode phonon). In a publication of Kampfrath et al. [96], it was observed that the excitation energy was transferred to optical phonons within 500 fs. This encloses the time value τ_1 here.

The second time constant, τ_2, was set to 600 fs. On that time scale optical phonon - acoustic phonon scattering is occuring. In the literature a time constant of 2.2 ps is stated for graphite for this process [95]. Yan et al. argue that this time constant depends on the number of decay routes. That this occurs faster here, than in the experiment of Yan et al. could be because of a higher variety of decay paths than in graphite, since the GO sample investigated here is strongly heterogenous. The time constant is obtained by the measurement of the time elapsed of the frequency shift of the C=C vibration in the IR pump-probe setup.

The third time constant τ_3 could also be related to processes embedding acoustic and optical phonons. It was set to 4 ps. This time constant might be strongly depend on the trapping states arising from oxygen groups (for instance from carboxyl or epoxide groups). Their importance for the decay mechanism were investigated by Kaniyankandy et al. [78]. They looked at the decay times while using reduced graphene oxide samples with different reduction levels, which leads to a decrease of the time constant from $\sim$9 ps to 2.5 ps (incorporating the time constant τ_3). The interpretation from Kaniyankandy et al. is leaned on the publication of Kampfrath et al. [96] (via phonon scattering). One hypothesis from us is that this third time constant is related to recombination processes via oxygen groups. A possible test might be to use 2,3 and 4 μm as a pump wavelength and compare the data.

The last time constant τ_4 is set to 100 ps. It reflects the long decay tail seen e.g. in the figure 3.17. On that scale, most of the traps are already filled by carriers, so that the remaining ones need more time to find a potential minimum (so traps). Also the GO sample is a sheet system, where each layer is a bit different to the others, which results in a variation for the decay time. Some subsystems can certainly be seen as semiconductors for which the recombination time can be in the nanosecond regime [83]. These long time sensitive processes of recombination could be studied similar to the first passage problems [97, 98], which investigate after how much time e.g. a particle passes a certain position on e.g. a one dimensional chain.

It is suspected, that the elevation at negative times (-700 fs, in figure 3.18) is due to perturbed free induction decay [99]. That effect would explain the slow rising curve in the measured data. This is not included in our model so far but under current investigation.

At this moment in time, there is a debate in the literature for similar systems about

how to interpret the time constants gained by fitting the measured curve. One often finds in the pump-THz-probe community that the first time constant is due to carrier-carrier scattering [77], being faster than 100 fs. Since most of the used amplified laser systems are working with 100 fs pulses it cannot be resolved, but is still interpreted that way. Nowadays laser pulses of a few fs are available but there is no publication indicating that carrier-carrier scattering was measured (to our knowledge). Also Kaniyankandy et al. [78] did power dependent measurements and did not find any decay dependency with the carrier-carrier interactions within their 100 fs time resolution. In the work involving a raman spectrometer [95], no dependency on the carrier-carrier scattering processes was found. Moreover, Yang et al. [100] argue that the carrier-carrier scattering does take place but does not dissipate energy. One argument that the pump-THz-probe experiments were not correctly interpreted, is that the Frank-Condon approximation (shortly described below in 3.11.1) should not be used for graphene or similar systems.

3.11.1 Transition of states

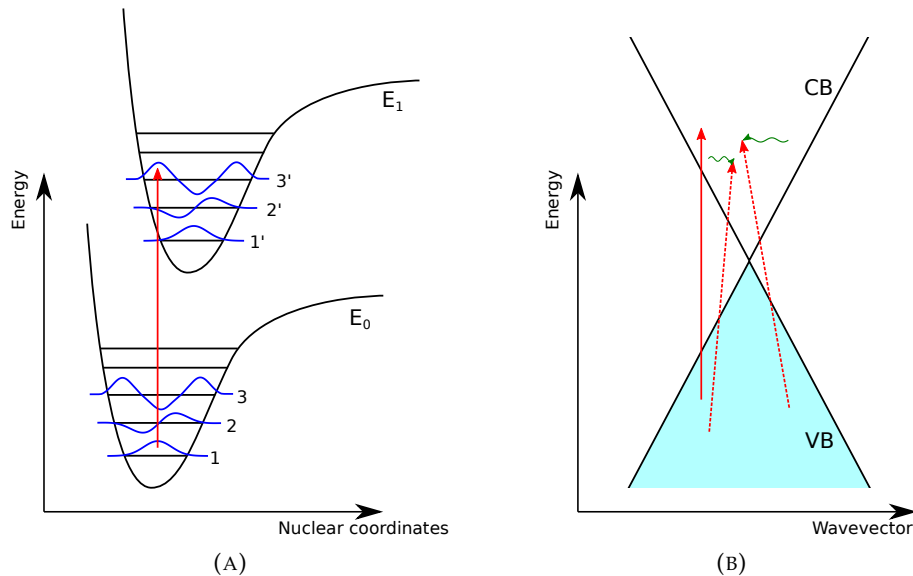FIGURE 3.23: The sketch in (A) shows the direct transition from the electronic state E_0 to the state E_1, after photon absorption. Due to the overlap of the wavefunctions, the vibrational state is changed from 1 to 3'. In (B) the band structure of graphene is shown. The vertical red arrow depicts a direct excitation by e.g. a photon and the dashed red arrows phonon assisted transitions. Phonons are indicated as green arrows.

In this section, a short description of electronic transitions should be given. As first approximation for such processes, the Born-Oppenheimer-Approximation is vastly used [101]. Due to the mass difference of the nuclei and electrons and therefore their difference in inertia, the wavefunction describing a state is separated into two parts. One is for the nuclei and the other is for the electrons. If an electronic transition is studied in a molecule, often the Franck-Condon principle (FCP) is applied. The excitation can be induced by collisions or absorption of a photon. The approximation made in the FCP, is that the dependence of the nuclei coordinates are fixed for the wavefunction describing the electrons at the moment of the excitation.

By absorption of a photon from a molecule, the electron is excited in a higher electronic and vibrational state. Since the process happens on a fast time scale, the nuclei is not changing its position during the e.g. electronic transition, as shown in figure 3.23(A).

The change in the vibrational state is due to the overlap of the wavefunctions of the two different states. It is also referred to as direct (vertical) transition [102]. In addition to the transition with highest overlap, other less probable transitions can occur to other vibrational states, resulting in a distribution of crossings.

In a similar way as for molecules, the FCP can be used for solid state materials like the GO membrane. The direct transitions do occur in that system but the phonons must also be taken into account, shown in figure 3.23(B). It leads to a vast distribution of possible phonon and non-phonon assisted transitions. That these two different crossing types are happening for carbon materials is under current debate for the interpretation of recorded data in the literature [100].

3.12 Conclusion

As can be seen from section 3.9, one can use slightly different models for having a nice fit. Also the interpretations are justifiable and can explain the data. But as stated above, it will never be possible to explain the small peaks with this approach. So a new nonlinear optics approach is made and the third order polarization is calculated. By using the time constants obtained from IR pump-probe measurements, a certain certitude for the minimization process is ensured and checked with a different method. Besides, the curves can be well described. Further investigation needs to be made to describe the small peaks next to the maximum. They could be implemented into the model if more Feynmann diagrams are being taken into account.

It is for now difficult to talk about a single model that describes graphene, graphene oxide or graphite oxide used here, since all the materials have such a variety of

characteristics, starting with the number of layers, which influences the band structure. Certainly to wrap all these up will be an important task for bringing a certain overview in that field of decay processes in carbon materials.

With these results a starting point is set for using carbon based materials as a substrate for e.g. molecules in pump-probe experiments. It would be more appropriate than using anorganic materials, since it is closer to their natural environment (which is organic). Such experiments could be more fertile for life science.

Chapter 4

Lactose

4.1 Motivation to study lactose

One central motivation for building the pump-probe setup introduced in chapter 2, is the possibility to investigate hydrogen bonds. These bonds play a role in all kinds of molecular structures and water environments. Maybe one of the most known example for its importance is ice [103], the form of which emerges due to hydrogen bonds. Another example is the DNA helix, in which central parts [104], the nucleobase are connected by hydrogen bonds, see figure 4.1.
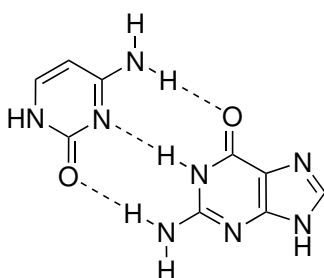
FIGURE 4.1: The dashed lines show the hydrogen bonds between cytosine and guanine which are core parts of the DNA helix (nucleotide base pairings).

Hydrogen bond (HB) : Valence electrons are responsible for building up a chemical bond. If hydrogen atoms are involved, a HB can occur. It can be displayed as X-H...A (the dotted line is the HB) and the bond can be separated in two parts. One group with X as X-H is the the proton donor and the other is A the proton acceptor. The following three interaction mechanism describe the nature of the HB: electrostatic, dispersion and induction. At the position of the hydrogen atom, a positive partial charge $\delta+$ is induced, because of the difference of electronegativity between the donor and the acceptor parts. Therefore, the acceptor has a negative partial charge $\delta-$. The involved acceptor atom can be for

instance oxygen, fluorine or nitrogen. The energy of that bond lies in the range of 0.1 eV, depending on the surroundings and is weaker than e.g. covalent bonds [105, 106]. In figure 4.2 an example is shown for two water molecules (dimer) that are linked to each other via hydrogen bond. Typically the bond length is smaller than 3.5 Å, has a smaller angle opening of the O-H...O connection than $\pm 30°$ [107] and a bond strength of 3.09 kcal/mol [108]. However, this is only the tip of iceberg because water can build many different cluster formations, up to decamers [108]. Also, possibilities to calculate material characteristics like heat capacity over a big range of different environments is still an issue. That leads to the experimental investigation of such bonds under different conditions and surroundings.
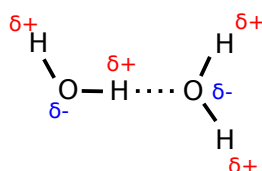
FIGURE 4.2: Hydrogen bond between two water molecules depicted by a dashed line. The positive or negative electronegativity is assigned by $\delta+$ and δ- respectively.

Nevertheless in the following, the focus lies on lactose, which was chosen because of its low lying absorption band, below 1 THz, which makes it interesting and accessible for our THz pulse bandwidth. In the same way, one could also have looked at glucose, fructose [109] or biotin [110] but they have absorptions at higher frequencies or are expensive in comparison to lactose.

Lactose has already been studied from different points of view, e.g. in relation to dairy products, in chemistry [111] or in physics by spectroscopic methods [112]. Its structure can be seen in figure 4.3 and consists of a combination of galactose and glucose. For lactose monohydrate there is one water molecule in the vicinity of the lactose molecule and several hydrogen bonds can be found if looking at several lactose molecules which interact with each other, see figure 4.11 or in the publication of Beevers et al. [113].

FIGURE 4.3: Structure of lactose.

To better understand this interplay and its dynamics, pump-probe measurements were performed. These have so far not been done in a lactose pellet (to our knowledge). What was done is to look at the change in absorption of a solution of lactose in w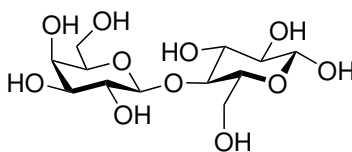ater, studied by Heugen et al. [114]. They looked at the solvation shell around the lactose molecule and found out that 123 water molecules play a role in that layer. It is important to mention here that a lot of studies have been done on water, for instance in [107, 106, 115, 116] but for life science the interplay of water and a molecule via hydrogen bond plays a huge role.

It is instructive to look into typical time scales for hydrogen bond dynamics. A tremendous body of work exists on water dynamics. Therefore, a short summary on the hydrogen bond dynamics in water will be presented, as studied with time-resolved vibrational spectroscopy. Photon echo spectroscopy has been applied to study the spectral diffusion of the local OH stretching mode. It has been found that ultrafast structural rearrangements of the surrounding hydrogen bond network lead to the loss of frequency correlation within 50 fs [115]. On the order of picoseconds a heating effect can be deduced. This is a result for instance of the vibrational relaxation in the water molecule. Generally, it is not simple to disentangle intra- and intermolecular vibrational relaxation. The modes (intra- and intermolecular) are strongly coupled in water. Nevertheless, in that timeframe the structure of the hydrogen bond network also relaxes [116]. Interestingly the lifetime of the hydrogen bond is also in the range of 1 ps [108]. However, these time specifications are in liquid water and here the molecule is investigated in the solid state as a monohydrate. Therefore, any comparison should be treated with care.

The pump-probe measurements were carried out with a pump wavelength of 3 μm coming from an OPA described in 2.10. THz radiation generated by the LN crystal was used for the probe pulse. Two aspects recommend THz measurements: The first is when collective rather than local vibrational dynamics are of interest. It can probe the dipolar relaxation of water and track its change after a pump pulse, for instance. This was also done by Backus et al. [5] for aqueous solutions (for instance pure water and HCl in water). It shows the dynamic of the hydrogen network, which correlates with the temperature. Thus, the warmer the water, the more THz is absorbed because of a blueshift of the absorption peak (for water molecules at 20 GHz representing their reorientation). The second is that in the THz frequency region, rotational modes of lactose lie (as well as other molecules, like nucleobases [117]). Recording induced changes to these modes would afford information on timings for processes happening between the OH stretching vibration of water and the rotational mode of a molecule.

To disclose the results: the time dependence could not be identified, since the signal to noise ratio of the experiment was not sufficient. There are results from

measurements which indicate a dynamic. However, in order to obtain clear results, a new attempt must be made with a better detector and/-or higher IR pump power.

4.2   Sample preparation

To study lactose at THz frequencies, at least two approaches may be used. One is to grow lactose crystals but that didn't yield the desired results, because their size did not exceed 1 mm and the THz beam size at the focus spot is on the same order. In appendix E the steps taken for growing crystals are described.

The other method is to press pellets from lactose powder and PTFE or PE. The mixture is done carefully because lactose absorbs strongly in the IR (as shown in 4.6) and the pellets should therefore be thin but still stable. By only using lactose for the pellet it does not hold and crumbles. So PTFE was used for mixing due to its small absorption in the THz (see figure 4.4) and its small particle size (mean particle size: 6-9 μm), in comparison to PE that could only be purchased with a particle size of 40-48 μm. Even after grinding for 20 min with a pestle and mortar, a stable and sufficiently thin (0.2 mm) pellet could not be produced with PE.

α-Lactose monohydrate (BioXtra grade)[1] and and Polytetrafluoroethylene (-Powder)[2] were obtained from Sigma-Aldrich Chemie GmbH and Goodfellow GmbH, respectively and used as received.

The press is a MP250 from Maassen GmbH. Each pellet has a diameter of 13 mm and a weight of 9 tons was applied to press them.

---

[1] Article number: L8783-1KG
[2] Article number: 531-672-48, 200g
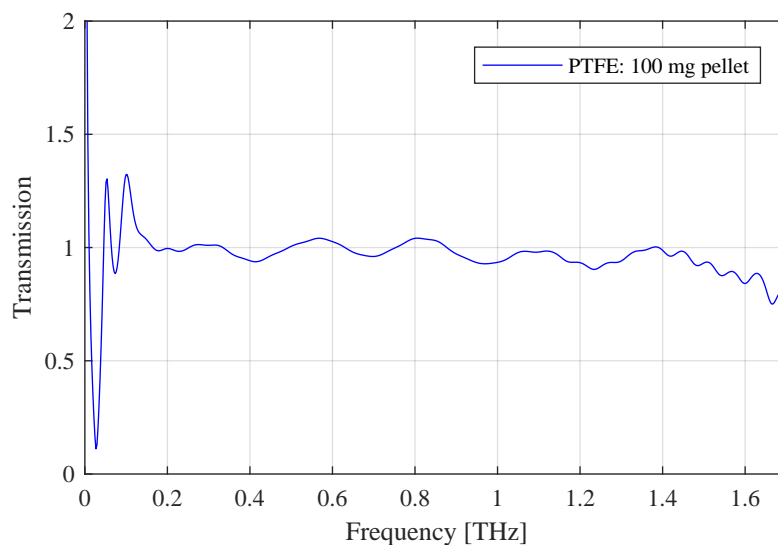
FIGURE 4.4: Transmission spectrum of a PTFE pellet. The oscillatory feature is an artefact from the FT because the EOS stage could not be moved long enough to fully capture the free induction decay of the water vapor vibrations. A better purge mechanism could prevent this oscillatory signal.

4.3 IR spectrum of lactose

In preparation for pump-probe measurements with the THz spectrometer and a pump beam coming from the OPA, spectra of lactose pellets were recorded with an FTIR Vertex 70 spectrometer from Bruker. In figure 4.5 the absorbance of PTFE pellets with different masses can be seen, which were taken for characterizing PTFE. As expected, with higher masses (thus higher thickness length), the absorbance increases. From 2700 cm^{-1} (3.7 μm) towards higher wavenumbers the absorbance has no specific features except for a small peak at 3560 cm^{-1} (2.8 μm) from the PTFE [118].
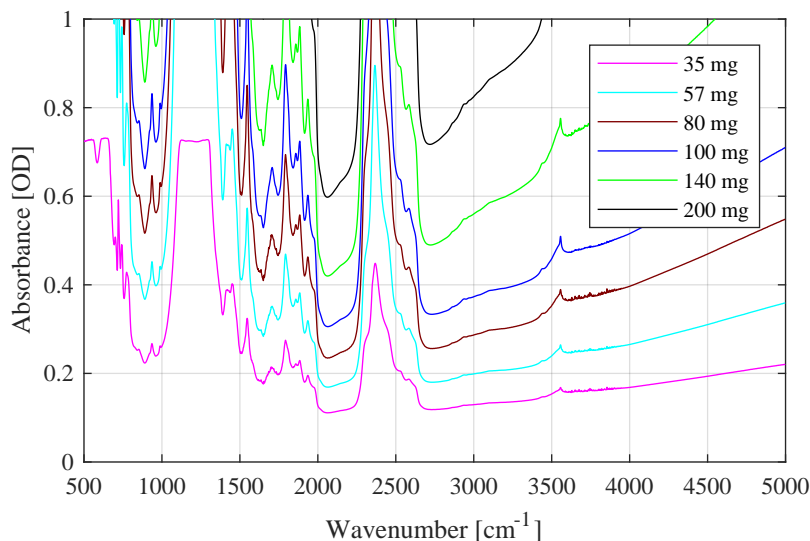
FIGURE 4.5: IR spectrum of PTFE pellets with different masses, measured with an FTIR spectrometer.

Having shown that PTFE has no special features around the water absorption lines (around 3μm, $3333\,\mathrm{cm}^{-1}$) and does not absorb strongly in that frequency range, it is therefore well suited as a filler material for making pellets (PTFE is also highly transmissive in the THz range). Thus, in figure 4.6 the absorbance spectra of different mixtures of lactose and PTFE are shown. In blue the absorbance of a 35 mg PTFE pellet is drawn. This should serve as a refernce since it is difficult to produce precisely the same composition (i.e. the same mass of PTFE) for every pellet. The black curve shows a measurement of a pellet for which the reference 35 mg PTFE pellet was directly subtracted by the FTIR software. Note that measurements with absorbance values higher than 1.5 (transmission of 3.2%), or worse when greater than 2 (transmission of 1%), are not reliable due to the fact that only a very small part of the IR radiation can reach the detector.
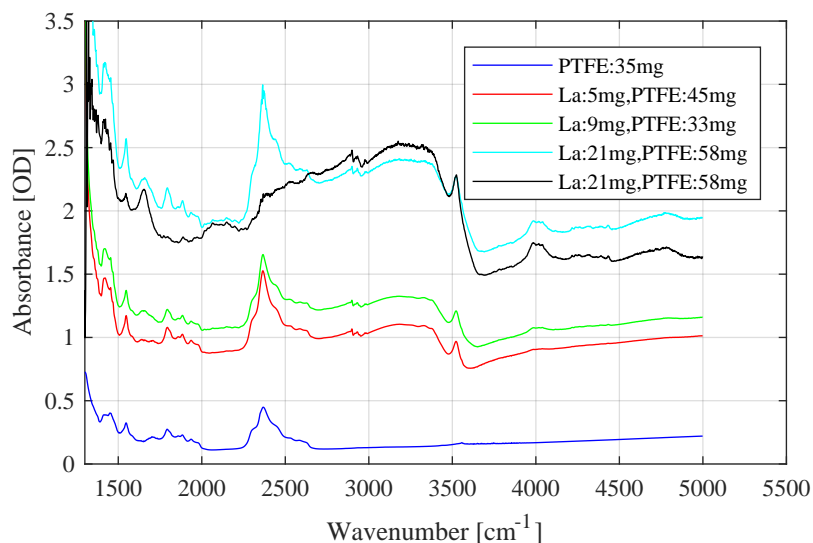
FIGURE 4.6: IR spectrum of lactose pellets with PTFE with different masses, measured with an FTIR spectrometer. The blue curve shows the spectrum of PTFE alone. In black is the spectrum for which the measurement was performed with the 35 mg PTFE pellet as a reference and so its absorbance is automatically subtracted. The other curves show the absorbance of the mixture without direct subtraction (except for ambient air).

In the following measurements two pellets were used: they are the one with 9 mg lactose and 33 mg PTFE (0.187 mm), since its absorbance lies in the range of 1 to 1.5 OD, and the one with 21 mg of lactose plus 58 mg of PTFE. As a reference, a lactose measurement provided via NIST (National Institute of Standards and Technology)[3] is shown in figure 4.7. It can be seen that the features of the lactose plus PTFE pellet do arise from lactose and PTFE. At wavenumbers around 3333 cm^{-1} the absorbance comes mostly from the lactose.

---

[3]IUPAC Standard InChIKey: WSVLPVUVIUVCRA-SIQISOGJSA-N
CAS Registry Number: 64044-51-5
Data taken from: http://webbook.nist.gov/cgi/cbook.cgi?ID=C64044515&Mask=80
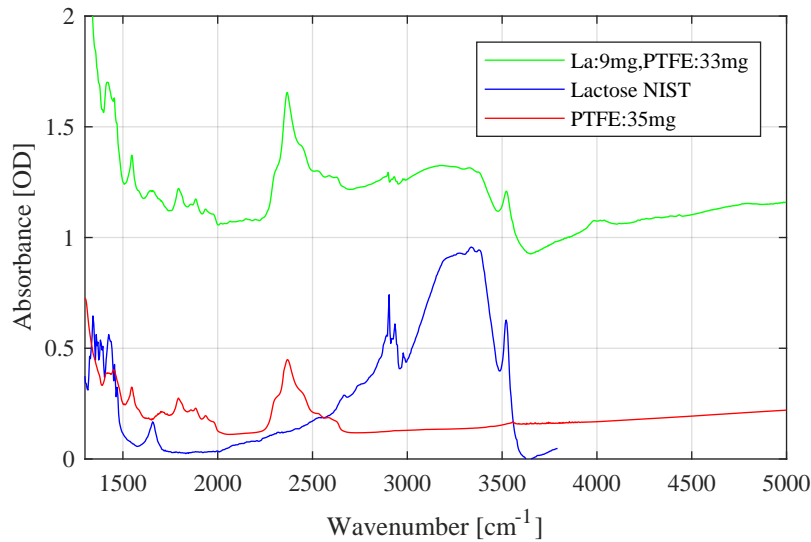
FIGURE 4.7: IR spectrum of a lactose pellet with PTFE (9 and 33 mg
respectively) in green and as reference a curve of lactose provided by
NIST [119] in blue. In red a PTFE pellet is shown.

4.4   Linear THz spectrum of lactose

In this section, the THz spectra of lactose pellets with PTFE are shown. They were
recorded with the THz setup described in chapter 2 and the radiation source is the
LN crystal.

4.4.1   Thick pellets

In figure 4.8, the spectra of a thick lactose plus PTFE pellet is shown, as the spectrum
of a PTFE pellet as reference and the spectra without any sample. It can be seen that
by purging the setup the water absorption lines are greatly diminished (comparison
of blue and cyan curve) but unfortunately do not vanish completely, which means
that the purge generator does not completely eliminate the water vapour. The red
curve shows a pellet of 100 mg PTFE and no absorption lines can be seen, which
makes PTFE a good filler material for pellets that are irradiated with THz radiation.
A thick pellet of 110 mg lactose and 110 mg of PTFE is depicted in green. Two clear
absorption lines are in the spectrum within the bandwidth and discussed at the end
of the section.
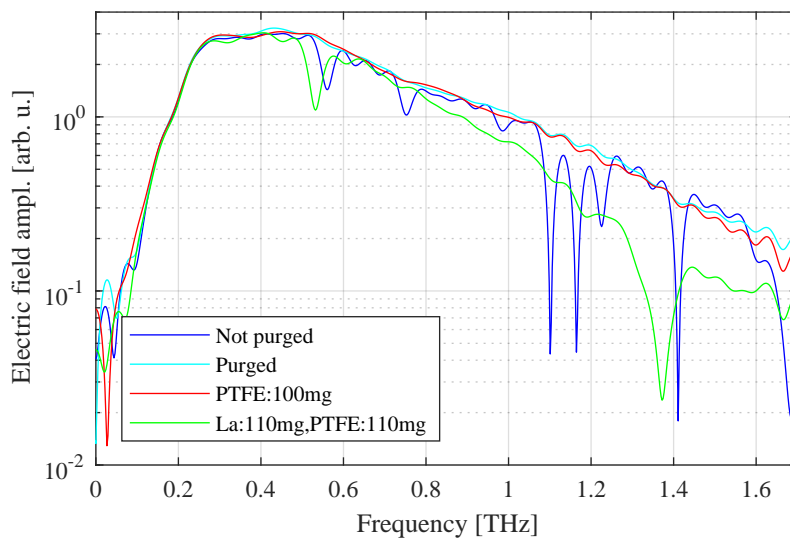
FIGURE 4.8: THz spectra of air and pellets. In blue is shown the water vapour in the setup and in cyan the spectrum when the setup is purged. The red curve is a PTFE pellet of 100 mg and in green a pellet with 110 mg of lactose mixed with 110 mg of PTFE.

4.4.2 Thin pellets

As can be seen from the IR spectra in section 4.3 the pellets must be very thin for transmitting IR light and enabling the irradiation of the whole pellet volume. Therefore, the THz spectra of thin pellets used for the IR measurements are shown in figure 4.9. The red curve is a spectrum from 9 mg lactose with 33 mg of PTFE pellet (thickness: 0.187 mm) and in green a pellet of 21 mg lactose with 58 mg PTFE (thickness: 0.318 mm).
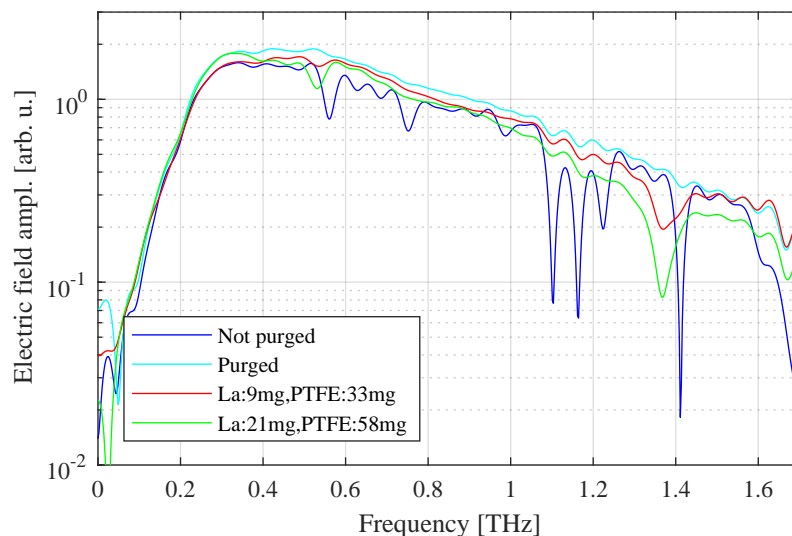
FIGURE 4.9: In blue the non purged setup spectra is shown and in cyan when it is purged. Red and green are pellets with 9 and 31 mg lactose respectively.
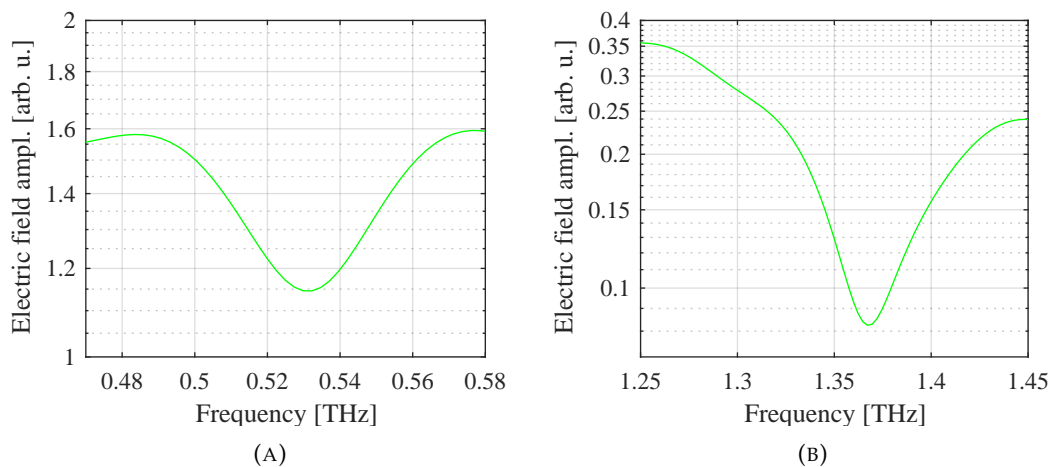
FIGURE 4.10: In (A) the absorption line at 0.53 THz and in (B) the one of 1.38 THz of a lactose+PTFE (21 mg + 58 mg) pellet can be seen.

4.4.3 Lactose absorption lines in the THz

Lactose has already been widely studied in the leterature and the absorption lines at 0.53 and 1.38 THz seen in figure 4.10(A) and (B) respectively (and 4.8, 4.9) can be assigned to it [112, 120, 20]. It is also clear that the more lactose the pellet has, the more it absorbs. Both lines represent molecular rotational modes as mentioned by Saito et

al. [121]. Maybe a better description is to call it hindered rotational mode as done by Allis et al. [122]. Both mentioned authors used the DFT method for calculating the modes measured in the THz frequency region.

As mentioned above (section 2.5), the close absorption lines between water and lactose show clearly that the setup must be purged with dry air or nitrogen, so that there is no overlap.

4.5 Pump-probe with lactose

Pump-probe measurements were performed with a pump wavelength of 3 μm generated by an OPA (see appendix E.3, detailing how the pump beam was focused onto the sample) and THz probe generated in an LN crystal. The pump excites the OH stretch vibration resonantly thereby introducing excess energy into the α-lactose crystals. Backus et al. showed that IR-pump-THz-probe spectroscopy is sensitive to temperature changes in the far IR region on ultrafast timescales in less than 200fs [5]. This offers possibilities to observe thermalization dynamics directly in the far IR region which is sensitive to delocalized, intermolecular and rotational modes of (bio)molecular systems. In case of α-lactose the aim is to observe the energy flow from the high-energy OH stretch vibration into its low energy hindered rotational mode [113]. It is expected that the hydrogen bonds between the water and lactose molecules become weaker with increasing temperature which should affect the frequency or the movement of the hindered rotational mode. In figure 4.11 two α-lactose monohydrate molecules are shown with and without the hydrogen bond network (data taken from [113] and plotted with Mercury). Additionally, DFT calculations show that this network is important for the structure and the absorption in the THz region [122].

(A)

(B)
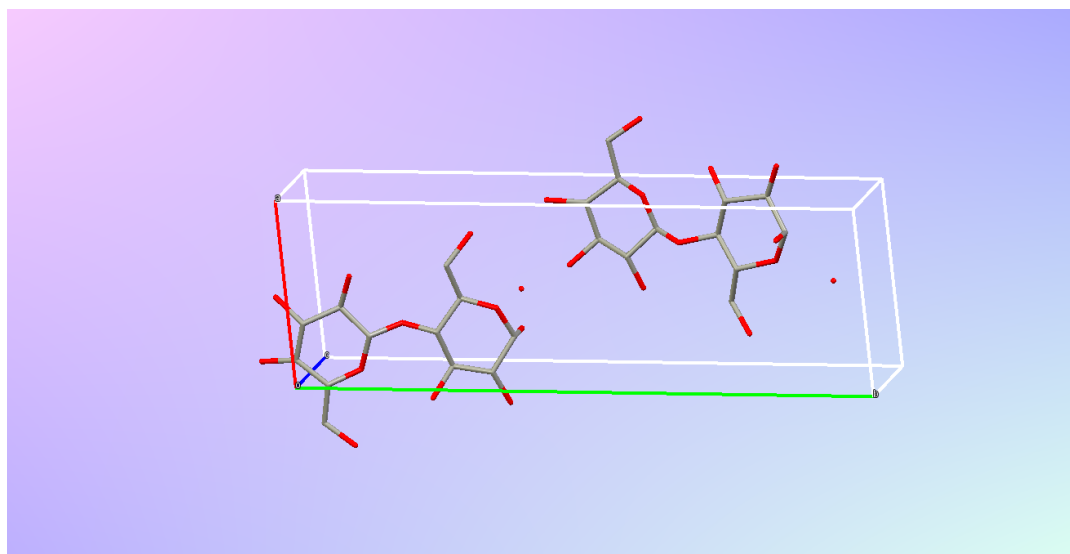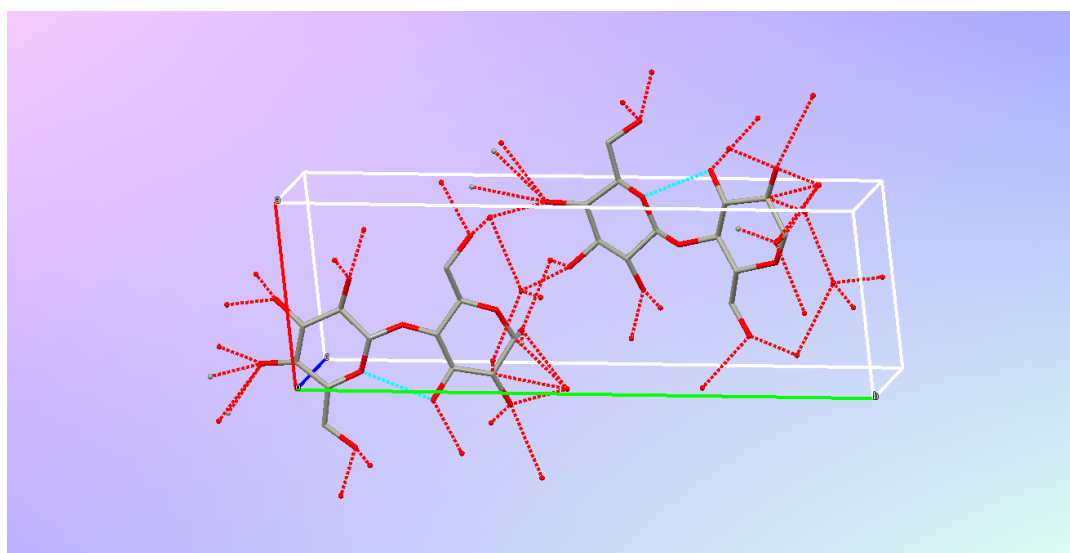
FIGURE 4.11: Two α-lactose monohydrate molecules are shown with
carbon atoms at grey vertices and oxygen atoms at red vertices. In
(A) no hydrogen bonding is shown for clarity. Red single dots depict
the oxygen atom of the water molecules. (B) shows the intermolecu-
lar hydrogen bonds as red dotted lines. The cyan dotted line shows
intramolecular hydrogen bonding. Data taken from Cambridge Crys-
tallographic Data Centre, Deposition number: 1202386, Compound
Name: α-Lactose monohydrate, publication [113], plotted with: Mer-
cury 3.10.

Before discussing the results in detail, it must be noted that the signal to noise
ratio is too low to declare that a dynamical signal can be seen. In figure 4.12 the

absorbance change[4] of the lactose pellet is shown when the pump beam is blocked. All other parameters are set like for an experiment with open pump path. 49 scans were averaged here. The best case would be to see a flat line at zero but here clearly a shape is seen. The noise in absorbance is on the order of 0.02. Also at the absorption frequencies of lactose (see figure 4.10) extrema can be seen.

In the following pages of this section, the measured pump-probe experiments are shown to discuss what was observed, but without any analysis, because the signal to noise ratio is on the order of the measured signals.
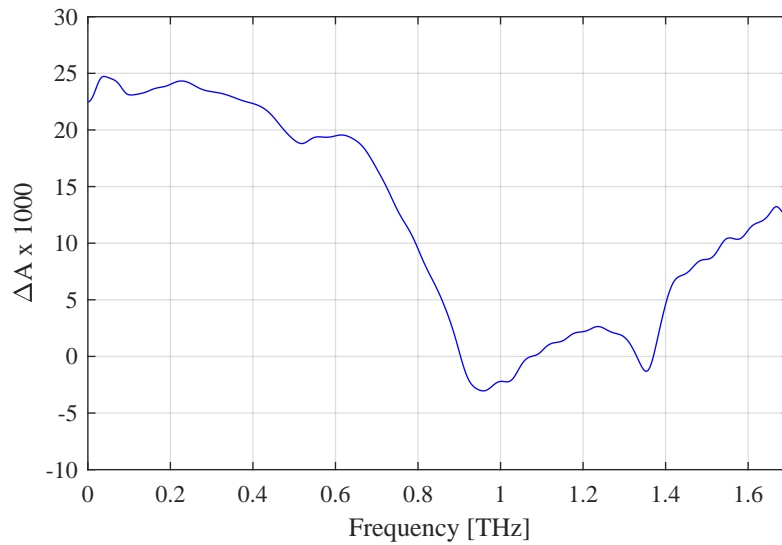
FIGURE 4.12: Reference measurement of the absorbance change in lactose, when the pump beam is blocked.

In figure 4.13 the pump-probe experiment with a lactose+PTFE pellet (21 mg of lactose) is shown. The absorbance change is on the same order as the reference measurement in figure 4.12. As stated above, delay times corresponding to dynamic changes in liquid water were chosen for scanning the THz probe beam: between 200 fs and 1 ps [115, 116]. At 1.38 THz, the absorbance increases from 200 fs to 500 fs.

---

[4]Calculated by $\Delta A = -log \frac{|E_{Pumped}(\omega)|^2}{|E_{NotPumped}(\omega)|^2}$.
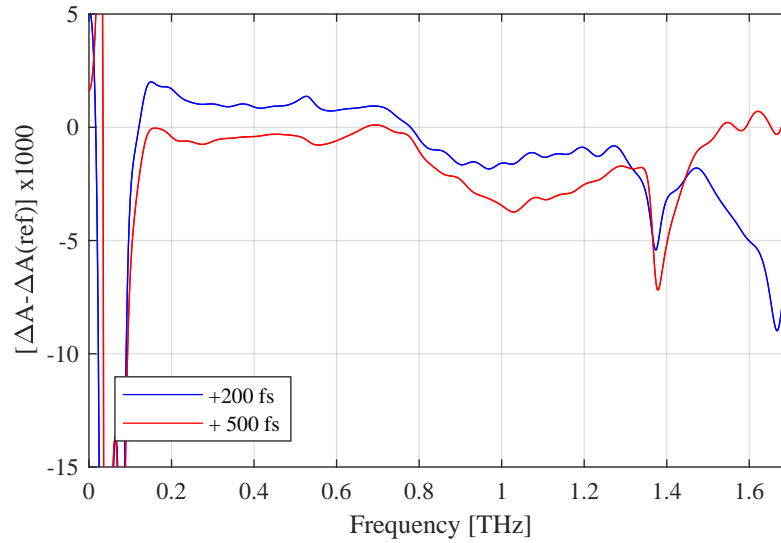
FIGURE 4.13: Pump-probe TDS THz scan of a lactose (21 mg) pellet
with different delay times (see legend).

Figure 4.14 shows a pump-probe experiment with a lactose+PTFE pellet (9 mg
of lactose)[5]. Also here the signal is on the same order as shown in the reference
measurement. The absorption line at 1.38 THz changes with increasing time, but not
as clear as in figure 4.13[6].

In the pump-probe experiment performed by Backus et al. [5] they had a pump
energy of minimum 20 μJ with a spot size of 300 μm. In comparison, the pump
energy here is $\sim$1.2 μJ on a spot size of 700 μm.

---

[5]Pump fluence on that day: 40 μJ/cm^2

[6]Pump fluence on that day: 32 μJ/cm^2
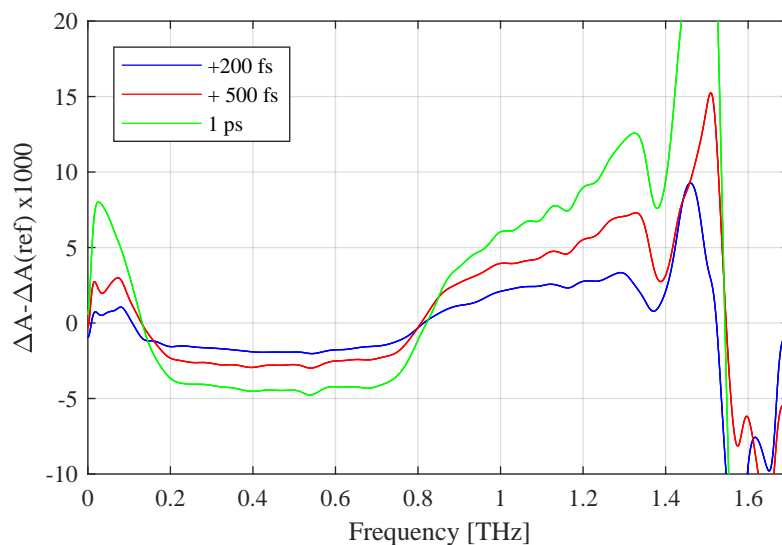
FIGURE 4.14: Pump-probe TDS THz scan of a lactose (9 mg) pellet with different delay times (see legend).

4.6 Results and discussion

Lactose pellets with PTFE were mixed in a ratio suitable for IR-pump-THz-probe measurements. This was checked with FTIR and linear THz measurements. Note that the pellets must be very thin, around 0.2 μm.

As mentioned previously, the signal to noise ratio is insufficient to come to the conclusion that the 3 μm pump is absorbed by the OH vibration, so that the hydrogen network is stimulated and a change is detected in the hindered rotation mode of lactose by the THz probe pulse. In the spectra it might seem that at longer time delays at the absorption frequency of 1.38 THz the peak is increasing, but no conclusion can be made.

In the experiment reported by Backus et al. [5], the pump fluence was more than 200 times higher than used in this thesis, and their detected signal on the order of the signal to noise here. A better signal to noise ratio may already be sufficient for a successful measurement. Since it is a third order process, the third order polarization increases quadratically with the pump fluence. Therefore, increased pump fluence has a dramatic effect on the sample response. Normally, pump-probe experiments are designed so that the pump spot size is larger than the probe size, for a homogeneous excitation in the probed region of the sample. However, Backus et al. used a pump spot diameter (diameter: 0.3 mm) that is three times smaller than for

probe (THz spot diameter: 1 mm). It can be suspected that no signal was detected otherwise.

4.7   Outlook

The next steps would be as mentioned in the outlook of the chapter on the THz setup (section 2.13). A detector with a better signal to noise ratio should be used, as is planned with the balanced detector. Also, higher pump power in the IR from an OPA would increase the energy redistribution via the hydrogen network and would perhaps affect the rotation mode of lactose more strongly.

Repeating the experiment after some changes would possibly lead to a measurable change in the THz probe beam and so to new insights about the dynamics of hindered rotational modes.

Chapter 5

MOKE - Magneto-optic Kerr effect

5.1 Motivation to study the MOKE

In this chapter, magnetized sheets are studied with a modified pump-probe setup as introduced in chapter 2. The idea is to shine THz light on a ring like structure, which creates a magnetic field, that changes the spin orientation of the sample. This should modify the polarization, amplitude or both of a probe beam, which is directed to the sample and reflected by it [123]. Thus, a time dependent Magneto-optic Kerr effect (MOKE) is expected to occur. The samples are produced and analysed beforehand by the scientific group of Prof. Oepen, who provided them (described in 5.4).
A similar experiment was performed by Vicario et al. [124]. They studied also Co (cobalt) films, which magnetization orientation is being influenced by a THz pulse. The MOKE was probed by an 800 nm pulse, as in this case. They recorded a MOKE signal, following the pump THz field.
This project was carried out in corporation with Norbert Weinkauf from the group of Prof. Oepen.

5.2 Introduction of the MOKE

The MOKE describes how a reflected beam is being influenced by the magnetization of the studied surface. It can change the type of polarization (linear or circular), rotate the main polarization axis and change the intensity. These effects can occur separately or together, depending on the individual MOKE.
Magnetization is described by the magnetic moment $\vec{\mu}$ per volume part dV. $\vec{\mu}$ is proportional to the spin $\vec{s}$ (for electrons: $\vec{\mu} = g_e \mu_B \frac{\vec{s}}{\hbar}$, with g_e the Lande factor and μ_B the Bohr magneton), if described in an atomic and quantum-mechanical picture [125, 126]. Which one of the possible MOKE types below will occur are determined by the magnetization orientation of the samples [127, 128].

For the change in the reflected beam, a more comfortable description of the magnetization is as follows

$$\vec{M} = \chi_m \vec{H},$$ (5.1)

with χ_m the magnetic susceptibility and H the magnetic field strength. From the χ_m matrix elements, the induced change can be derived [129]. It describes how the material behaves in a magnetic field.

Considering that the incoming probe beam is linearly polarized [130], and depending on the sample surface's magnetization, the outgoing light can be altered as follows:

1. If the magnetization points outside the surface, one speaks of polar MOKE (PMOKE, see figure 5.1(A)). By shining linear polarized light on the sheet, the reflected beam gets altered. In general, linear polarized light can be split into left and right hand rotating waves. They are affected differently by the vertical magnetization, since both parts encounter a different refractive index and absorption coefficient. As a result, the outgoing beam is elliptically polarized and the optical axis is rotated by the Kerr rotation angle θ. This effect is often measured with a setup in which the incident probe beam is nearly at normal incidence (vertical to the sample plane).

2. For a magnetization that is vertical to the optical principal plane and the ingoing beam polarization, the outgoing beam exhibits a change in intensity, as shown in figure 5.1(B). This is referred to as transversal MOKE (TMOKE).

3. When the magnetization is in plane with the principal plane and the magnetized surface, the effect is called longitudinal MOKE (LMOKE). Here the outgoing beam gets elliptically polarized and the polarization axis can be altered as in PMOKE (see figure 5.1(C)).

Other phenomena or geometries can also occur, but are not discussed here.
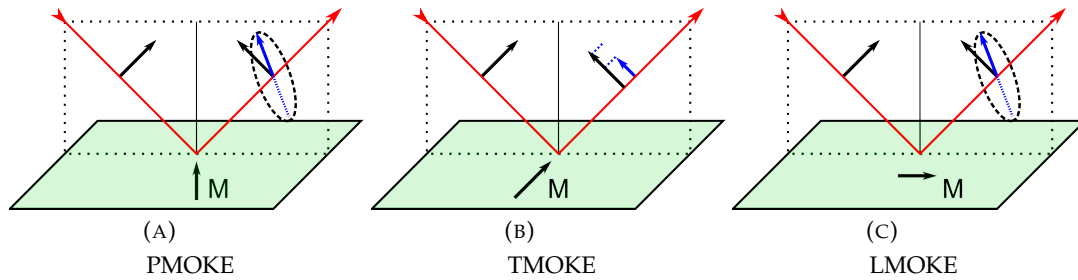
FIGURE 5.1: In the figures above, three different MOKE types are
sketched. The sample surface is slightly green and the ingoing p-
polarized light is shown in red, as is the outgoing beam with the pos-
sible induced change in intensity, ellipticity and polarization axis.

5.3 Experiment

For performing a MOKE experiment, the setup shown in figure 2.1 must be slightly
modified. The pump path for the THz generation remains unchanged. Since the
THz pulse is used as a pump, it only strikes the first three parabolic mirrors and is
focused onto the sample.

The 800 nm probe beam is obtained from the transmission of a 90:10 (R:T) beam-
splitter on the breadboard (first mirror on the upper left corner) and is collimated
afterwards by a 1:4 telescope, see figure 5.2. This collimated beam hits the outer part
of the third parabolic mirror which is focusing the beam onto the sample, where the
THz pulse did excite the structure. The 800 nm reflection of the magnetized surface
is collimated by the opposite outer part of the third parabolic mirror and guided
towards the EOS beam path, described previously (section 2.2). In order to balance
out a non changed probe beam by the sample, a half wave plate is used instead of a
quarter wave plate. The electronic detection scheme used in this experiment, is the
same as described before in section 2.6.
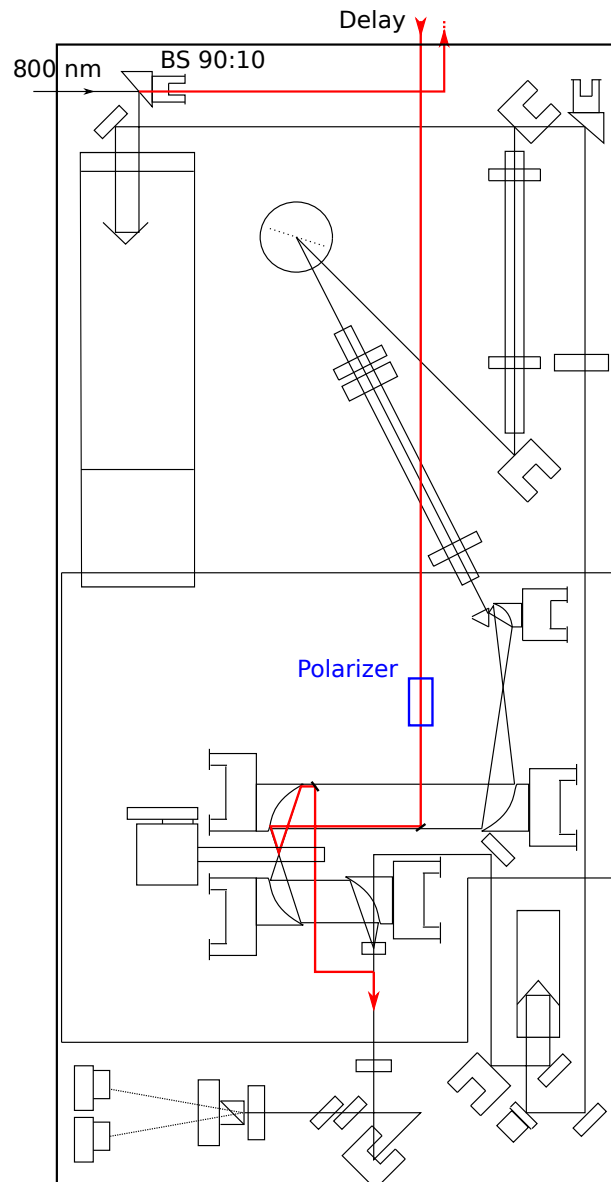
FIGURE 5.2: Essentially the THz MOKE setup is the same installation as shown in figure 2.1. Here, the THz is the pump pulse and the 800 nm probe beam is following the depicted red line. The parabolic mirror is focusing it onto the sample and gets collimated on the opposite mirror edge after reflection on the sample. Afterwards, it is guided into the EOS beam path. In blue a possible position of a polarizer is shown, which would be installed as a next step for a new attempt of the MOKE experiment.

5.4 Sample

The sample provided is a rectangular Co or Pt-Co-Pt (Pt: platinum) pad [131] within a split ring resonator in the shape of an Ω. The latter one is of gold and the overall substrate is GaAs. The THz pump pulse is inducing a current in the split ring that results in an oscillating magnetic field within the structure [15, 132]. This causes a transient change in the magnetization of the pad. Calculations were performed by Kumar et al. [133], stating that with a SRR, the magnetic field of a THz pulse could be enhanced up to a factor of 200. Therefore, it is important that the probe beam hits the inner part of such a structure, at the point where the magnetization is maximum in order to produce the maximum possible change in polarization (or amplitude).

Split ring resonator - SRR As the name implies, an SRR is a ring structure with a gap. The ring can be found in various geometries and materials, depending on the desired characteristics. The metamaterial can have for instance a negative refractive index [134] or other specifications that cannot be found in nature [135].

In this experiment, an incoming electric field, such as the THz pulse, is inducing an electric current in the ring. It excites oscillations in the wire and builds up a magnetic field within the structure that is oscillating. The gap of the ring can be described as a capacitor, where strong magnetic fields can build up.

If the rings are arranged as a grid, they can be used as a filter for microwave radiation, that absorbs waves of one specific frequency or at higher harmonics. In equation 5.2, a rough frequency ν estimation can be calculated

$$\nu = \frac{c \cdot m}{2 \cdot n \cdot l} \tag{5.2}$$

where m denotes the m-th order, l the length of the extended ring and n the refractive index. The m-th mode is excited if l=m$\frac{\lambda}{2}$ is fulfilled (λ : *wavelength*). By using Babinet's principle the array can be used as a filter that allows only a single frequency or higher modes of it to pass [136].

5.5 Results and discussion

The expected result of the experiment would have been to record an oscillation in the s- and p-polarizations difference of the 800 nm beam. It should arise from the generated precession of the spin that is being kicked out of equilibrium by the THz pump pulse [137].

Unfortunately, no such signal could be detected. By beam walking of the 800 nm over the golden structures, it can be ensured that the probe beam is being reflected

in the middle of the split ring. This can be seen by a different amplitude at the oscilloscope, since the reflection of gold is higher than the one of the substrate or pad. Also, the THz focus spot size, which is larger than the probe beam should hit the structure. Thus, it is not expected that the missing signal change was due to an alignment problem.

It is suspected that it is necessary to put an extra polarizer into the probe beam path, to purify the polarization of the 800 nm probe beam. Spectra Physics does not specify the polarization ratio of the amplified laser system, but due to the seed pulse from the oscillator and the gratings in the compressor plus stretcher it should be relatively high (at least more than 10^{-2}).

For the experiment performed by Vicario et al. [124], the sample was set in an external magnetic field (0.01 T) to align the magnetization and therefore, improving the signal to noise ratio. Additionally, their THz pump fluence towards the sample was 0.8 mJ/cm^2 compared to the 0.01 mJ/cm^2 applied here.

5.6   Outlook

Three things can be changed to enhance the chance of a succesful experiment. As mentioned above one option would be the installation of a polarizer that treats the probe beam, resulting in a higher polarization ratio[1]. The second is the cooling of the LN crystal with a cryostat. The result would be a stronger THz pump pulse leading to a bigger displacement of the magnetic spin. Finally, the installation of a balanced detector would enhance the detection sensitivity.

---

[1]Like one from Bernhard Halle Nachfl. GmbH, with an extinction ratio of 10^{-6}.

Chapter 6

Conclusion

6.1   Overall summary

The first part of this thesis incorporated the design and set-up of a versatile pump-probe spectrometer. The system can presently be operated with several pump wavelengths, ranging from the UV/vis to the IR. The probing is performed by a THz pulse. This probe pulse has a bandwidth of 0.2 to 1.5 THz. Its pulse energy is in the range of hundred nJ. The detection of the THz pulses is performed via EOS, that enables the user to record the electric field transient directly. After finishing the construction and testing the usability, several experiments were performed which are summarized below.

One experiment was to measure the decay behaviour of excited free charge carriers by a laser pump pulse and to probe it with THz radiation, since it is sensitive to the carriers. The decay measurements were performed on a free standing graphite oxide film. It was specified by the manufacturer to have an oxygen level of 41 to 50% and consisted of several thousands of layers stacked on top of each other. Three different pump wavelengths were used: 800 nm, 2 μm and 3 μm in order to check whether there is a dependency. It must be pointed out that this was the first IR-pump-THz-probe measurement on such a system.

By comparing the decay curves, smaller peaks next to the main maximum can be seen when pumping at 2 μm. To model these, an approach of nonlinear optics introduced by Mukamel must be chosen. This way, the slope of the measured curves can be correctly described. As a decay model for the carriers a sum of exponentials was used. The time constants for this were obtained by IR-pump-probe measurements (by Amul Shinde) on the same sample membrane. Since the minimization process worked well with these values, they appear to have been correctly determined.

It is important to use two independent approaches to check the time constants, because there is an ongoing debate in the literature about the decay values and how to interpret them. It appears that the electron-electron scattering process in the first 30 fs, which is very often mentioned, has only a marginal influence. Also such a time

constant is not required for describing the data. Perhaps future studies will lead to a better insight. It is also important to carefully check if the approximation of the Franck-Condon principle can be used.

The four time constants can be separated into two groups: the first three time constants describe the relaxation process via phonons. For the third time constant, it might be strongly dependent on the oxygen groups' related defects. But further studies need to be done in that direction. Afterwards the recombination process of the carriers takes place. Probably first via the induced defects from oxygen groups and then by structural defects as found in semiconductors. This gives a complete image about the decay mechanism in the GO membrane.

Two more experiments were carried out.

One was a pump-probe experiment on lactose monohydrate pellets. The pump wavelength was 3 μm which should excite the OH stretching mode of the water surrounding the molecules. Via the hydrogen bound network in the system, the induced energy should reach the lactose molecule. The idea was that this would affect the low lying rotational mode of it and that a possible change would be observed.

The purpose of the other experiment was to study magnetized surfaces via the MOKE. The magnetic Co-sample was surrounded by a split ring resonator. By inducing a current into the ring by a THz pump pulse, an oscillatory magnetic field would build up with a maximum magnetic field strength at the position of the sample. This way the spin orientation would be forced out of equilibrium. Polarization or amplitude of a 800 nm probe pulse, that is reflected by the magnetic surface should be altered, after a change in the MOKE by the magnetic field from the ring was induced.

A variety of different experiments on quite diverse samples were performed. Not of all of them delivered the desired results. However, the potential of the setup was demonstrated and approaches to successfully perform the experiments were highlighted.

6.2 Outlook

As mentioned in the outlooks of the chapters before, a couple of improvements of the setup would certainly increase its usability. These are:

A balanced detector that subtracts the signals of the s- and p-polarization of the EOS beam directly after the detectors. This would result in a better signal to noise ratio. Its construction has already been initiated. After delivery it only has to be installed at the position of the single detectors.

To build a cryostat around the LN crystal would increase the emitted THz power (at

least by a factor of 10) and the bandwidth (going above 2 THz). Chances are that with an enhanced THz pulse the setup could also be operated in the pump mode and a larger frequency range could be probed.

By setting up a cryostat that is able to cool the samples, other effects can be observed e.g. phase transitions, conductivity change or low frequency modes (e.g. rotational) of molecules that are covered by other modes at room temperature. In this compilation the combination with the IR detection unit could offer new possibilities.

Free standing GO membranes were extensively studied by the group of Nils Huse. A possible step forward would be to use these films as a substrate. For molecules that have been studied only on anorganic substrates so far, the carbon material resembles a more realistic environment.

With the changes to the setup described above, new efforts for experiments with lactose and the MOKE become feasible. As for investigations of lactose the use of a balanced detector would be the first choice. Keeping the sample in a cryostat would increase the probability to see a change in the hindered rotational mode induced by the excitation of an OH stretching mode by the 3 μm pump pulse.

The use of the balanced detector would be an improvement for experiments with the MOKE too. However, in order to significantly increase the change in the MOKE a stronger THz pulse would be required.

Considering the steps above, a clear action plan can be followed. A cryostat for holding the samples already got delivered at this point in time. Its stable fixation at very limited space would be the next step. To design a cryostat around the LN crystal is the most challenging part in the improvement plan. No significant losses can be tolerated in the in- and out-coupling process of the pulses. However, the cryostat would increase the chance to successfully perform an experiment with the THz pulse as a pump.

Appendix A

Fundamental 800 nm laser beam

A.1 800 nm laser beam cut

To characterize the main 800 nm beam coming from the amplifier, a leakage from the beam was cut with a knife edge and the power recorded. In figures A.1 and A.2 the profiles in horizontal and vertical direction can be seen, respectively. The FWHM is approximately 6.4 mm.
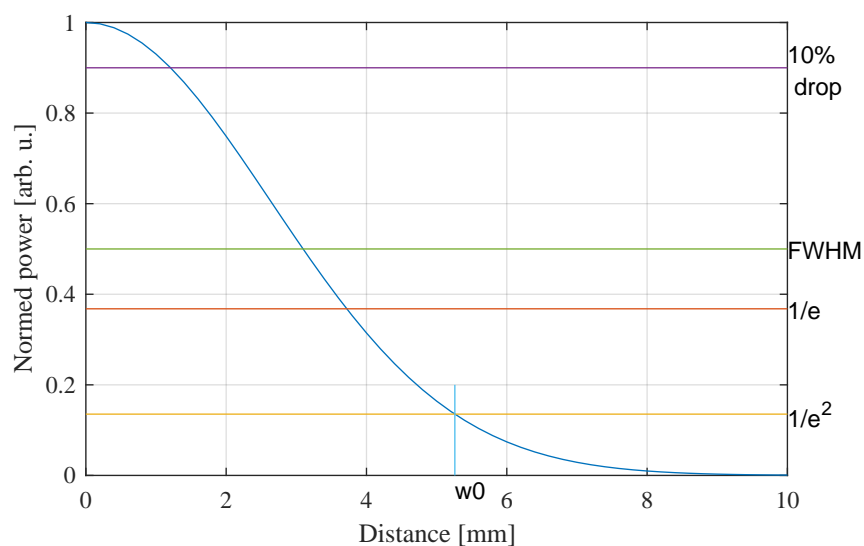
FIGURE A.1: Cut through the horizontal part of the 800 nm beam. The blue line shows the power profile. Horizontal lines show the power drop at distinct values.
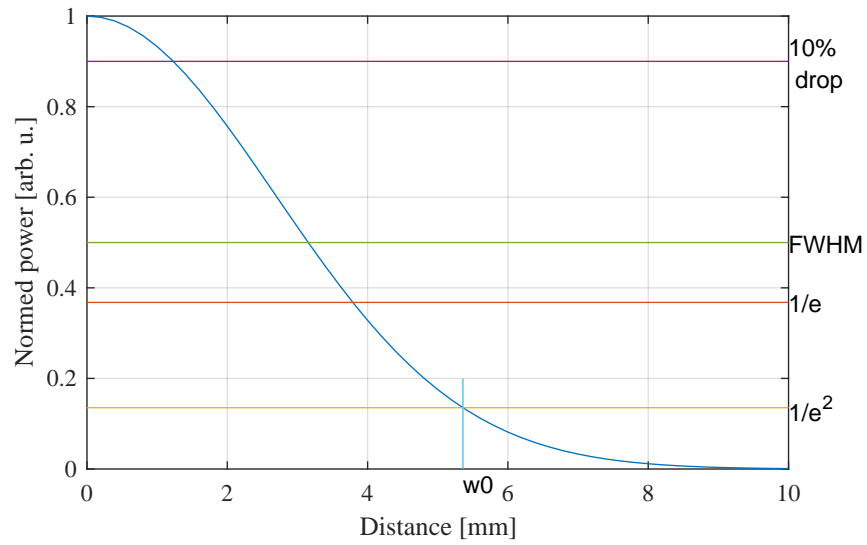
FIGURE A.2: Cut through the vertical part of the 800 nm beam. The blue line shows the power profile. Horizontal lines show the power drop at distinct values.

Appendix B

THz beam alignment

B.1 Aligning the THz beam

If the 800 nm beam is adapted with telescopes and a grating, the first step is to position the LN crystal in a correct way for maximum THz generation. For that, the 800 nm beam should hit the crystal in one of the its outer edges. As a result, the THz radiation has to travel as little as possible through the LN crystal, since the generated higher frequencies (above 1 THz) in the THz region are getting reabsorbed (cooling reduces this effect). Afterwards, two irises and a pyrodetector can be used for adjusting the crystal position in a way, that the outgoing THz is being radiated perpendicular to the output surface, as shown in figure B.1.
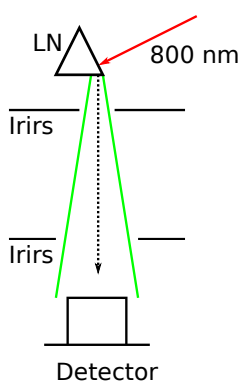
FIGURE B.1: Positioning LN crystal with two irises and a detector.

Having done this, a small 1/2 inch off-axis parabolic mirror can be placed at a distance at which the horizontal and vertical divergence of the THz beam are equal. After this, the mirror must be adjusted in a way that the THz radiation deviation is $90°$. Again, two irises and a pyrodetector can be used for that (see figure B.2).
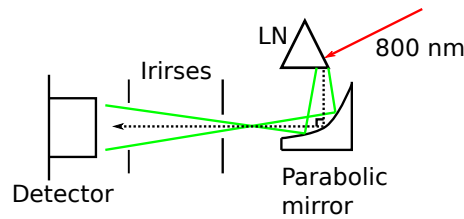
FIGURE B.2: Positioning first parabolic mirror with two irises and a
detector.

These two irises stay in place, so that an alignment laser, for instance a HeNe
laser, can be adjusted onto them. The beam can be inserted into the THz beam path
with a folding mirror, positioned between the first parabolic mirror and the first iris.
The alignment beam must have been widened beforehand to a diameter of more
than 25 mm (better is to have 30 or 40 mm for larger illuminance of the 2" mirrors).
With a lens (f=+50 mm) placed in the beam path of the HeNe, the divergence of
THz beam can be emphasised. This alignment beam placed upon the THz beam can
be used for prealigning the four off-axis parabolic mirrors and one can check if the
following two foci points are well situated (sample and EOS crystal position). Addi-
tionally, the collimation can be verified.
Afterwards the THz beam is lead onto the off-axis parabolic mirrors. At the focus
position, where the sample position is, a pyrocam[1] can be placed for seeing if astig-
matism is occurring and if the beam is approximately centered. The same can be
done at the last focus position (EOS crystal position).

B.2 Angles of the grating

In figure 2.5 the angles for positioning the grating are specified.
For repositioning the grating (after cleaning it for example), send back the beam as if
the grating would be a mirror, onto the incoming beam and align it onto each other.
Rotate the grating afterwards.

B.3 THz setup with grid

Figure B.3 shows the THz setup with the breadboard grid.

---

[1]Here the Pyrocam III from Ophir Photonics was used.
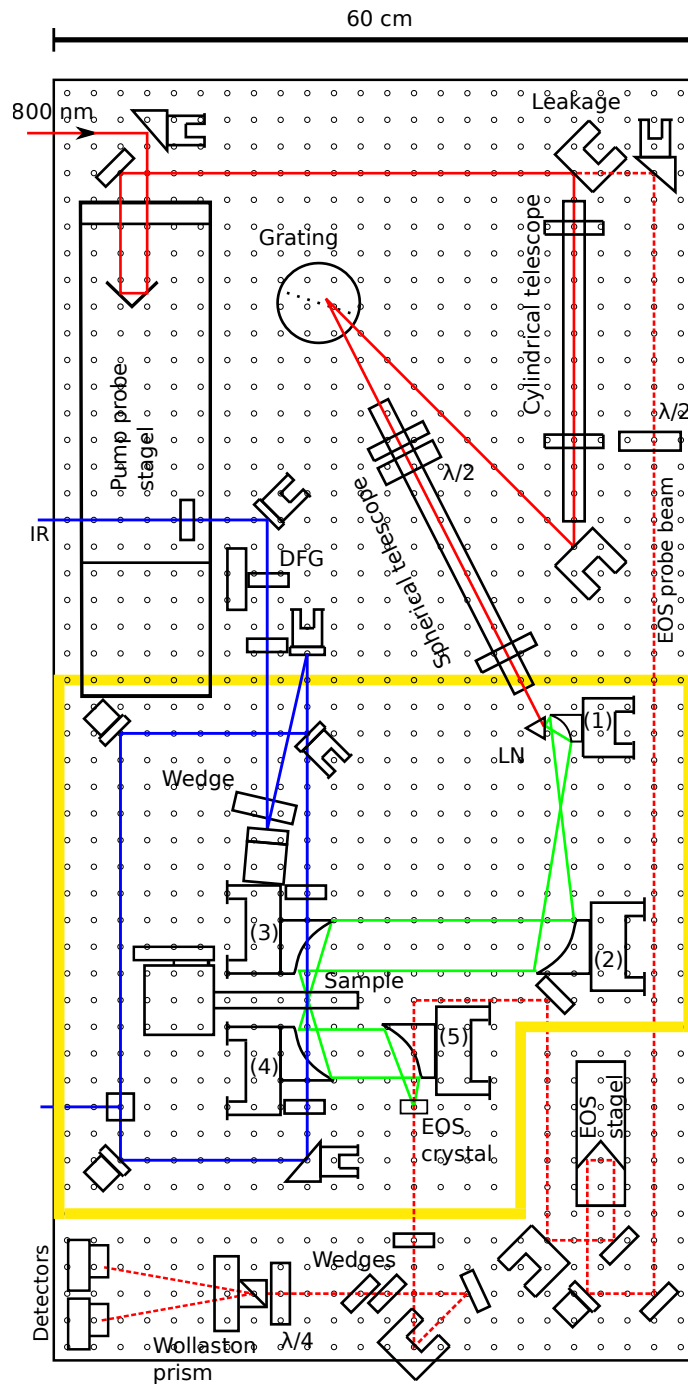
FIGURE B.3: THz setup sketch with the breadboard grid.

Appendix C

List of materials

In the tables underneath, relevant purchased articles for the THz setup are listed.

TABLE C.1: Crystals used in the THz setup

Description	Company	Order no.
GaP, Wafer, undoped(110), 5x5x0.3mm	University Wafer Inc.	
GaP (110) crystal for Thz application	Altechna Co. Ltd.	
5x5x0.3 mm, mounted in 1.,7 mm		
ZnTe (110). 5x5x1 mm, (001) axis is randomly		
oriented in polished planes, Surface		
S1:AR@800nm, S2:uncoated		

TABLE C.2: Detection electronics

Description	Company	Order no.
Si Switchable Gain Detector	Thorlabs	PDA36A-EC
A/D converter	PLUG-IN Electronic GmbH	USB-1608FS-PLUS

Table C.3: Optomechanics

Description	Company	Order no.
Wollaston Prism, 20° Beam Separation	Thorlabs	WP10-B
High-Precision Rotation Mount	Thorlabs	PRM1/M
Strahlteiler Quarzglas plan/plan	Layertec GmbH	108209
Telescope 2:1 before grid		
N-BK7 Plano-Convex Lens, 2", f = 150.0 mm	Thorlabs	LA1417-B
N-BK7 Plano-Convex Lens, 2", f = 75.0 mm	Thorlabs	LA1145-B
Telescope after grid.		
Only mounted can be purchased now		
f = 300 mm, 1", N-BK7	Thorlabs	LJ1558RM-B
Mounted Plano-Convex Round Cyl Lens		
f=-150 mm, 1", N-BK7	Thorlbs	LK1419RM-B
Mounted Plano-Concave Round Cyl Lens		
Compact Dovetail Linear Stage,	Newport	M-DS25-XYZ
6.3 mm XY, 3.0 mm Z, 25 x 25 x 49 mm,	Spectra-Physics GmbH	
Metric, for positioning the LN crystal		
Compact Dovetail XY Linear Stage, 6,3mm	Newport	M-DS25-XY
	Spectra-Physics GmbH	
Piezo Motor Linear Stage,	Newport	MFA-PPD
Direct Encoder, Integrated Controller	Spectra-Physics GmbH	
High Performance ILS Linear Stage	Newport	ILS150CC
150 mm Travel, DC Motor	Spectra-Physics GmbH	
Grid+Mount		
Diffraction Grating Mount	Newport	DGM-1
	Spectra-Physics GmbH	
Grating, 2000 lines/mm	Spectrogon	
PC 2000 25x25x6 mm NIR		
Parabolic mirrors		
1/2" 90° Off-Axis Parabolic Mirror,	Thorlabs	MPD127075
Prot.Gold, RFL = 15 mm		-90-M01
50.8 x 95.3 mm 90° Parabolspiegel Gold	Edmund Optics GmbH	#84-633
50.8 x 25.4 mm 90° Parabolspiegel Gold	Edmund Optics GmbH	#84-628

TABLE C.4: Purchased chemicals

Description	Company	Order no.
Polytetrafluoroethylene – Powder PTFE, Mean Particle size:6-9micron 200g	Goodfellow GmbH	531-672-48
a-Lactose monohydrate BioXtra, >-99%	Sigma-Aldrich Chemie GmbH	L8783-1KG
Polyethylene	Sigma-Aldrich Chemie GmbH	434272-100G

TABLE C.5: Additional parts

Description	Company	Order no.
Spülgasgenerator CO2-PG28 CO2 Absorber und Trockner für max. 32 Nl/min. bei 8,6 bar Eingangsdruck. Inkl. Eingangs- u. Ausgangsfilter	Rainer Lammertz	CO2-PG28
Scientific Grade Optical Breadboard 600x1200x59mm, M6 holes	Newport Spectra-Physics GmbH	M-SG-24-2
Laser Safety Curtain SHELTERNG	Laservision GmbH	BC1.F1P01.1999

Appendix D

Carbon based materials

D.1 Normalized raw data

Below, the normed data of the decay traces at the three different pump wavelengths can be seen. In the figures D.1, the data at 800 nm pump wavelength is shown. The normed decay at 2 μm pump wavelength is shown in the figures D.2 and the data for 3 μm pump wavelength is shown in the next section.

(A) (B)
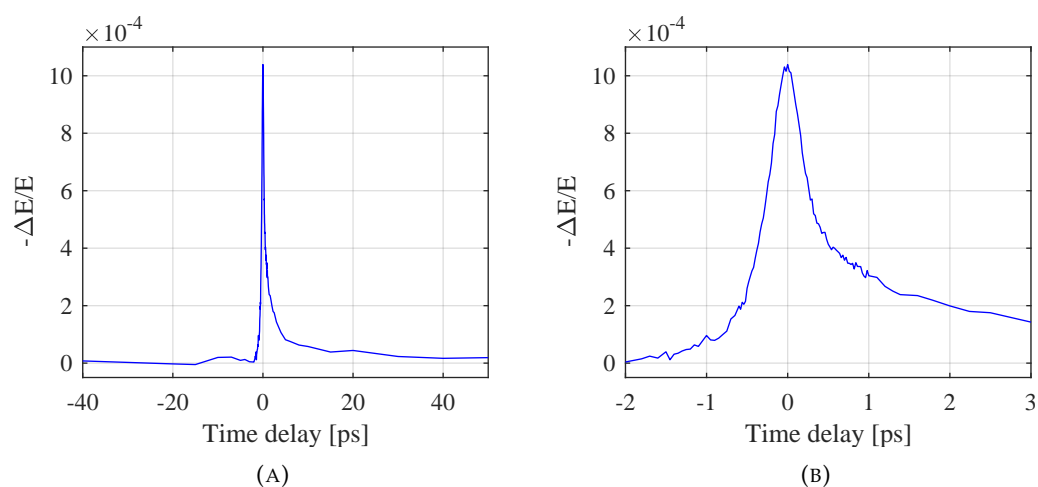
FIGURE D.1: Figure (A) shows the decay curve for GO pumped at 800 nm and probed with THz. In (B) a zoom around the maximum is done. (Normed data)
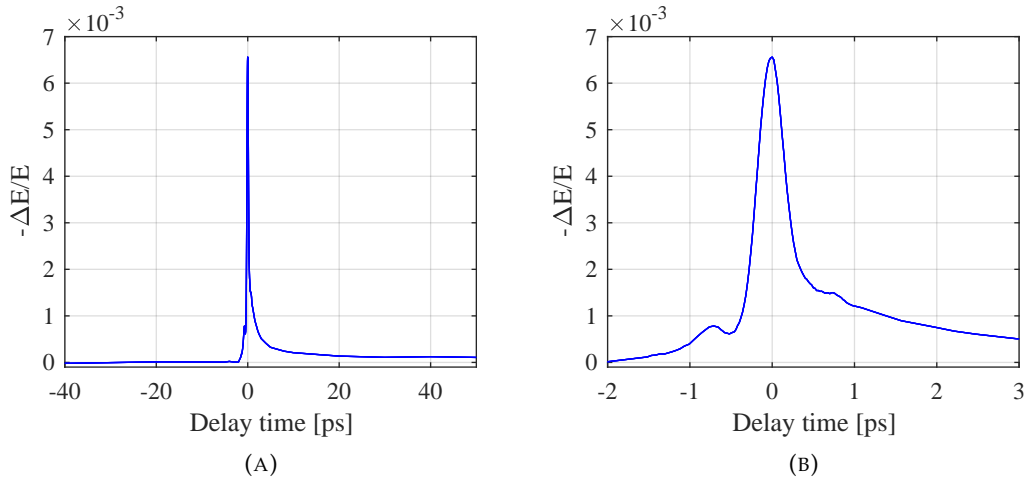
FIGURE D.2: (A) shows the decay curve for GO pumped at 2 μm and probed with THz. In (B) a zoom around the maximum is done and at -700 fs and +700 fs, embossments can be seen. (Normed data)

D.2   3 μm pump data

In the figures of D.3 the measurements of 3 different days and their average (in black) can be seen. The single measurements show strong noise on the whole time range. Also, at long positive time delays the data scatters around the zero value. On the different days the ΔE peak does not have the same height, because of the different energies given out by the OPA for the pump pulses, depending on the laser output which varied on each day. The peak height is clearly depending on the pump energy. For the single days, the fluence was:

25. ->47 $\mu J/cm^2$,

27. ->52 $\mu J/cm^2$,

28. ->53 $\mu J/cm^2$.

It is comparable to the fluence at the pump wavelength of 2 μm because here, the spot size was reduced to $\sim$0.7 mm (10-90 cut diameter).
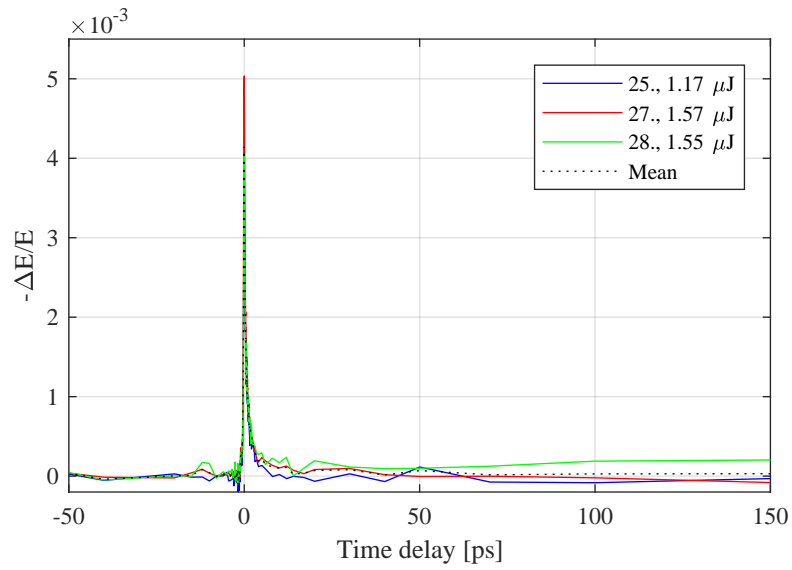
(A)
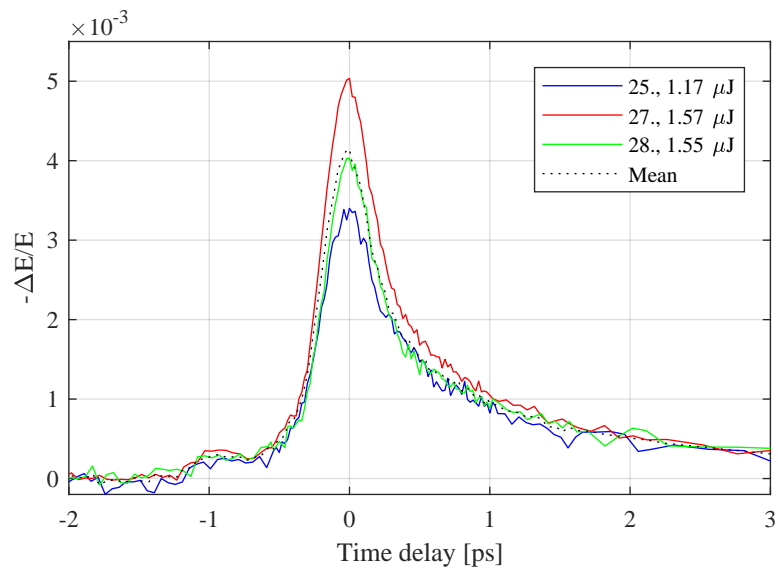
(B)

FIGURE D.3: In (A) the whole time trace of 3 measurement days are shown. The pump was 3 µm and the probe THz radiation. The black curve shows the average. (B) shows a zoom around the maximum. The legend shows the day of measurement and the energy of the pump pulse.

Appendix E

Lactose

E.1 Lactose pellets with PTFE

Lactore plus PTFE pellets were produced with different mass values and their absorbance is shown in figure E.1. In blue is a reference PTFE pellet and the red and green curves show the background measurements of the device. For the lactose curves, the PTFE background was not subtracted.
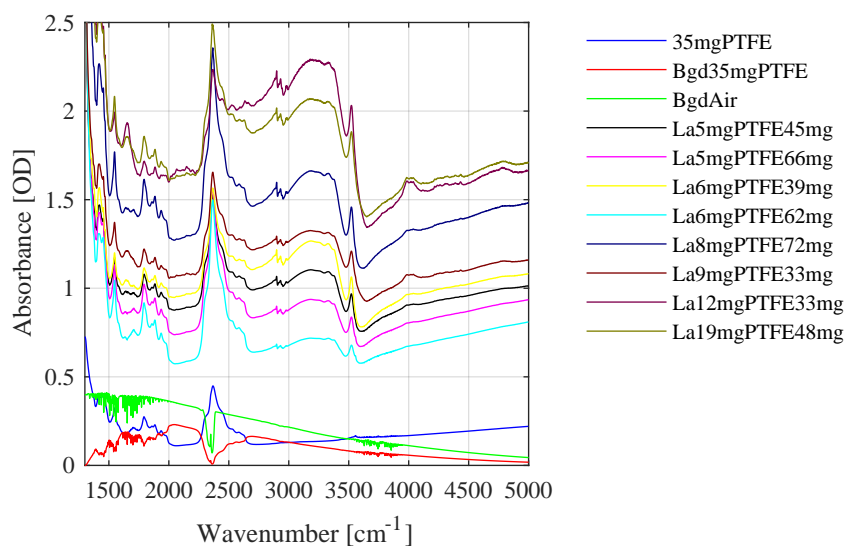
FIGURE E.1: IR spectrum of lactose plus PTFE pellets for different masses. The blue, red and green lines show reference and background measurements. The measurements were made with an FTIR spectrometer.

E.2 Growing crystals

Lactose can be grown as a single crystal which would be better to study since no complementary PTFE is needed. In order to grow the crystals, the instructions described by Jelen et al. [138] were followed.

The first step was to heat e.g. 44 g of lactose per 100 g of water to achieve dissolution. The necessary heat in our case was around 55°C, slightly above the mentioned one of 50°C. Once the lactose dissolved, the mixture turned from a milky colour to transparent. This solution was allowed to cool to room temperature. After a few days small crystals began to form at the bottom of the flask.

Since these are quite small (less than 1 mm), they need to grow further. One possibility is to put the single crystals in a supersaturated solution. But until now, the enlargement could not be achieved yet. So further testing is needed if a single crystal should be used for the pump-probe experiment.

E.3 IR pump path for lactose

Shortly before the third parabolic mirror, the IR pump beam path is shown in figure E.2. To filter out the idler and signal after the DFG crystal a longpass is used. It transmits only light above 2.5 μm. Afterwards a f=100 mm uncoated CaF$_2$ lens on a movable stage focuses the beam towards the sample. In this way a spot size of around 0.7 or 0.8 μm was achieved (measured by 10-90 cut). If the spot size should be larger (e.g. 1.4 mm), the last mirror (depicted with (1) in figure E.2) can be exchanged to a concave gold mirror (e.g. f=500 mm). The lens must removed then.

FIGURE E.2: IR pump beam path with DFG crystal, longpass and a lens for focussing.

Bibliography

[1] Justin T. Darrow et al. "Saturation Properties of Large-Aperture Photocon-ducting Antennas". In: *IEEE Journal of Quantum Electronics* 28.6 (1992), pp. 1607–1616. ISSN: 15581713. DOI: 10.1109/3.135314.
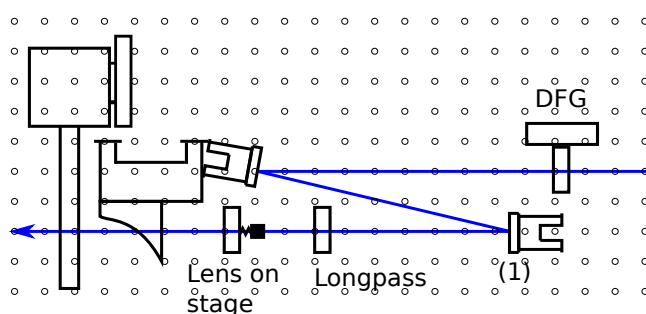
[2] X. C. Zhang et al. "Terahertz optical rectification from a nonlinear organic crystal". In: *Applied Physics Letters* 61.26 (1992), pp. 3080–3082. ISSN: 00036951. DOI: 10.1063/1.107968. URL: http://aip.scitation.org/doi/10.1063/1.107968.

[3] Benjamin Clough, Jianming Dai, and Xi Cheng Zhang. "Laser air photonics: Beyond the terahertz gap". In: *Materials Today* 15.1-2 (2012), pp. 50–58. ISSN: 13697021. DOI: 10.1016/S1369-7021(12)70020-2. URL: http://dx.doi.org/10.1016/S1369-7021(12)70020-2.

[4] János Hebling et al. "Generation of high-power terahertz pulses by tilted-pulse-front excitation and their application possibilities". In: *JOSA B* 25.7 (2008), pp. 6–19. URL: http://www.opticsinfobase.org/abstract.cfm?uri=josab-25-7-B6.

[5] Ellen H. G. Backus et al. "Probing ultrafast temperature changes of aque-ous solutions with coherent terahertz pulses." In: *Optics letters* 39.7 (2014), pp. 1717–20. ISSN: 1539-4794. URL: http://www.ncbi.nlm.nih.gov/pubmed/24686587.

[6] L. Xu, X.-C. Zhang, and D. H. Auston. "Terahertz beam generation by fem-tosecond optical pulses in electro-optic materials". In: *Applied Physics Letters* 61.15 (1992), pp. 1784–1786. ISSN: 0003-6951. DOI: 10.1063/1.108426. URL: http://aip.scitation.org/doi/10.1063/1.108426.

[7] Shin Arahira et al. "Terahertz-rate optical pulse generation from a passively mode-locked semiconductor laser diode". In: *Optics Letters* 19.11 (1994), pp. 834–836. ISSN: 0146-9592. DOI: 10.1364/OL.19.000834. URL: https://www.osapublishing.org/abstract.cfm?URI=ol-19-11-834.

[8] F. Krausz et al. "Femtosecond solid-state lasers". In: *IEEE Journal of Quantum Electronics* 28.10 (1992), pp. 2097–2122. ISSN: 0018-9197. DOI: 10.1109/3.159520. arXiv: 0504052 [physics].

[9]   Yun Shik Lee. *Principles of terahertz science and technology*. Springer Science+Business Media, LLC, 2009, pp. 1–340. ISBN: 9780387095394. DOI: 10.1007/978-0-387-09540-0.

[10]   Hamed Baghban Ali Rostani, Hassan Rasooli. *Terahertz Technology Fundamentals and Applications*. Springer-Verlag Berlin Heidelberg, 2011. ISBN: 9783642119866.

[11]   Nikola Stojanovic and Markus Drescher. "Accelerator- and laser-based sources of high-field terahertz pulses". In: *Journal of Physics B: Atomic, Molecular and Optical Physics* 46.19 (2013), p. 192001. ISSN: 0953-4075. DOI: 10.1088/0953-4075/46/19/192001. URL: http://stacks.iop.org/0953-4075/46/i=19/a=192001?key=crossref.1beee4e3515cff6b006accf633341b33.

[12]   A Oppelt et al. "DESIGN CONSIDERATIONS FOR A THz PUMP SOURCE AT THE SWISSFEL". In: *Proceedings of FEL2009*. Liverpool, 2009, pp. 161–164.

[13]   Mira Naftaly and Robert E. Miles. "Terahertz time-domain spectroscopy for material characterization". In: *Proceedings of the IEEE* 95.8 (2007), pp. 1658–1665. ISSN: 00189219. DOI: 10.1109/JPROC.2007.898835.

[14]   Michael C Kemp et al. "Security applications of terahertz technology". In: *Proceedings of SPIE*. Vol. 5070. Terahertz for Military and Security Applications. 2003, p. 44. ISBN: 9788578110796. DOI: 10.1117/12.500491. arXiv: arXiv:1011.1669v3.

[15]   J B Pendry et al. "Magnetism from conductors and enhanced nonlinear phenomena". In: *IEEE Transactions on Microwave Theory and Techniques* 47.11 (1999), pp. 2075–2084. ISSN: 0018-9480. DOI: 10.1109/22.798002.

[16]   Markus Walther et al. "Terahertz metamaterials fabricated by inkjet printing". In: *Applied Physics Letters* 95.25 (2009), p. 251107. DOI: 10.1063/1.3276544. URL: http://link.aip.org/link/?APL/95/251107/1.

[17]   Hannes Merbold et al. "THz Switching and THz Nonlinear Spectroscopy Applications". In: *CHIMIA International Journal for Chemistry* 65.5 (2011), pp. 316–319. ISSN: 00094293. DOI: 10.2533/chimia.2011.316.

[18]   S J Park et al. "Detection of microorganisms using terahertz metamaterials." In: *Scientific reports* 4 (2014), p. 4988. ISSN: 2045-2322. DOI: 10.1038/srep04988.

[19]   Michael Theuer et al. "Terahertz time-domain spectroscopy of gases, liquids, and solids." In: *Chemphyschem : a European journal of chemical physics and physical chemistry* 12.15 (2011), pp. 2695–705. ISSN: 1439-7641. DOI: 10.1002/cphc.201100158. URL: http://www.ncbi.nlm.nih.gov/pubmed/21735510.

[20] B Fischer et al. "Chemical recognition in terahertz time-domain spectroscopy and imaging". In: *Semiconductor Science and Technology* 20.7 (2005), S246–S253. ISSN: 0268-1242. DOI: 10.1088/0268-1242/20/7/015.

[21] Ruth M Woodward et al. "Terahertz pulse imaging in reflection geometry of human skin cancer and skin tissue". In: *Physics in Medicine and Biology* 47.21 (2002), pp. 3853–3863. ISSN: 0031-9155. DOI: 10.1088/0031-9155/47/21/325. URL: http://stacks.iop.org/0031-9155/47/i=21/a=325?key=crossref.ee5adcbc8d6ef833bb46aa6cbd0a050e.

[22] Alex Ortner, Andreas Bitzer, and Markus Walther. "Terahertz near-field microscopy with subwavelength spatial resolution based on photoconductive antennas". In: *Applied Optics* 49.19 (2010), E1–E6. ISSN: 2155-3165. DOI: 10.1364/AO.49.0000E1. URL: https://www.osapublishing.org/ao/abstract.cfm?uri=ao-49-19-e1.

[23] C. Jördens et al. "Evaluation of leaf water status by means of permittivity at terahertz frequencies". In: *Journal of Biological Physics* 35.3 (2009), pp. 255–264. ISSN: 0092-0606. DOI: 10.1007/s10867-009-9161-0. URL: http://link.springer.com/10.1007/s10867-009-9161-0.

[24] Ian F. Akyildiz, Josep Miquel Jornet, and Chong Han. "Terahertz band: Next frontier for wireless communications". In: *Physical Communication* 12 (2014), pp. 16–32. ISSN: 18744907. DOI: 10.1016/j.phycom.2014.01.006. URL: http://www.sciencedirect.com/science/article/pii/S1874490714000238.

[25] Gilad Haran et al. "Femtosecond far-infrared pump-probe spectroscopy: A new tool for studying low-frequency vibrational dynamics in molecular condensed phases". In: *Chemical Physics Letters* 274.4 (1997), pp. 365–371. DOI: 10.1016/S0009-2614(97)00705-7. URL: http://www.sciencedirect.com/science/article/pii/S0009261497007057.

[26] F. A. Hegmann et al. "Picosecond Transient Photoconductivity in Functionalized Pentacene Molecular Crystals Probed by Terahertz Pulse Spectroscopy". In: *Physical Review Letters* 89.22 (2002), p. 227403. ISSN: 0031-9007. DOI: 10.1103/PhysRevLett.89.227403. URL: https://link.aps.org/doi/10.1103/PhysRevLett.89.227403.

[27] B. I. Greene et al. "Picosecond pump and probe spectroscopy utilizing freely propagating terahertz radiation". In: *Optics Letters* 16.1 (1991), pp. 48–49. ISSN: 0146-9592. DOI: 10.1364/OL.16.000048. URL: https://www.osapublishing.org/abstract.cfm?URI=ol-16-1-48.

[28]   Michael Schall and Peter Uhd Jepsen. "Photoexcited GaAs surfaces stud-
       ied by transient terahertz time-domain spectroscopy". In: *Optics Letters* 25.1
       (2000), pp. 13–15. ISSN: 0146-9592. DOI: `10.1364/OL.25.000013`. URL: `https:
       //www.osapublishing.org/abstract.cfm?URI=ol-25-1-13`.

[29]   Wolfgang Demtröder. *Laserspektroskopie 1*. 6th. Springer, 2011. ISBN: 978-3-
       642-21305-2. DOI: `10.1007/978-3-642-21306-9`.

[30]   *Spitfire Ace, Ultrafast Amplifier, User'sManual*. 90048324. Spectra-Physics, 2011.

[31]   Bahaa E. A. Saleh and Malvin C. Teich. *Fundamentals of Photonics*. 2nd ed. Wi-
       ley Series in Pure and Applied Optics. Wiley, 2007, p. 1200. ISBN: 9780471358329.
       URL: `http://books.google.de/books?id=Ve8eAQAAIAAJ`.

[32]   R. W. Boyd. *Nonlinear Optics*. 3rd. Academic Press, 2008, p. 640. ISBN: 978-0-
       12-369470-6.

[33]   Shu-Wei Huang et al. "High conversion efficiency, high energy terahertz pulses
       by optical rectification in cryogenically cooled lithium niobate". In: *Optics Let-
       ters* 38.5 (2013), pp. 796–798. ISSN: 0146-9592. DOI: `10.1364/OL.38.000796`.
       URL: `https://www.osapublishing.org/abstract.cfm?URI=ol-38-5-796`.

[34]   C Kittel. *Einführung in die Festkörperphysik*. 10th ed. Oldenbourg, 1993. ISBN:
       9783486577235.

[35]   Sen-Cheng Zhong et al. "Optimization of terahertz generation from LiNbO_3
       under intense laser excitation with the effect of three-photon absorption". In:
       Optics Express 23.24 (2015), pp. 31313–31323. ISSN: 1094-4087. DOI: `10.1364/
       OE.23.031313`.

[36]   Koustuban Ravi et al. "Theory of terahertz generation by optical rectification
       using tilted-pulse-fronts". In: *Optics Express* 23.4 (2015), pp. 5253–5276. ISSN:
       1094-4087. DOI: `10.1364/OE.23.005253`. URL: `https://www.osapublishing.
       org/abstract.cfm?URI=oe-23-4-5253`.

[37]   Masaru Nakamura et al. "Optical damage resistance and refractive indices
       in near-stoichiometric MgO-doped LiNbO3". In: *Japanese Journal of Applied
       Physics* 41.1 A/B (2002), pp. L 49–L 51. ISSN: 00214922. DOI: `10.1143/JJAP.
       41.L49`.

[38]   L. Pálfalvi et al. "Temperature dependence of the absorption and refraction
       of Mg-doped congruent and stoichiometric LiNbO 3 in the THz range". In:
       Journal of Applied Physics 97.12 (2005), p. 123505. ISSN: 00218979. DOI: `10.
       1063/1.1929859`. URL: `http://aip.scitation.org/doi/10.1063/1.
       1929859`.

[39] J Hebling et al. "Tunable THz pulse generation by optical rectification of ultrashort laser pulses with tilted pulse fronts". In: *Applied Physics B: Lasers and Optics* 78.5 (2004), pp. 593–599. ISSN: 09462171. DOI: 10.1007/s00340-004-1469-7.

[40] Susan L. Dexheimer, ed. *Terahertz spectroscopy: principles and applications*. 1st ed. Boca Raton, Fla.: CRC Press, 2007, p. 331. ISBN: 978-0-8493-7525-5.

[41] M Dressel and G Grüner. *Electrodynamics of Solids: Optical Properties of Electrons in Matter*. 1st ed. Cambridge University Press, 2002, p. 474. ISBN: 9780521597265.

[42] Saima Ahmed et al. "Detectivity enhancement in THz electrooptical sampling". In: *Review of Scientific Instruments* 85.1 (2014). ISSN: 00346748. DOI: 10.1063/1.4862657.

[43] X. Xin et al. "Terahertz absorption spectrum of para and ortho water vapors at different humidities at room temperature". In: *Journal of Applied Physics* 100.9 (2006), pp. 1–5. ISSN: 00218979. DOI: 10.1063/1.2357412.

[44] Xi-Cheng Zhang and Jingzhou Xu. *Introduction to THz Wave Photonics*. Springer Science+Business Media, LLC, 2010. ISBN: 978-1-4419-0977-0. DOI: 10.1007/978-1-4419-0978-7.

[45] Abdul J. Jerri. "The Shannon Sampling Theorem—Its Various Extensions and Applications: A Tutorial Review". In: *Proceedings of the IEEE* 65.11 (1977), pp. 1565–1596. ISSN: 15582256. DOI: 10.1109/PROC.1977.10771. URL: http://ieeexplore.ieee.org/document/1455040/.

[46] Martin van Exter, C. Fattinger, and D. Grischkowsky. "Terahertz time-domain spectroscopy of water vapor". In: *Optics Letters* 14.20 (1989), pp. 1128–1130. ISSN: 0146-9592. DOI: 10.1364/OL.14.001128. URL: https://www.osapublishing.org/abstract.cfm?URI=ol-14-20-1128.

[47] Richard T. Hall, Dale Vrabec, and Jerome M. Dowling. "A High-Resolution, Far Infrared Double-Beam Lamellar Grating Interferometer". In: *Applied Optics* 5.7 (1966), pp. 1147–1158. ISSN: 0003-6935. DOI: 10.1364/AO.5.001147.

[48] Richard T Hall and Jerome M Dowling. "Pure Rotational Spectrum of Water Vapor". In: *J. Chem. Phys.* 47.7 (1967), pp. 2454–2461. ISSN: 00219606. DOI: 10.1063/1.1703330.

[49] Andrei G. Stepanov, János Hebling, and Jürgen Kuhl. "Efficient generation of subpicosecond terahertz radiation by phase-matched optical rectification using ultrashort laser pulses with tilted pulse fronts". In: *Applied Physics Letters* 83.15 (2003), pp. 3000–3002. ISSN: 00036951. DOI: 10.1063/1.1617371.

[50]   H. Hirori et al. "Single-cycle terahertz pulses with amplitudes exceeding 1 MV/cm generated by optical rectification in LiNbO3". In: *Applied Physics Letters* 98.9 (2011), p. 091106. ISSN: 00036951. DOI: 10.1063/1.3560062.

[51]   Wolfgang Demtröder. *Experimentalphysik 2*. 6th ed. Springer-Verlag Berlin Heidelberg, 2013. ISBN: 978-3-642-29943-8. DOI: 10.1007/978-3-642-29944-5.

[52]   Deep Jariwala et al. "Carbon nanomaterials for electronics, optoelectronics, photovoltaics, and sensing". In: *Chem. Soc. Rev.* 42.7 (2013), pp. 2824–2860. ISSN: 0306-0012. DOI: 10.1039/C2CS35335K.

[53]   A. Srivastava et al. "Carbon nanotube filters". In: *Nature Materials* 3.9 (2004), pp. 610–614. ISSN: 14761122. DOI: 10.1038/nmat1192. URL: http://www.nature.com/doifinder/10.1038/nmat1192.

[54]   Ritwik Kumar Roy and Kwang-Ryeol Lee. "Biomedical applications of diamond-like carbon coatings: A review". In: *Journal of Biomedical Materials Research Part B: Applied Biomaterials* 83B.1 (2007), pp. 72–84. ISSN: 15524973. DOI: 10.1002/jbm.b.30768. URL: http://doi.wiley.com/10.1002/jbm.b.30768.

[55]   Hua Bai, Chun Li, and Gaoquan Shi. "Functional composite materials based on chemically converted graphene". In: *Advanced Materials* 23.9 (2011), pp. 1089–1115. ISSN: 09359648. DOI: 10.1002/adma.201003753.

[56]   K. S. Novoselov et al. "Electric field in atomically thin carbon films". In: *Science* 306.5696 (2004), pp. 666–669. ISSN: 00368075. DOI: 10.1126/science.1102896. arXiv: 0410550 [cond-mat]. URL: http://www.ncbi.nlm.nih.gov/pubmed/15499015.

[57]   T Enoki. *Physics and Chemistry of Graphene: Graphene to Nanographene*. World Scientific Publishing Limited, 2012. ISBN: 9789814241489.

[58]   A. K. Geim and K. S. Novoselov. "The rise of graphene". In: *Nature materials* 6.3 (2007), pp. 183–191. ISSN: 1476-1122. DOI: 10.1038/nmat1849. URL: http://www.ncbi.nlm.nih.gov/pubmed/17330084.

[59]   Uichiro Mizutani. *Introduction to the Electron Theory of Metals*. Cambridge: Cambridge University Press, 2001. ISBN: 9780511612626. DOI: 10.1017/CBO9780511612626.

[60]   J. Wintterlin and M.-L. Bocquet. "Graphene on metal surfaces". In: *Surface Science* 603.10–12 (2009), pp. 1841–1852. ISSN: 0039-6028. DOI: http://dx.doi.org/10.1016/j.susc.2008.08.037.

[61]   K. S. Novoselov. "Nobel Lecture: Graphene: Materials in the Flatland". In: *Reviews of Modern Physics* 83.3 (2011), pp. 837–849. ISSN: 00346861. DOI: 10.1103/RevModPhys.83.837. URL: https://link.aps.org/doi/10.1103/RevModPhys.83.837.

[62] Dmitry V Kosynkin et al. "Longitudinal unzipping of carbon nanotubes to form graphene nanoribbons". In: *Nature* 458.7240 (2009), pp. 872–876. ISSN: 0028-0836. DOI: 10.1038/nature07872. URL: http://dx.doi.org/10.1038/nature07872.

[63] Songfeng Pei and Hui-Ming Cheng. "The reduction of graphene oxide". In: *Carbon* 50.9 (2012), pp. 3210–3228. ISSN: 0008-6223. DOI: http://dx.doi.org/10.1016/j.carbon.2011.11.010. URL: http://www.sciencedirect.com/science/article/pii/S0008622311008967.

[64] Shun Mao, Haihui Pu, and Junhong Chen. "Graphene oxide and its reduction: modeling and experimental progress". In: *RSC Adv.* 2.7 (2012), pp. 2643–2662. DOI: 10.1039/C2RA00663D. URL: http://dx.doi.org/10.1039/C2RA00663D.

[65] Zhiting Liu et al. "Controlling and formation mechanism of oxygen-containing groups on graphite oxide". In: *Industrial and Engineering Chemistry Research* 53.1 (2014), pp. 253–258. ISSN: 08885885. DOI: 10.1021/ie403088t. URL: https://pubs.acs.org/doi/pdf/10.1021/ie403088t.

[66] F. Tuinstra and J. L. Koenig. "Raman Spectrum of Graphite". In: *The Journal of Chemical Physics* 53.3 (1970), pp. 1126–1130. ISSN: 0021-9606. DOI: 10.1063/1.1674108. arXiv: arXiv:1011.1669v3. URL: http://aip.scitation.org/doi/10.1063/1.1674108.

[67] Nina I. Kovtyukhova et al. "Layer-by-layer assembly of ultrathin composite films from micron-sized graphite oxide sheets and polycations". In: *Chemistry of Materials* 11.3 (1999), pp. 771–778. ISSN: 08974756. DOI: 10.1021/cm981085u. URL: https://pubs.acs.org/doi/abs/10.1021/cm981085u.

[68] Konstantin N. Kudin et al. "Raman spectra of graphite oxide and functionalized graphene sheets". In: *Nano Letters* 8.1 (2008), pp. 36–41. ISSN: 15306984. DOI: 10.1021/nl071822y. URL: https://pubs.acs.org/doi/abs/10.1021/nl071822y.

[69] Folke Johannes Tölle, Martin Fabritius, and Rolf Mülhaupt. "Emulsifier-Free Graphene Dispersions with High Graphene Content for Printed Electronics and Freestanding Graphene Films". In: *Advanced Functional Materials* 22.6 (2012), pp. 1136–1144. ISSN: 1616301X. DOI: 10.1002/adfm.201102888. URL: http://doi.wiley.com/10.1002/adfm.201102888.

[70] K. K.H. De Silva et al. *Chemical reduction of graphene oxide using green reductants*. 2017. DOI: 10.1016/j.carbon.2017.04.025.

[71]   William S. Hummers and Richard E. Offeman. "Preparation of Graphitic Oxide". In: *Journal of the American Chemical Society* 80.6 (1958), pp. 1339–1339. ISSN: 0002-7863. DOI: 10.1021/ja01539a017. URL: http://pubs.acs.org/doi/abs/10.1021/ja01539a017.

[72]   I Miccoli et al. "The 100th anniversary of the four-point probe technique: The role of probe geometries in isotropic and anisotropic systems". In: *Journal of Physics Condensed Matter* 27.22 (2015), p. 223201. ISSN: 1361648X. DOI: 10.1088/0953-8984/27/22/223201. URL: http://stacks.iop.org/0953-8984/27/i=22/a=223201?key=crossref.5f146e5ca8d78e9795a89548e891758e.

[73]   Hungyen Lin et al. "Contactless graphene conductivity mapping on a wide range of substrates with terahertz time-domain reflection spectroscopy". In: *Scientific Reports* 7.1 (2017), p. 10625. ISSN: 20452322. DOI: 10.1038/s41598-017-09809-7. URL: http://www.nature.com/articles/s41598-017-09809-7.

[74]   David M. A. Mackenzie et al. "Quality assessment of terahertz time-domain spectroscopy transmission and reflection modes for graphene conductivity mapping". In: *Optics Express* 26.7 (2018), pp. 9220–9229. ISSN: 1094-4087. DOI: 10.1364/OE.26.009220. URL: https://www.osapublishing.org/abstract.cfm?URI=oe-26-7-9220.

[75]   Paul a George et al. "Ultrafast Optical-Pump Terahertz-Probe Spectroscopy of the Carrier Relaxation Epitaxial Graphene". In: *Nano letters* 8.12 (2008), pp. 4248–4251. ISSN: 1530-6984. DOI: 10.102/nl8019399. arXiv: 0805.4647.

[76]   M Tinkham. "Energy Gap Interpretation of Experiments on Infrared Transmission through Superconducting Films". In: *Phys. Rev.* 104.3 (1956), pp. 845–846. DOI: 10.1103/PhysRev.104.845. URL: http://link.aps.org/doi/10.1103/PhysRev.104.845.

[77]   Jahan M. Dawlaty et al. "Measurement of ultrafast carrier dynamics in epitaxial graphene". In: *Applied Physics Letters* 92.4 (2008), pp. 16–19. ISSN: 00036951. DOI: 10.1063/1.2837539. arXiv: 0712.0119v1.

[78]   Sreejith Kaniyankandy et al. "Ultrafast relaxation dynamics in graphene oxide: Evidence of electron trapping". In: *Journal of Physical Chemistry C* 115.39 (2011), pp. 19110–19116. ISSN: 19327447. DOI: 10.1021/jp206923q.

[79]   Srabani Kar et al. "Time resolved terahertz spectroscopy of low frequency electronic resonances and optical pump-induced terahertz photoconductivity in reduced graphene oxide membrane". In: *Carbon* 80.1 (2014), pp. 762–770. ISSN: 00086223. DOI: 10.1016/j.carbon.2014.09.030. arXiv: 1407.2752. URL: http://dx.doi.org/10.1016/j.carbon.2014.09.030.

[80] Momchil T Mihnev et al. "Microscopic origins of the terahertz carrier relaxation and cooling dynamics in graphene." In: *Nature communications* 7.11617 (2016). DOI: 10.1038/ncomms11617.

[81] Y Ishida et al. "Non-thermal hot electrons ultrafastly generating hot optical phonons in graphite". In: *Scientific reports* 1 (2011), p. 64. DOI: 10.1038/srep00064. arXiv: 1108.4567. URL: http://www.nature.com/srep/2011/110819/srep00064/full/srep00064.html.

[82] Matthew C. Beard, Gordon M. Turner, and Charles A. Schmuttenmaer. *Terahertz spectroscopy*. 2002. DOI: 10.1021/jp020579i. URL: https://pubs.acs.org/doi/abs/10.1021/jp020579i.

[83] Michael Schall et al. "Subpicosecond time-resolved terahertz time-domain spectroscopy of transient carrier dynamics in semiconductors". In: *SPIE/EOS International Symposium on Terahertz Radiation* (1999), pp. 220–227. ISSN: 0277-786X. DOI: 10.1117/12.361038. URL: http://proceedings.spiedigitallibrary.org/proceeding.aspx?doi=10.1117/12.361038.

[84] Srabani Kar et al. "Tuning photoinduced terahertz conductivity in monolayer graphene: Optical-pump terahertz-probe spectroscopy". In: *Physical Review B - Condensed Matter and Materials Physics* 90.16 (2014), pp. 1–9. ISSN: 1550235X. DOI: 10.1103/PhysRevB.90.165420. arXiv: 1407.2752.

[85] R. Kohlrausch. "Theorie des elektrischen Rückstandes in der Leidener Flasche". In: *Annalen der Physik und Chemie* 167.2 (1854), pp. 179–214. ISSN: 00033804. DOI: 10.1002/andp.18541670203. URL: http://doi.wiley.com/10.1002/andp.18541670203.

[86] M. Cardona, R.V. Chamberlin, and W. Marx. "The history of the stretched exponential function". In: *Annalen der Physik* 16.12 (2007), pp. 842–845. ISSN: 00033804. DOI: 10.1002/andp.200710269. URL: http://doi.wiley.com/10.1002/andp.200710269.

[87] Graham Williams and David C. Watts. "Non-symmetrical dielectric relaxation behaviour arising from a simple empirical decay function". In: *Transactions of the Faraday Society* 66.0 (1970), pp. 80–85. DOI: 10.1039/tf9706600080. URL: http://dx.doi.org/10.1039/TF9706600080.

[88] J. C. Phillips. "Stretched exponential relaxation in molecular and electronic glasses". In: *Reports on Progress in Physics* 59.9 (1996), pp. 1133–1207. ISSN: 00344885. DOI: 10.1088/0034-4885/59/9/003.

[89] D. C. Johnston. "Stretched exponential relaxation arising from a continuous sum of exponential decays". In: *Physical Review B - Condensed Matter and Materials Physics* 74.18 (2006). ISSN: 10980121. DOI: 10.1103/PhysRevB.74.184430.

[90]   M. N. Berberan-Santos, E. N. Bodunov, and B. Valeur. "Mathematical functions for the analysis of luminescence decays with underlying distributions 1. Kohlrausch decay function (stretched exponential)". In: *Chemical Physics* 315.1-2 (2005), pp. 171–182. ISSN: 03010104. DOI: 10.1016/j.chemphys.2005. 04.006.

[91]   J M Mendel. *Optimal seismic deconvolution: an estimation-based approach*. Monograph Series. Academic Press, 1983, p. 254. ISBN: 978-1483243450.

[92]   S Mukamel. *Principles of Nonlinear Optical spectroscopy*. Ed. by M. Lapp et al. Rochester, New York: Oxford University Press, 1995. ISBN: 0-19-509278-3.

[93]   Kazuyuki Fujii. "Introduction to the Rotating Wave Approximation (RWA): Two Coherent Oscillations". In: *Journal of Modern Physics* 08.12 (2017), pp. 2042– 2058. ISSN: 2153-1196. DOI: 10.4236/jmp.2017.812124. URL: http://www. scirp.org/journal/doi.aspx?DOI=10.4236/jmp.2017.812124.

[94]   Amul Shinde. "Ultrafast dynamics of graphite oxide and semiconducture saturable absorber". PhD thesis. University of Hamburg, 2018.

[95]   Hugen Yan et al. "Time-resolved Raman spectroscopy of optical phonons in graphite: Phonon anharmonic coupling and anomalous stiffening". In: *Physical Review B - Condensed Matter and Materials Physics* 80.12 (2009). ISSN: 10980121. DOI: 10.1103/PhysRevB.80.121403. arXiv: 0908.3036.

[96]   Tobias Kampfrath et al. "Strongly coupled optical phonons in the ultrafast dynamics of the electronic energy and current relaxation in graphite". In: *Physical Review Letters* 95.18 (2005), pp. 26–29. ISSN: 00319007. DOI: 10.1103/ PhysRevLett.95.187403.

[97]   D. A. Darling and A. J. F. Siegert. "The 1st passage problem for a continuous Markov Process". In: *Ann. Math. Stat.* 24.4 (1953), pp. 624–639. DOI: 10.2307/ 2236785. URL: https://www.jstor.org/stable/2236785.

[98]   Oliver Mülken. "Enhanced Quantum Transport in Multiplex Networks". In: *Journal of Statistical Physics* 162.3 (2016), pp. 644–651. ISSN: 00224715. DOI: 10.1007/s10955-015-1434-3. arXiv: 1503.01609v2. URL: http://link. springer.com/10.1007/s10955-015-1434-3.

[99]   Peter Hamm. "Coherent effects in femtosecond infrared spectroscopy". In: *Chemical Physics* 200.3 (1995), pp. 415–429. DOI: https://doi.org/10.1016/ 0301-0104(95)00262-6.

[100] Yuan Yang et al. "Reassessing Graphene Absorption and Emission Spectroscopy". In: *Nano Letters* 17.10 (2017), pp. 6077–6082. ISSN: 15306992. DOI: 10.1021/ acs.nanolett.7b02500. arXiv: 1704.07500.

[101] M. Born and R. Oppenheimer. "Zur Quantentheorie der Molekeln". In: *Annalen der Physik* 389.20 (1927), pp. 457–484. ISSN: 00033804. DOI: 10.1002/andp.19273892002. URL: http://doi.wiley.com/10.1002/andp.19273892002.

[102] N. K. Rahman and C. Guidotti. *Photons and Continuum States of Atoms and Molecules*. Ed. by N. K. Rahman, C. Guidotti, and M. Allegrini. Cortona, Italy: Springer-Verlag Berlin Heidelberg, 1986. ISBN: 13:978-3-642-71780-2. DOI: 10.1007/978-3-642-71778-9.

[103] Jichen Li and D. K. Ross. "Evidence for two kinds of hydrogen bond in ice". In: *Nature* 365.6444 (1993), pp. 327–329. ISSN: 0028-0836. DOI: 10.1038/365327a0. URL: http://www.nature.com/doifinder/10.1038/365327a0.

[104] Célia Fonseca Guerra et al. "Hydrogen Bonding in DNA Base Pairs: Reconciliation of Theory and Experiment". In: *Journal of the American Chemical Society* 122.17 (2000), pp. 4117–4128. ISSN: 0002-7863. DOI: 10.1021/ja993262d. URL: https://pubs.acs.org/doi/abs/10.1021/ja993262d.

[105] Rudolf Gross and Achim Marx. *Festkörperphysik*. 2nd ed. Walter de Gruyter GmbH, Berlin/Boston, 2014. ISBN: 978-3-11-035869-8.

[106] Thomas Steiner. "The hydrogen bond in the solid state." In: *Angew. Chem. Int. Ed.* 41.1 (2002), pp. 49–76. ISSN: 1433-7851. URL: https://doi.org/10.1002/1521-3773(20020104)41:1{\%}3C48::AID-ANIE48{\%}3E3.0.CO;2-U.

[107] A. Luzar and D. Chandler. "Effect of environment on hydrogen bond dynamics in liquid water". In: *Physical Review Letters* 76.6 (1996), pp. 928–931. ISSN: 1079-7114. DOI: 10.1103/PhysRevLett.76.928.

[108] F. N. Keutsch and R. J. Saykally. "Water clusters: Untangling the mysteries of the liquid, one molecule at a time". In: *Proceedings of the National Academy of Sciences* 98.19 (2001), pp. 10533–10540. ISSN: 0027-8424. DOI: 10.1073/pnas.191266498. URL: http://www.pnas.org/cgi/doi/10.1073/pnas.191266498.

[109] Markus Walther, Bernd M. Fischer, and P. Uhd Jepsen. "Noncovalent intermolecular forces in polycrystalline and amorphous saccharides in the far infrared". In: *Chemical Physics* 288.2-3 (2003), pp. 261–268. ISSN: 03010104. DOI: 10.1016/S0301-0104(03)00031-4. URL: http://linkinghub.elsevier.com/retrieve/pii/S0301010403000314.

[110] T. M. Korter and D. F. Plusquellic. "Continuous-wave terahertz spectroscopy of biotin: Vibrational anharmonicity in the far-infrared". In: *Chemical Physics Letters* 385.1-2 (2004), pp. 45–51. ISSN: 00092614. DOI: 10.1016/j.cplett.2003.12.060.

[111] P.L.H. McSweeney and P.F. Fox. *Advanced Dairy Chemistry*. Ed. by Paul McSweeney and Patrick F. Fox. 3rd ed. Vol. 2. New York, NY: Springer New York, 2009, p. 801. ISBN: 978-0-387-84864-8. DOI: 10.1007/978-0-387-84865-5. URL: http://link.springer.com/10.1007/978-0-387-84865-5.

[112] Jon E. Bjarnason, Elliott R. Brown, and Timothy M. Korter. "Comparison of the THz absorption feature in lactose to related saccharides". In: 6549 (2007), pp. 65490L–65490L–9. DOI: 10.1117/12.725169. URL: http://proceedings.spiedigitallibrary.org/proceeding.aspx?articleid=1338474.

[113] C. A. Beevers and H. N. Hansen. "The structure of α-lactose monohydrate". In: *Acta Crystallographica Section B Structural Crystallography and Crystal Chemistry* 27.7 (1971), pp. 1323–1325. ISSN: 0567-7408. DOI: 10.1107/S0567740871003947. URL: http://scripts.iucr.org/cgi-bin/paper?S0567740871003947.

[114] U. Heugen et al. "Solute-induced retardation of water dynamics probed directly by terahertz spectroscopy". In: *Proceedings of the National Academy of Sciences* 103.33 (2006), pp. 12301–12306. ISSN: 0027-8424. DOI: 10.1073/pnas.0604897103.

[115] M. L. Cowan et al. "Ultrafast memory loss and energy redistribution in the hydrogen bond network of liquid H2O". In: *Nature* 434.1999 (2005), pp. 199–202. DOI: 10.1038/nature03383. URL: http://dx.doi.org/10.1038/nature03383.

[116] Krupa Ramasesha et al. "Water vibrations have strongly mixed intra- and intermolecular character". In: *Nature Chemistry* 5.11 (2013), pp. 935–940. ISSN: 17554330. DOI: 10.1038/nchem.1757.

[117] B. M. Fischer, M. Walther, and P. U. Jepsen. "Far-infrared vibrational modes of DNA components studied by terahertz time-domain spectroscopy". In: *Physics in Medicine and Biology* 47.21 (2002), pp. 3807–3814. ISSN: 00319155. DOI: 10.1088/0031-9155/47/21/319. URL: http://stacks.iop.org/0031-9155/47/i=21/a=319?key=crossref.837a2a7e9f988a91e4c429d581f341bf.

[118] G. Masetti et al. "Conformational Order and Disorder in Poly(tetrafluoroethylene) from the Infrared Spectrum". In: *Macromolecules* 6.5 (1973), pp. 700–707. DOI: 10.1021/ma60035a011. URL: https://doi.org/10.1021/ma60035a011.

[119] Dwight Gray. *American Institute of Physics Handbook*. 3rd ed. McGraw-Hill, 1972, p. 2200. ISBN: 007001485X.

[120] E. R. Brown et al. "On the strong and narrow absorption signature in lactose at 0.53 THz". In: *Applied Physics Letters* 90.6 (2007), pp. 3–5. ISSN: 00036951. DOI: 10.1063/1.2437107.

[121] Shigeki Saito et al. "First principles calculation of terahertz vibrational modes of a disaccharide monohydrate crystal of lactose". In: *Japanese Journal of Applied Physics, Part 2: Letters* 45.42-45 (2006), pp. 10–13. ISSN: 00214922. DOI: `10.1143/JJAP.45.L1156`.

[122] D. G. Allis et al. "Assignment of the lowest-lying THz absorption signatures in biotin and lactose monohydrate by solid-state density functional theory". In: *Chemical Physics Letters* 440.4-6 (2007), pp. 203–209. ISSN: 00092614. DOI: `10.1016/j.cplett.2007.04.032`.

[123] M. R. Freeman, R. R. Ruf, and R. J. Gambino. "Picosecond Pulsed Magnetic Fields for Studies of Ultrafast Magnetic Phenomena". In: *IEEE Transactions on Magnetics* 27.6 (1991), pp. 4840–4842. ISSN: 19410069. DOI: `10.1109/20.278964`.

[124] C. Vicario et al. "Off-resonant magnetization dynamics phase-locked to an intense phase-stable terahertz transient". In: *Nature Photonics* 7.9 (2013), pp. 1–4. DOI: `10.1038/nphoton.2013.209`.

[125] M. Basler et al. *Physik: für Wissenschaftler und Ingenieure*. Springer Berlin Heidelberg, 2014. ISBN: 9783642541667.

[126] C. Gerthsen and D. Meschede. *Gerthsen Physik*. Springer-Lehrbuch. Springer, 2003. ISBN: 9783540026228.

[127] Z. Q. Qiu and S. D. Bader. "Surface magneto-optic Kerr effect". In: *Review of Scientific Instruments* 71.3 (2000), p. 1243. ISSN: 00346748. DOI: `10.1063/1.1150496`.

[128] Z. Q. Qiu and S. D. Bader. "Surface magneto-optic Kerr effect (SMOKE)". In: *Journal of Magnetism and Magnetic Materials* 200 (1999), pp. 664–678. URL: `https://doi.org/10.1016/S0304-8853(99)00311-X`.

[129] Y. Ino et al. "Terahertz time domain magneto-optical ellipsometry in reflection geometry". In: *Physical Review B - Condensed Matter and Materials Physics* 70.15 (2004), pp. 1–9. ISSN: 01631829. DOI: `10.1103/PhysRevB.70.155101`.

[130] E. Oblak et al. "Ultrasensitive transverse magneto-optical Kerr effect measurements by means of effective polarization change detection". In: *Journal of Physics D: Applied Physics* 50.23 (2017), 23LT01. ISSN: 13616463. DOI: `10.1088/1361-6463/aa6df2`. URL: `http://stacks.iop.org/0022-3727/50/i=23/a=23LT01?key=crossref.a78fbb14aae9f462090b0fe91eeb92fc`.

[131] T. J. Huisman et al. "Simultaneous measurements of terahertz emission and magneto-optical Kerr effect for resolving ultrafast laser-induced demagnetization dynamics". In: *Physical Review B - Condensed Matter and Materials Physics* 92.10 (2015), pp. 1–8. ISSN: 1550235X. DOI: `10.1103/PhysRevB.92.104419`.

[132] Jan Wallauer et al. "Near-field signature of electromagnetic coupling in metamaterial arrays: a terahertz microscopy study". In: *Optics Express* 19.18 (2011), p. 17283. ISSN: 1094-4087. DOI: `10.1364/OE.19.017283`. URL: `https://www.osapublishing.org/abstract.cfm?URI=oe-19-18-17283`.

[133] Nishant Kumar et al. "THz near-field Faraday imaging in hybrid metamaterials". In: *Optics Express* 20.10 (2012), pp. 11277–11287. ISSN: 1094-4087. DOI: `10.1364/OE.20.011277`. URL: `https://www.osapublishing.org/oe/abstract.cfm?uri=oe-20-10-11277`.

[134] R. A. Shelby, D. R. Smith, and S. Schultz. "Experimental verification of a negative index of refraction". In: *Science* 292.5514 (2001), pp. 77–79. ISSN: 00368075. DOI: `10.1126/science.1058847`. URL: `http://www.ncbi.nlm.nih.gov/pubmed/11292865`.

[135] J. Pendry. "Negative refraction makes a perfect lens". In: *Physical review letters* 85.18 (2000), pp. 3966–3969. ISSN: 1079-7114. URL: `http://www.ncbi.nlm.nih.gov/pubmed/11041972`.

[136] Andreas Bitzer et al. "Terahertz near-field microscopy of complementary planar metamaterials: Babinet's principle". In: *Optics Express* 19.3 (2011), pp. 2537–2545. ISSN: 1094-4087. DOI: `10.1364/OE.19.002537`. URL: `https://www.osapublishing.org/oe/abstract.cfm?uri=oe-19-3-2537`.

[137] W. Hiebert, A. Stankiewicz, and M. Freeman. "Direct Observation of Magnetic Relaxation in a Small Permalloy Disk by Time-Resolved Scanning Kerr Microscopy". In: *Physical Review Letters* 79.6 (1997), pp. 1134–1137. ISSN: 0031-9007. DOI: `10.1103/PhysRevLett.79.1134`.

[138] P. Jelen and S. T. Coulter. "Effects of Supersaturation and temperature on the growth of lactose crystals". In: *Journal of food science* 38 (1973), pp. 1182–1185.